SPATIAL GEOSTATISTICS, LATERAL VARIABILITY, AND SCALE INVARIANCE OF VARIOGRAM PROPERTIES WITHIN DOLOMITES

By

Robert M. Jaecks

B.S., Colorado State University, 2009

A thesis submitted to the
Faculty of the Graduate School of the
University of Colorado in partial fulfillment
of the requirement for the degree of
Master of Science
Department of Geological Sciences
2012

This thesis entitled:

Spatial Geostatistics, Lateral Variability, and Scale Invariance

of Variogram Properties Within Dolomites

written by Robert M. Jaecks

Has been approved for the Department of Geological Sciences

____

David A. Budd

____

Matthew J. Pranter

____

James W. Jennings

Date____________________

The final copy of this thesis has been examined by the signatories, and we find that both the content and the form meet acceptable presentation standards of scholarly work in the above mentioned discipline.

Jaecks, Robert M. (M.S., Geological Sciences)
SPATIAL GEOSTATISTICS, LATERAL VARIABILITY AND SCALE INVARIANCE OF VARIOGRAM PROPERTIES WITHIN DOLOMITIES
Thesis directed by Professor David A. Budd

ABSTRACT

Previous research into the lateral variability of dolostones' attributes at outcrop and subsurface interwell scale suggest that variogram properties such as the correlation range and hole-effect wavelength may follow a power-law function with respect to the scale at which sampling is conducted. The research question posed in this thesis is, does a power-law relationship exist between variogram attributes (i.e., correlation range and hole-effect wavelength) and sampling scale across greater magnitudes of scale (i.e. from thin-section to interwell scale). This question was addressed by analyzing the spatial variability of various properties of dolomites at sub-meter sampling scales (thin-section, outcrop slab, and outcrop photomosaics). Porosity and permeability were analyzed on five outcrop slabs and were shown to have either long-range trends or apparent correlation ranges of 4-20 cm and hole-effects with wavelengths of 20-30 cm. Thin-sections were collected from each of these slabs and analyzed for porosity. These sample were shown to have either long-range trends or apparent correlation ranges of 0.2-0.5 cm and hole-effect wavelengths of 2.8-4.6 cm. Outcrop photomosaics were shown to have either long-range trends or apparent correlation ranges of 5-230 cm and hole effects with wavelengths of 70-560 cm.

The data collected herein and previously collected literature data do define a power-law relationship for both correlation range and hole-effect wavelength over several magnitudes of sampling scale. Three possible hypotheses were considered as explanations of this relationship.

(1) Variogram attributes are related to the sample spacing. (2) Variogram attributes are related to the volume of investigation of each sample. (3) Variogram attributes are illusory because short transect lengths (i.e., slabs and thin-sections) are not long enough to exhibit statistical stationarity. Hypotheses 2 and 3 were shown to be the most likely explanations for the presence of the power-law function. Hypothesis 2 likely accounts for the long correlation ranges seen in subsurface data because each sampling point captures heterogeneity at a much larger scale than sampling for outcrop studies. Hypothesis 3 is valid because short transects (slabs and thin-sections) do not exhibit stationarity relative to the longer outcrop studies. Therefore the variograms based on slab and thin-section data have characteristics that should not be interpreted as ranges and hole-effects. While it is possible that a power-law relationship could exist for correlation ranges and hole-effect wavelengths from micro to megascales, the data collected herein does not demonstrate its existence.

DEDICATION

I would like to dedicate this thesis to everyone who has shared in my struggles and achievements for the last two years. To my mom, dad, and sister who are an ever-present source of love and support. To my friends and colleagues at CU, with whom I've shared priceless conversations over many lunch beers. And most of all to Lauren, who endured every positive and negative moment along the way, all while inspiring me in her own quiet way to do the best I could.

ACKNOWLEDGEMENTS

First and foremost, I would like to thank my advisor, Dr. David Budd, who provided just the right amount of insight and guidance while allowing me to explore. I feel confident in saying that his direction has made this thesis much better as well as helping me to become a better scientist. I would also like to thank my committee members Dr. Matthew Pranter and Dr. Jim Jennings for their past and continued guidance. Their collective wisdom has added a great deal to the content of this thesis.

Funding for this project came from the Analysis of Variability in Dolomites (AVID) Consortium and general funding came from the Department of Geological Sciences through a Teaching Assistantship. I would like to thank all of those that contributed financially for making my research possible.

Many thanks to Paul Boni for the numerous days he let me use his lab and equipment. Thank you to Kevin Mahan for the use of his microscope and camera. Thank you to my undergraduate assistants (Morgan, Alex, and Hannah) who all spent many hours helping with data collection.

TABLE OF CONTENTS

LIST OF TABLES

Table

LIST OF FIGURES

FIGURE

CHAPTER 1: INTRODUCTION AND BACKGROUND

Carbonate rocks play an important role in the production of hydrocarbon reservoirs around the world. The petrophysical properties which govern successful recovery of hydrocarbon reserves are the porosity and permeability of the reservoir rock. Quantifying the porosity and permeability of carbonate rocks is especially troublesome because they are highly prone to post depositional diagenetic processes that alter the petrophysical properties (Moore, 1989). One such process is dolomitization, which can occur in a variety of settings and under numerous conditions within each of those settings (Moore, 1989). Geostatistical analyses are useful tools for quantifying the spatial characteristics of dolomitic rocks and they are used quite extensively within industry to better model dolostone reservoirs. Outcrop analogs also are used in order to build a geostatistical database that can then be used for reservoir modeling purposes. Dolomite outcrops have been quite extensively studied to this end (Kittridge, 1990; Senger, 1993; Eisenberg et al., 1994; Grant et al., 1994; Kerans et al., 1994; Wang et al., 1998; Jennings, 2000; Pranter et al., 2005, 2006; Budd et al., 2006; Bribiesca, 2010; Mathias, 2011).

Perhaps the most commonly used tool for geospatial analysis is the variogram because of its utility within modeling algorithms (Gringarten et al., 2001). The experimental semi-variogram is a measure of the variance in sample sets with increasing separation (lag). Thus, values composing the variogram will increase as samples become more dissimilar and decrease as samples become more similar (Gringarten et al., 2001). A typical variogram (Figure 1) is composed of three important parts: the nugget, range, and sill. The nugget is considered to be random variability at a hypothetical lag of zero. As lag increases away from the nugget, variance will generally also increase because increasingly distant points are less likely to be correlated to one another. The range is the point at which samples are far enough apart that there is no correlation between them and the variance reaches its maximum value. At still greater separation distances, the variance neither increases or decreases and the variogram is at the sill. There are also two other structures that some variograms may exhibit: a hole effect and a trend. A hole effect is a decrease in variance at a lag beyond the range and often represents some form of cyclicity (Gringarten et al., 2001). A trend is a steady increase in variance at larger lag distances, which is a common result of geologic phenomena such as coarsening upward sediment packages (Gringarten et al., 2001). Figure 1 shows all of these variogram characteristics. The nugget accounts for 25% of total variance, the range accounts for 55% of total variance and the long range trend accounts for 20% of variance. There is also a hole effect with a wavelength of 0.2.

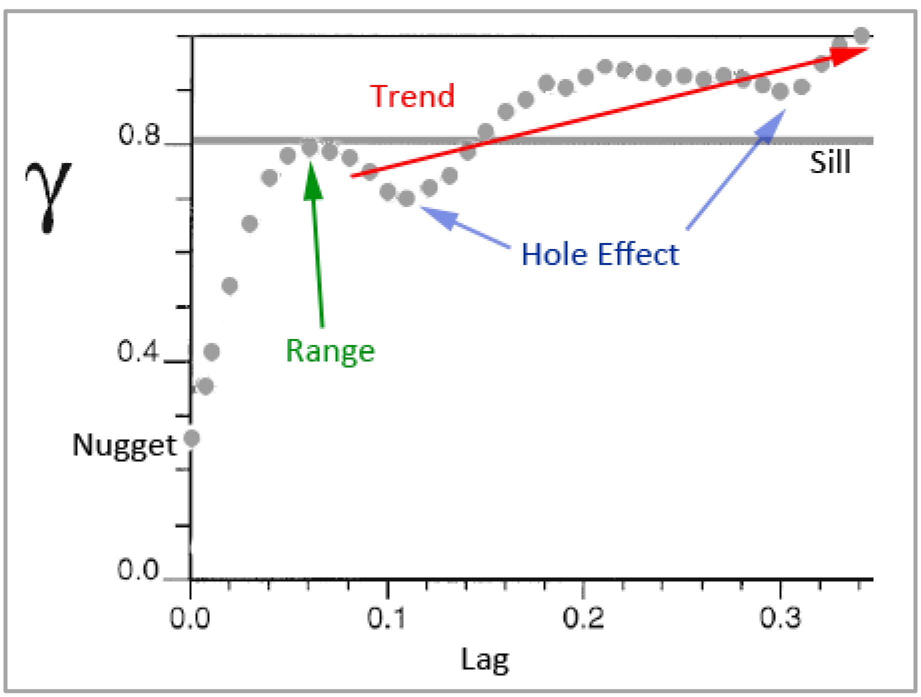

Figure 1.
A typical variogram (adopted from Gringarten and Deutsch 2001). Four scales of variance are shown: the hypothetical nugget, the correlation range, a trend and hole effects. The hole effects do not add to overall variance and occur within the trend in this example. Most variograms may show only a nugget and a range. Hole effects and trends indicate long range patterns in the variance.

Much of the geostatistical work on dolomite outcrops has been done in Permian dolograinstones of the San Andres Formation in southern New Mexico (Kittridge, 1990; Senger, 1993; Eisenberg et al., 1994; Grant et al., 1994; Kerans et al., 1994; Wang et al., 1998; Jennings, 2000). Eisenberg et al. (1994) collected permeability from three horizontal transects of 28 to 36 meters (two 30-cm sample spacing and one 15-cm sampling spacing) in the San Andres Formation along the Algerita Escarpment. The results, as related to this study are presented in Figure 2. A spherical model was used to fit the experimental semivariograms and these models yielded nuggets of 0.25, 0.26 and 0.63 and short-range correlations of 2.4, 3.6, and 7 meters for the HOT1, HOT2 and HOT3 transects, respectively. Although Eisenberg et al. (1994) did not discuss the presence of long-range hole effects, it is possible to observe declines in semivariance that could be intrepreted as hole effects, as shown by the blue arrows in Figure 2. These hole effects may even exhibit cyclicity with wavelengths of 2-5 meters.

Grant et al. (1994) performed a similar study along the Algerita Escarpment collecting lateral permeability data at 15-cm intervals over a 90 meter transect. Figure 3 shows the experimental semivariogram created using these data. Grant et al. (1994) found a nugget of 0.2 and a short-range correlation of 3.6 meters. Grant et al. (1994) surmised that this shorter than expected correlation range was likely due to heterogenity in dolomite texture (sucrosic versus tightly-cemented dolomite). Hole effects were not discussed by Grant et al. (1994), but a hole effect with wavelength of about 8 meters appears to be present (blue arrows in Figure 3).

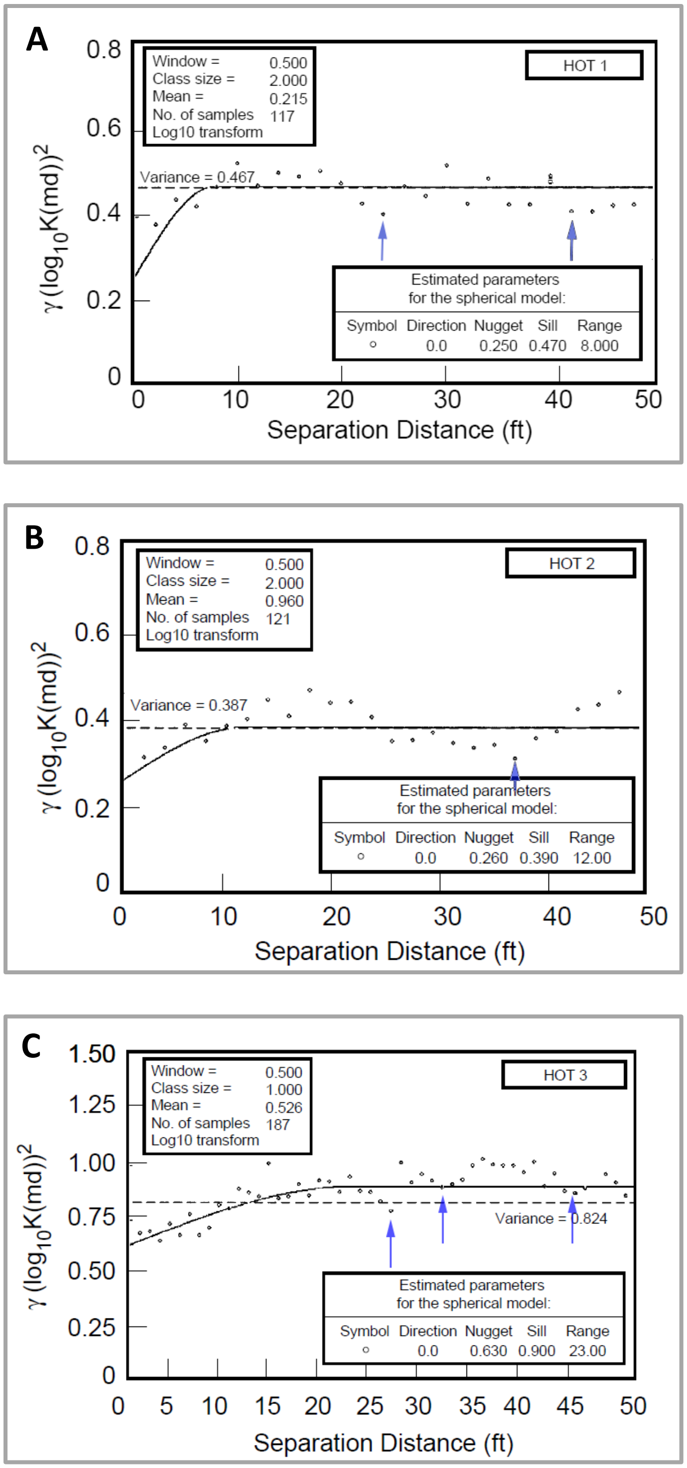

Figure 2. Semivariograms of Log_{10} permeability from three lateral transects (A-HOT1, B-HOT2, C-HOT3) in the Permian San Andres Formation. Hole effects are marked by blue arrows. (From Eisenberg et al., 1994)

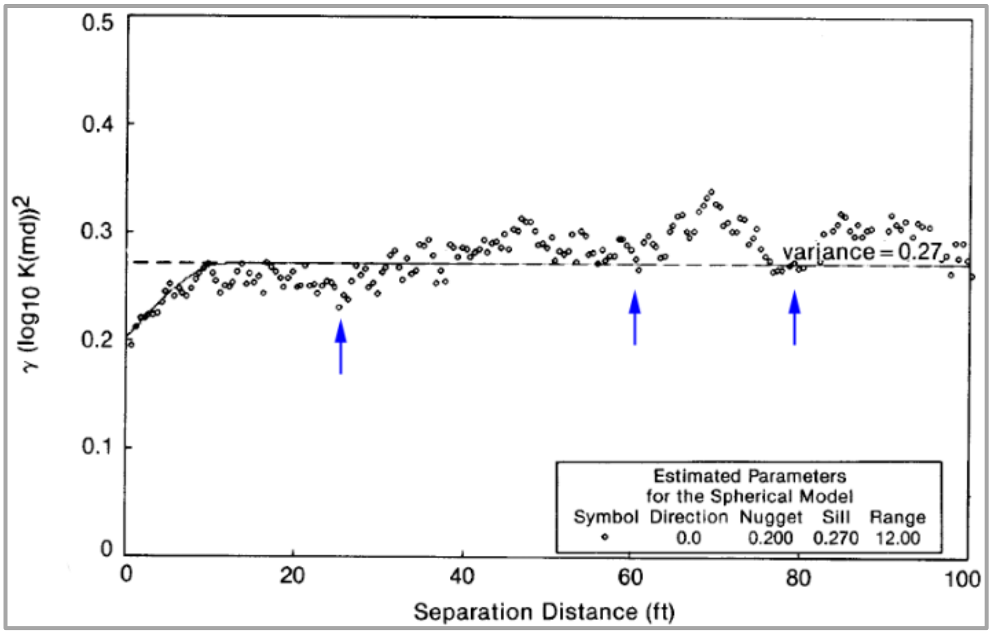

Figure 3. Semivariogram of Log_{10} permeability from a 90-m lateral transect with 15-cm sample spacing, obtained from the Permian San Andres Formation. Here, the nugget is 0.2, range is 3.6 meters and there are hole effects with a wavelength of 6-10 meters as shown by blue arrows. (From Grant et al., 1994)

Jennings et al. (2000) summarized interesting results on two long lateral transects: one 314 meters with a 30 cm sample spacing and a 835 meter transect with 150 cm sample spacing. These transects were collected in the San Andres and Victorio Peak Formations at Lawyer Canyon and Apache Canyon. Figure 4 shows the variograms for these respective transects. The short range correlations were 6 and 30 meters respectively. Both transects show strong evidence for hole effects with wavelengths on the order of 42-54 meters (Jennings et al., 2000). The Apache Canyon variogram in particular shows 5-6 regularly spaced hole effects.

The Missippian-age Madison Formation has also been extensively studied in regard to the spatial variability of dolomite (Pranter et al., 2005, 2006; Budd et al., 2006). Pranter et al. (2005) and Pranter et al. (2006) discussed the effect of dolomite variability on fluid flow, an important consideration for optimizing production from carbonate reservoirs. Pranter et al. (2006) found that sweep efficiency and large-scale fingering were optimized where correlation

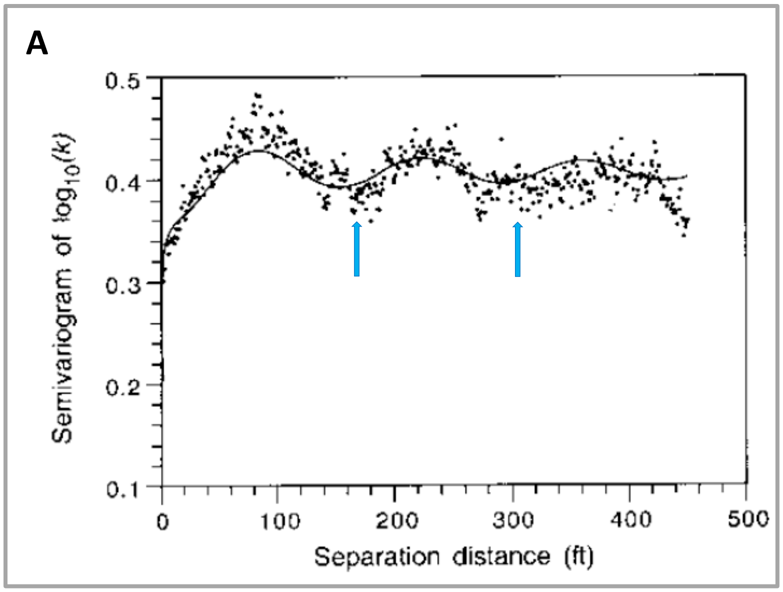

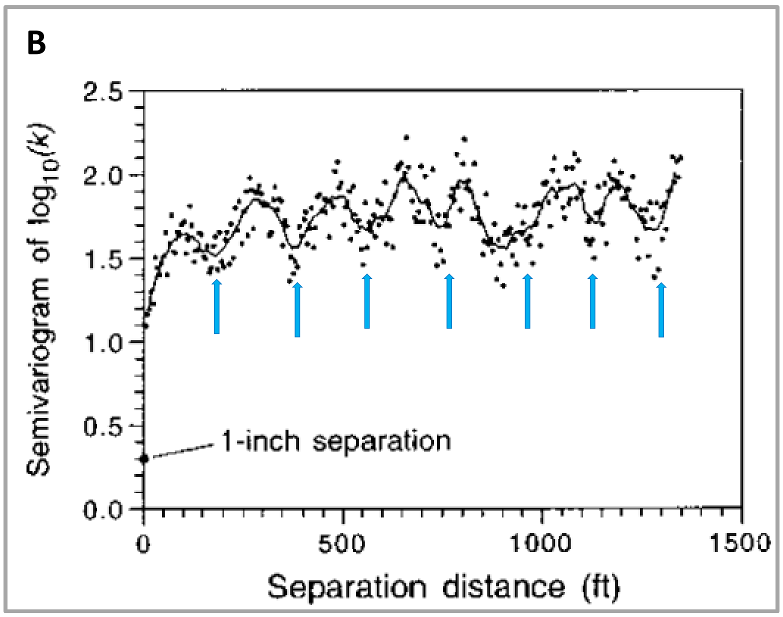

Figure 4. Semivariograms of Log_{10} permeability in the Permian San Andres Formation and based on lateral transects of (A) 314 m with a 30 cm sample spacing and (B) 835 m with a 150 cm sample spacing. Reported ranges are 6 m and 30 m and hole effect wavelengths vary from 42-54 meters. (From Jennings et al., 2000)

ranges were longer. Dolograinstones from Lysite Mountain contain 55% of their total variance at a lag of 30 cm, while short-range correlation is 4.5 meters (both porosity and permeability) and multiple scales of longer range periodicities exist with wavelengths from 4.5-36.9 meters (Pranter et al., 2006). Dolowackestones from Sheep Canyon show similar results with a nugget effect of 58-65%, short range correlations of 4 and 6.7 meters for permeability and porosity respectively, and multiple scales of long range periodicity with wavelengths from 4.6-45.7 meters (Pranter et al., 2005, 2006).

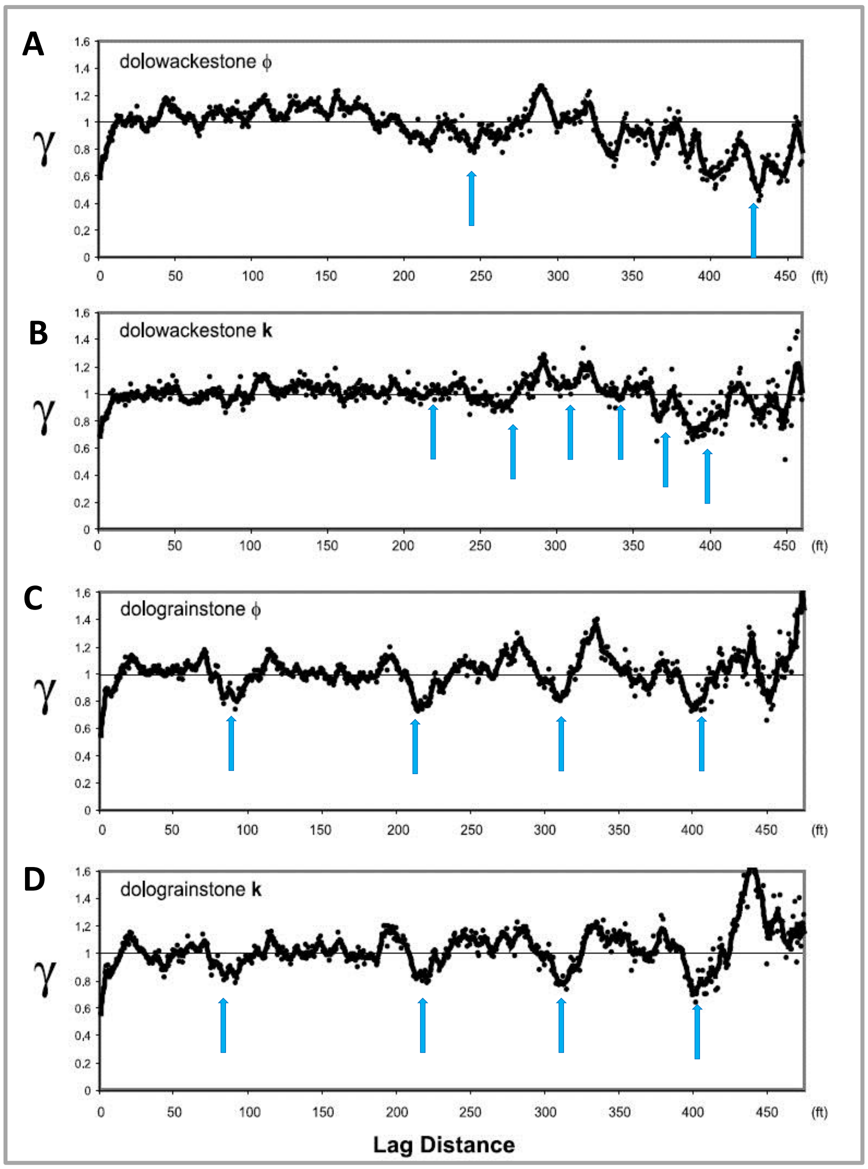

Figure 5. Semivariograms of porosity (A and C) and permeability (B and D) from a dolowackestone and a dolograinstone in the Mississippian Madison Formation. Results show correlation ranges of 4-6.7 meters and hole effects (blue arrows) with wavelength from 4.6 to 45.7 meters. Black line represents a 5-point moving average. (From Pranter et al., 2006)

Budd et al., (2006) also investigated petrophysical variability and trace-element concentration variability using the same Sheep Canyon transect as Pranter et al., (2006). All of the variables measured (Figure 6) showed three scales of variability: a near random component at minimum lag accounting for over 50% of variance, a short-range correlation from 2.4-7.6 meters and long-range oscillatory patterns with wavelengths ranging from 1.2 up to 24.2 meters (Budd et al., 2006). In response to similarities between variograms in San Andres and Madison dolomites, Budd et al. (2006) concluded that long-range oscillatory patterns could be a universal property of dolomite. Budd et al. (2006) provide three possible explanations for the origin of these observed patterns: (1) inherited pattern from limestone precursor, (2) a result of overprinting by later diagenetic events and (3) chemical and petrophysical self-organization during dolomitization. Budd et al. (2006) argued that the presence of oscillatory patterns in the

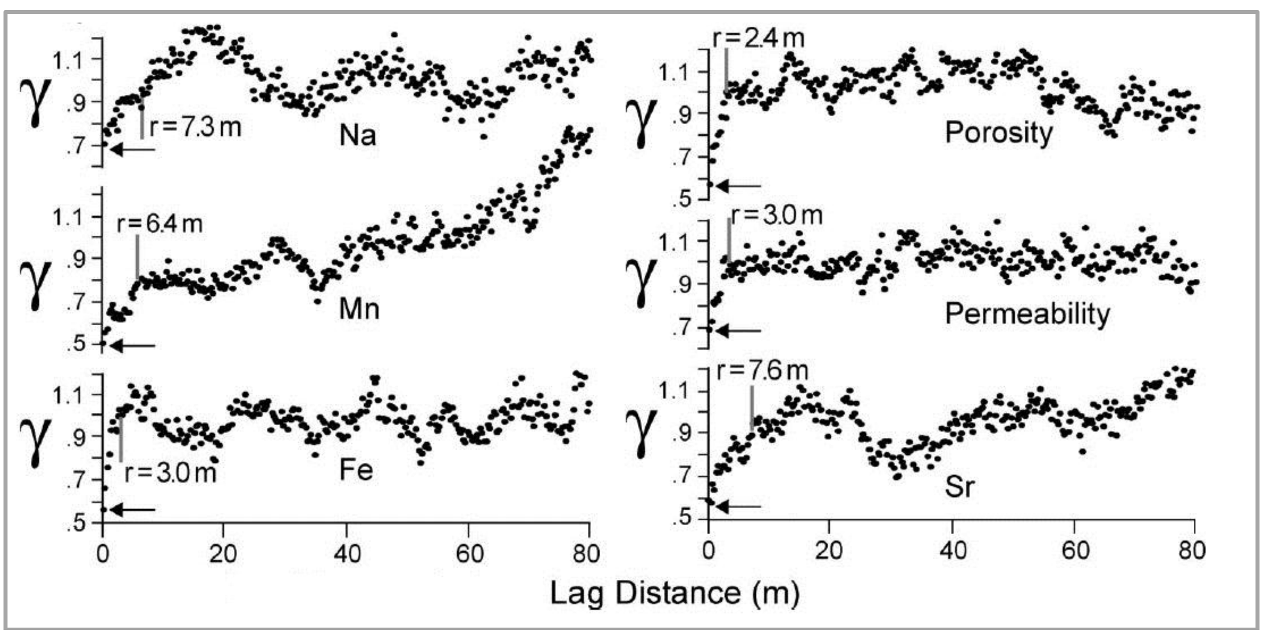

Figure 6. Semivariograms showing commonality between correlation range and hole effects for different variables including trace elements, porosity and permeability. All semivariograms are derived from analysis of dolowackestone from Sheep Canyon, WY. Correlation ranges (r) are shown for each semivariogram. (From Budd et al., 2006)

trace-element chemistry and slightly different patterning between porosity and permeability is most likely an indication of self-organization during dolomitization due to feedbacks between overdolomitized and underdolomitized areas.

This conclusion was investigated by two theses, Bribiesca (2010) and Mathias (2011), both on outcrops with 30 cm sample spacings. Bribiesca (2010) concluded that all observed hole effects in dolomite of the Eocene Avon Park Formation were caused by a diagenetic overprint due to surface weathering. In contrast, Mathias (2011) sampled the Miocene Seroe Domi Formation from limestone through a reaction front into dolomite and found long-range spatial patterns in dolomite that were not present in the limestone. Mathias (2011) concluded that those results were best explained by self-organizing processes during dolomitization.

Published studies of petrophysical variability of subsurface dolomites that include variogram data are uncommon. While many studies include reservoir models that have been built using variography, the actual variogram attributes (range, wavelength of hole effects, sample separation distances) are difficult to find or just not reported because variography was not the focus of the study. The small number of published subsurface studies that do provide variogram attributes for dolomite reservoirs indicate that variograms based on well data tend to have long correlation ranges. Rossini et al. (1994) used well spacings of about 280 m and found correlation ranges of 600-650 meters. Meddaugh et al. (2009) also analyzed porosity using borehole geophysical log and found that 75 m-spaced wells gave a correlation range of ~300 m and 500 m-spaced wells gave a correlation range of ~1500 m. Dull (2004) used log-to-core correlation to build a log-based lithologic indicator, called PFACIES, and then created semivariograms based on PFACIES calculations for two depositional cycles within the reservoir

(Figure 7). With well spacings of approximately 400 m, correlation ranges were 1523 and 2233 meters respectively for different facies (Dull, 2004). None of these three subsurface studies report any hole effects.

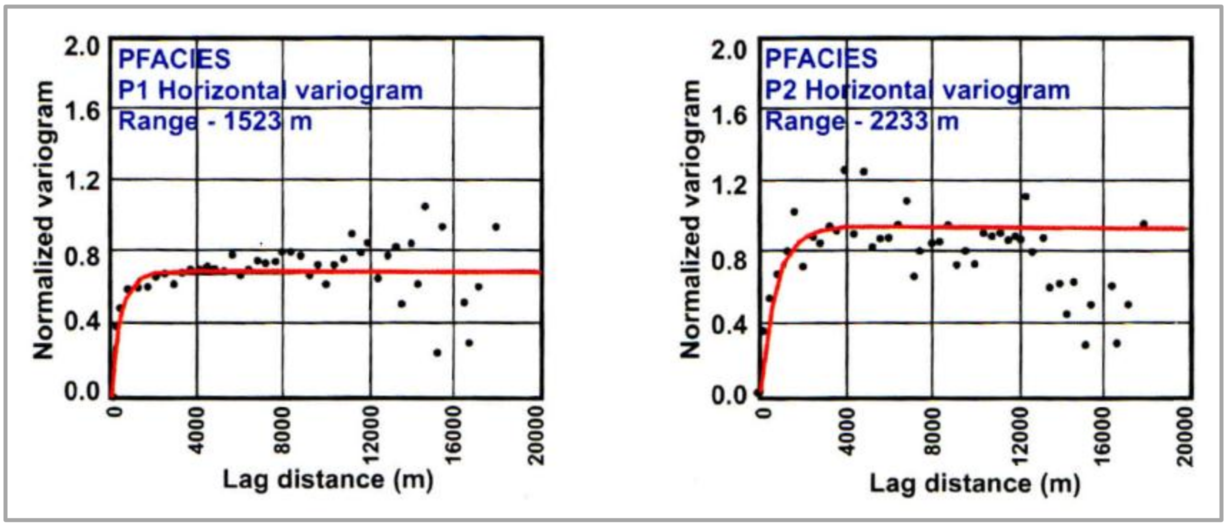

Figure 7. Semivariogram of PFACIES in two cycles (P1 and P2) of the Second Eocence reservoir of Wafra Field. Correlation ranges are 1523m and 2233m respectively. (From Dull, 2004)

Collectively, the many outcrop studies of lateral variability in the petrophysical properties of dolomite suggest correlation ranges on the order of 2.4 to 30.5 meters and hole effects at wavelengths of 1.2 to 55 meters (Table 1). However, subsurface data collected at interwell spacings of 75 to 500 meters reveal longer correlation ranges of 300 to 2230 meters and no hole effects (Table 1). When outcrop and subsurface datasets are considered together (Figure 8), it appears that short-range correlation follow a power-law, such that range is related to sample spacing. What sample spacing represents is a topic that will be explored in the discussion.

On Figure 8, it is unclear if long-range oscillatory patterns (hole effects) follow the same power-law as correlation range because the studies at interwell spacings did not record any hole effects. This could be due to an actual lack of long range pattern at that scale. However, it is also possible that long-range structures are present at interwell spacings, but they are not being captured due to a paucity of data (i.e., transect lengths across oil fields are not long enough to resolve hole effects).

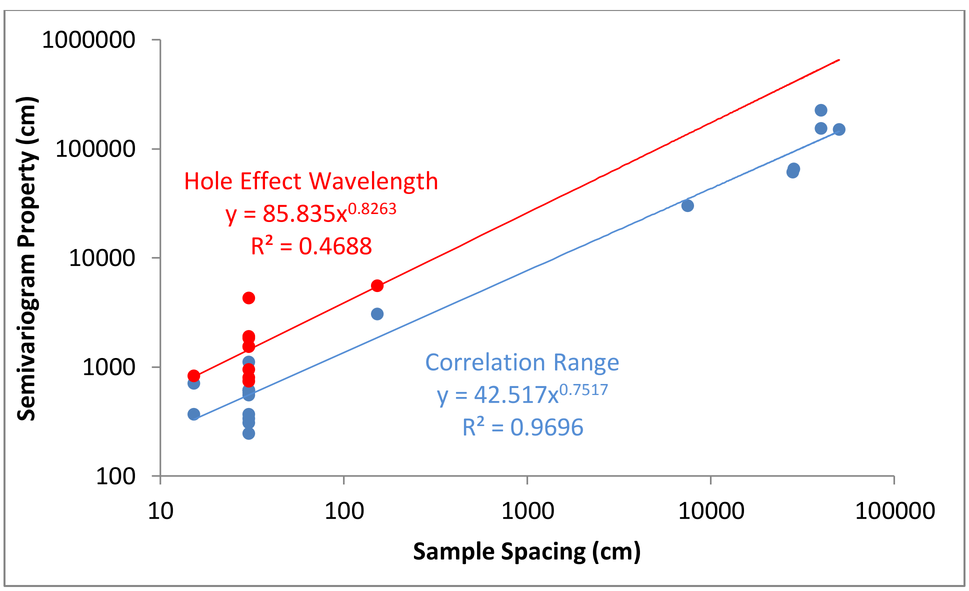

Figure 8. Correlation ranges (blue) and hole effect wavelength (red) in the attributes of dolomites as a function of sample spacing. There is an apparent power-law relationship between correlation range and sample spacing. The data are unclear as to whether a similar power-law exists between hole effect and sample spacing. Data from Table 1.

Source	Variable	Formation - Age	Sample Interval (m)	Correlation Range (m)	Hole Effect (m)
Eisenberg et al., 1994	Permeability	San Andres - Permian	0.15	7.0	8.2
Grant et al., 1994	Permeability	San Andres - Permian	0.15	3.7	
Bribiesca 2010	Plug porosity	Avon Park - Eocene	0.30	6.1	
Bribiesca 2010	Plug Permeability	Avon Park - Eocene	0.30	5.8	
Mathias 2011	Plug Porosity	Seroe Domi - Miocene	0.30	5.5	18.9
Mathias 2011	Plug Permeability	Seroe Domi - Miocene	0.30	11.0	
AVID - Lysite	Porosity	Madison - Mississippian	0.30	6.1	15.2
AVID - Sheep	Porosity	Madison - Mississippian	0.30	3.4	9.5
AVID - Lysite	Permeability	Madison - Mississippian	0.30	6.1	15.2
AVID - Sheep	Permeability	Madison - Mississippian	0.30	3.0	18.3
Eisenberg et al., 1994	Permeability	San Andres - Permian	0.30	2.4	7.3
Eisenberg et al., 1994	Permeability	San Andres - Permian	0.30	3.7	7.9
Jennings, 2000	Permeability	San Andres - Permian	0.30	6.1	42.7
Jennings, 2000	Permeability	San Andres - Permian	1.52	30.5	54.9
Meddaugh et al., 2009	Porosity	Humma Marrat - Jurassic	75	299	
Meddaugh et al., 2009	Porosity	Humma Marrat - Jurassic	500	1494	
Rossini 1994	Facies Indicator	Unspecified	280	610	
Rossini 1994	Porosity	Unspecified	284	650	
Dull 2004	PFacies	Wafra Field - Eocene	400	1524	
Dull 2004	PFacies	Wafra Field - Eocene	400	2232	

Table 1 – Semivariogram attributes from studies of lateral petrophysical variability in dolomites collected from literature and previous studies. Ranges and hole effect wavelength were collected from sources' experimental semivariogram, although raw data were available in a few cases.

In light of the data shown in Figure 8 and Table 1, the research question posed in this thesis is, does a power-law relationship exist between correlation range and sample spacing and between hole effect wavelength and sample spacing. Because it is not feasible to collect data at large spacings (e.g., tens to hundreds of meters) over many kilometers, the analytical strategy herein is to sample at scales below common outcrop sample spacings (30 cm) and then extrapolate to large, interwell scales. Meter and less scales will be assessed using large outcrop slabs, thin sections, and outcrop photographs. Ranges and hole effect wavelengths derived from those data sets will test the research question when added to Figure 8.

CHAPTER 2: METHODS

Sampling

Five outcrop slabs were collected at three separate locations, with slab lengths ranging from 32 to 110 cm and heights ranging from 8 to 42 cm. Three of these slabs are dolograinstones of the Mississippian Madison Formation at Lysite Mountain, Wyoming. Another Madison slab was collected from a dolowackestone at Sheep Canyon, Wyoming. The fifth outcrop slab was collected from the Devonian Cairn Formation, which outcrops west of Canmore, Alberta near Grassi Lakes.

Slabs were cut off the outcrop using a concrete cut-off saw. In order to recover as much sample as possible, slabs were cut into blocks on the outcrop face and then quarried off the outcrop using hammer and chisel (Figure 9). Sample extraction was much easier in the Madison dolomites where higher porosities and less brittle fracturing allowed easier removal of blocks. The lateral dimensions for the BCDE, KL, WXYZ (Madison dolograinstones) and Sheep (Madison dolowackestone) slabs where 47 cm, 32 cm, 54 cm, and 76 cm respectively. Initial analyses on the Madison slabs indicated that the Cairn slab needed to be longer in order to capture any possible spatial patterns. Therefore, the Cairn slab was cut to a length of 110 centimeters.

Outcrop photomosaics were also taken of the Cairn Formation at the Grassi Lakes location, the Tansill Formation in Dark Canyon, New Mexico, and the San Andres Formation at Pot Hole Tank, New Mexico. The Grassi Lakes location is completely dolomitized and the outcrop photomosaics were taken with the intention of analyzing the spatial patterning of macroscale vuggy porosity in the dolomite (Figure 10). Photos were taken on the opposite side of the ravine from outcropping rocks. The Dark Canyon and Pot Hole tank locations expose dolomitization fronts (Frost et al., in press; Garcia-Fresca, 2009) between limestone and

Figure 9. Example of method for removing slab from outcrop face. Blocks were cut using a gas cut-off saw and then chiseled out. Example is from Cairn Formation, Alberta, Canada.

Figure 10. Macroscale vugs in the Cairn Formation, Alberta, Canada.

dolomite and the photos were taken with the intention of analyzing the spatial patterning of the dolomite bodies (Figure 11). Outcrops in Dark Canyon were in a dry creek bed and photographs were taken above the outcrop by standing on a ladder and moving the ladder as needed to create photomosaics. Three separate dolomite reaction fronts were photographed at the Dark Canyon location. At Pot Hole Tank, the dolomitization fronts occur at the base of a steep cliff and photomosaics were taken 3 meters from the cliff face.

Figure 11. Outcrop photograph of a dolomite reaction front where dolostone is lighter colored and limestone is darker colored. Core plug holes are 30 cm apart. Tansill Formation, Dark Canyon, New Mexico.

Slab Preparation and Data Collection

The desired data from the slabs was permeability and porosity on a centimeter by centimeter scale. In order to collect permeability, the face of the slab needed to be smooth so that a minipermeameter probe could form a strong seal with the surface. This was done using a slab saw to trim off the rough outcrop face. An important consideration was to keep the smoothed face from each block even with the adjacent blocks such that a lateral transect across the entire slab stayed in the same plane. Once slabbed, point grids at 1 cm spacings were placed on the rock faces. With the exception of the KL slab, grids were 8 to 12 rows high and extended horizontally across the entire slab. Forty rows were used on the KL slab because it was short (32 cm) in the horizontal direction.

Permeability data were collected twice at each grid point on the slab faces using a TEMCO Mini-Probe Permeameter 410, which injects nitrogen into the sample (Figure 12). Permeability is measured using a constant gas pressure and recording the flow rate into the sample once a steady state has been reached (Hurst, 1995). Permeabilities in the Madison Formation were measured using an injection pressure of 12 ± 0.2 psi greater than atmospheric pressure. Permeabilities in the Cairn Formation where measured using an injection pressure of 24 ± 0.2 psi greater than the atmospheric pressure. This was done because higher injection pressures are required to resolve very low permeabilities. All measurements were made using a probe tip diameter of 1.6 mm.

Once the TEMCO minipermeameter detected that a steady state had been reached with respect to gas pressure, the flow rate was recorded. Gas flow rates were converted to liquid permeability using a set of standard core plugs with known Klinkenberg permeabilities (Budd et al., 2001). Standard data were collected each day before and after slab measurements were obtained. Gas flow rates through the standards were regressed against the logarithm of the known permeabilities to produce a calibration equation between measured flow rates and permeability (Figure 13). This equation was then used to convert flow rates measured on the outcrop slabs to permeability. Further discussion of this process can be found in Budd et al. (2001). Minimum detectable and reproducible flow rates at an injection pressure of 12 psi greater than the ambient was ~8 cc/min, which sets the permeability detection limit at 2 mD for the Lysite and Sheep slabs. Minimum detectable and reproducible flow rates at an injection pressure of 24 psi greater than the ambient was ~2.3 cc/min, which sets the permeability detection limit at 0.1 mD for the Cairn slab.

The smooth-faced slabs were gridded (Figure 14) at a one centimeter scale and gas flow rates were measured twice at each point as an evaluation of reproducibility (Figure 15). The geometric mean of both measurements at a particular grid point is reported herein as the permeability of that point. With respect to the two measurements at each point, the Cairn slab had the most repeatable measurements, followed by the Sheep slab and then by the Lysite slabs (Figure 15). An explanation for this difference could be that the Cairn was sampled at the highest injection pressure (24 psi above atmospheric pressure), which allowed for more precise measurement at lower flow rates. It is also possible that the difference could arise due to measurement biases by different investigators (all three sets of slabs were analyzed by different minipermeameter operators). One further explanation could be rock fabric. When the second measurement was taken, the probe tip does not necessarily cover the exact same area. There may be a discrepancy of some fraction of a millimeter. Thus, the Cairn slab which has small and homogenously distributed pores should yield good reproducibility at each grid point. In contrast, the Lysite slab, which has a heterogeneous pore system that includes moldic pores, should have yielded more varied permeability values even for the same “point”.

Porosity values were collected on roughly 2 cm x 2 cm x 2 cm cubes cut from each slab after permeability values were collected. This means that each porosity cube had four permeability values associated with it, except where cutting required that the cube be only 1 cm in either the X or Y direction (e.g. when cutting the cube along the edge of a block). Porosity cubes were cut from the same face on which permeability values were taken. A trim saw was used to cut the cubes and a lap polisher was used to remove any sharp edges. Porosity values were then measured using a four step process: (1) weigh the cube to determine the volume of dolomite; (2) wrap the cube in Parafilm, weigh the wrapped cube to determine the mass of Parafilm added, and then calculate the volume of Parafilm given its density of 0.767 g/cc; (3) weigh a beaker filled with water; and (4) suspend the wrapped cube in the water and record the new weight of the beaker. The difference in beaker weights is the weight of the displaced water which converts to the volume of the wrapped cube. Subtracting the volume of the

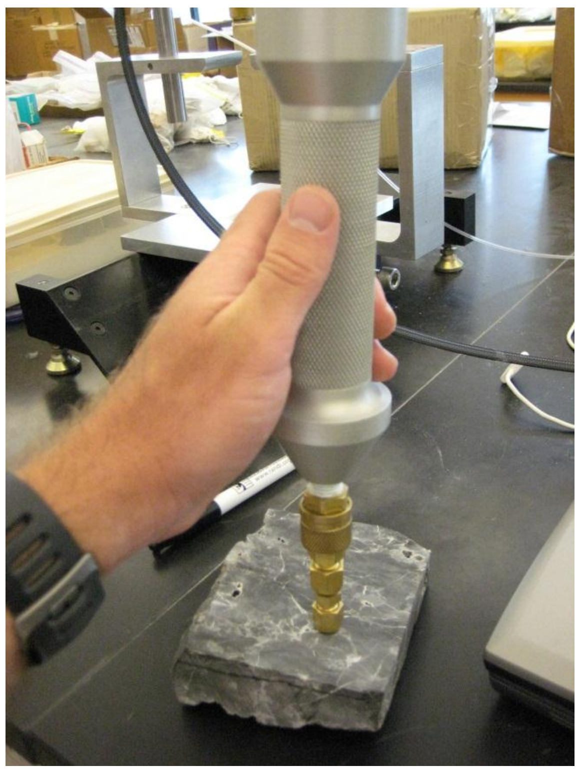

Figure 12. Measurement of gas flow rate at a point on the Cairn Formation slab using the hand-held probe of the Temco minipermeameter.

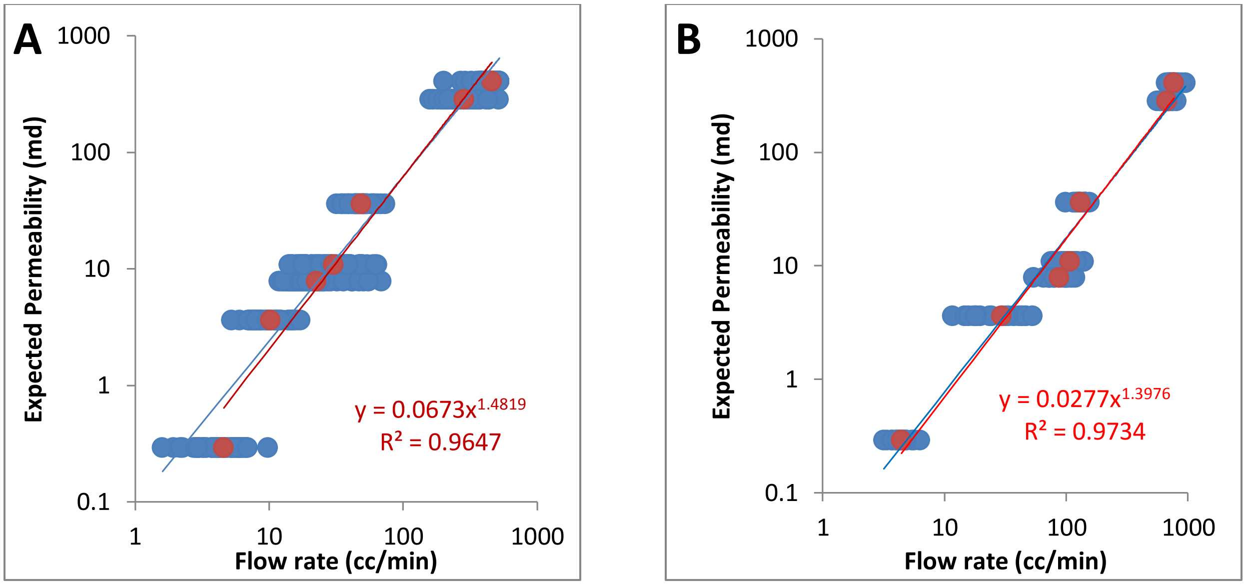

Figure 13. Calibration curves used to convert measured gas flow rates to permeability, taken at both (A) 12psi and (B) 24psi above atmospheric pressure. Blue dots represent all measured points and red dots represent the mean of those points for a specific standard. The linear regression through the average points (red line) was used to convert flow rates to permeability.

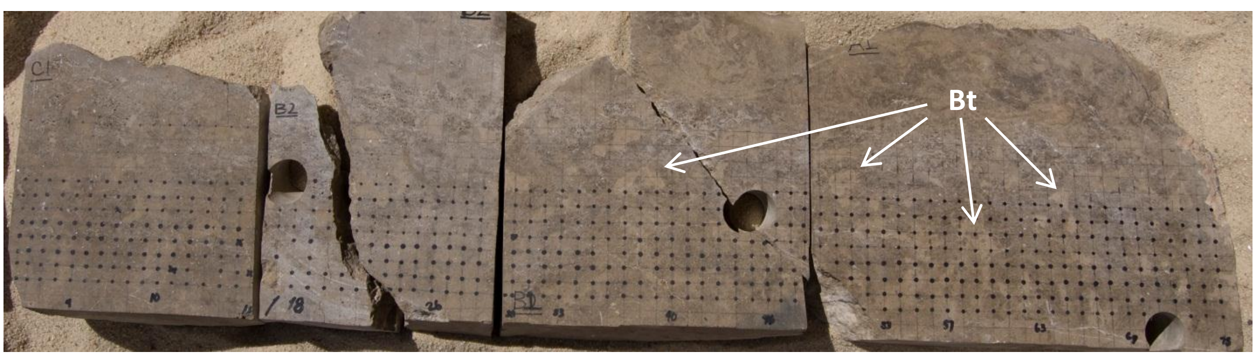

Figure 14. Example of 1 cm-spaced gridded surface of the Sheep slab, which is 8 cm x 76 cm. Bioturbation is notable on this slab as relatively light areas (Bt).

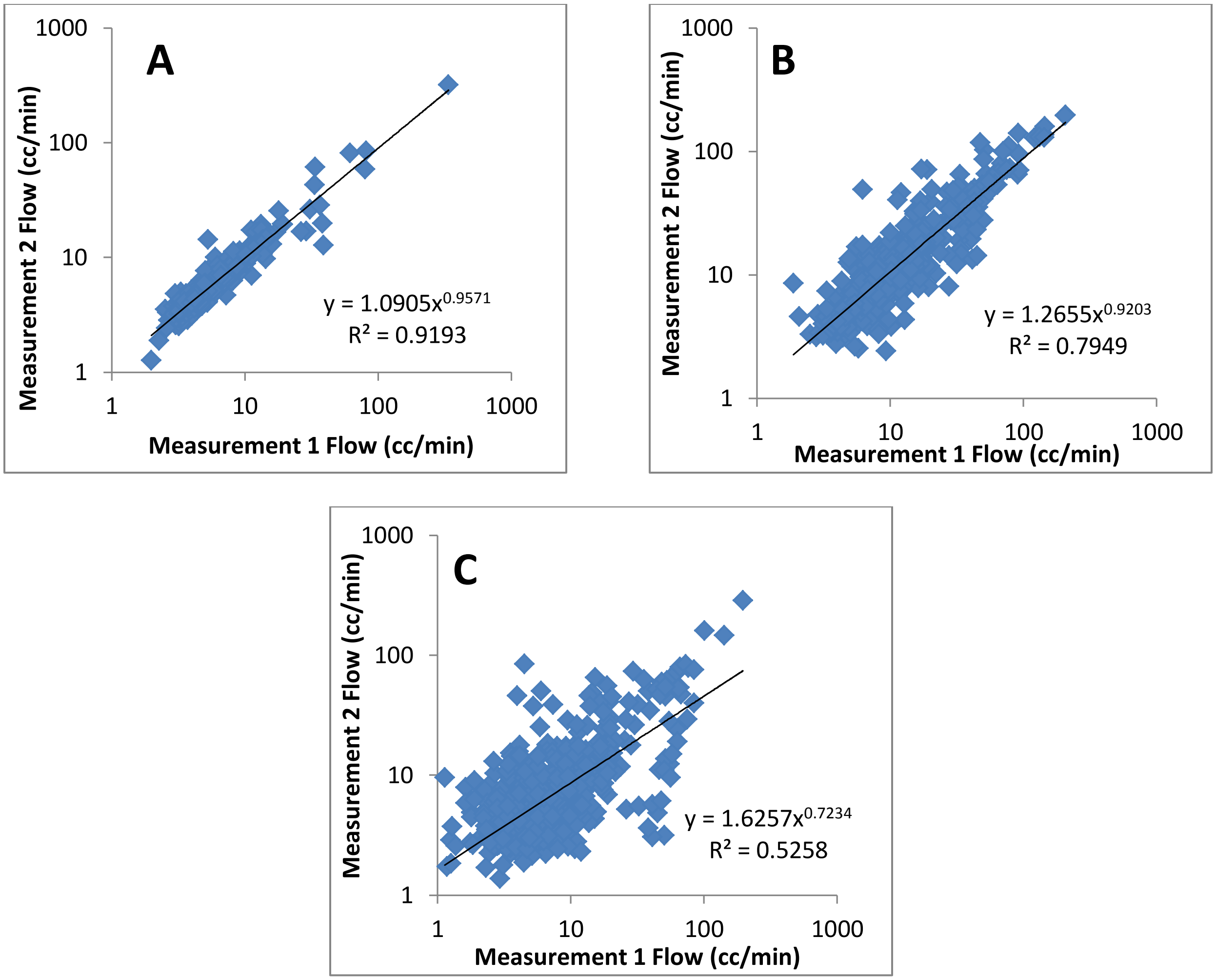

Figure 15. Permeability reproducibility between measurements shown for the (A)Cairn, (B)Sheep and (C) Lysite (BCDE & WXYZ) slabs. The Cairn slab shows the best overall reproducibility in the data, followed by the Sheep and Lysite respectively.

Parafilm (step 2) gives the volume of the cube. Porosity was then determined using the cube volume and the assumption that all cubes were 100% dolomite with a density of 2.85 g/cc. Every tenth cube was measured twice in order to check reproducibility (Figure 16), which was generally good aside from one outlier for the Lysite slabs.

Thin-Section Preparation and Data Collection

Thin-sections were prepared from the opposite faces of the slabs on which permeability and porosity measurements were collected (i.e. the opposite pieces of the slabs when sawed to create smooth surface). Locations for thin-sections (Figure 17) were picked based on observed permeability values, with the objective being to cross heterogeneities while avoiding large vugs or fractures. Three oversized (5 x 7.6 cm) thin-sections were cut from laterally adjacent material on each of the five slabs. Prior to thin-sectioning, each sample was vacuum and pressure impregnated with a blue epoxy to mark porosity.

All thin-sections were photographed using a Leica Z16 APO macroscope mounted with a SPOT Flex 64 megapixel digital camera. The macroscope was used because of difficulties in stitching together thin-section photographs at higher magnification (due to number of photos and the ultimate size of the file). Using the macroscope allowed the thin sections to be completely photographed in no more than 15 pictures of 96 dpi (typical field of view for each photomicrograph was 22 x 22 mm). These pictures where then stitched together using Adobe Photoshop's Automate>Photomerge function. Photoshop was also used for image manipulation since spatial statistics were to be done based on grayscale values. For example, the primary goal was to quantify the spatial distribution of porosity. Thus, all blue pixels (porosity) were selected in Photoshop and turned into a black layer with every other pixel in the image (dolomite) turned into a white background (Figure 18). These grayscale images were then imported into QuantumGIS which enables the conversion of raster images into a table of ASCII grayscale values, thus giving each pixel an x-y coordinate. Variography could then be performed on the grayscale values.

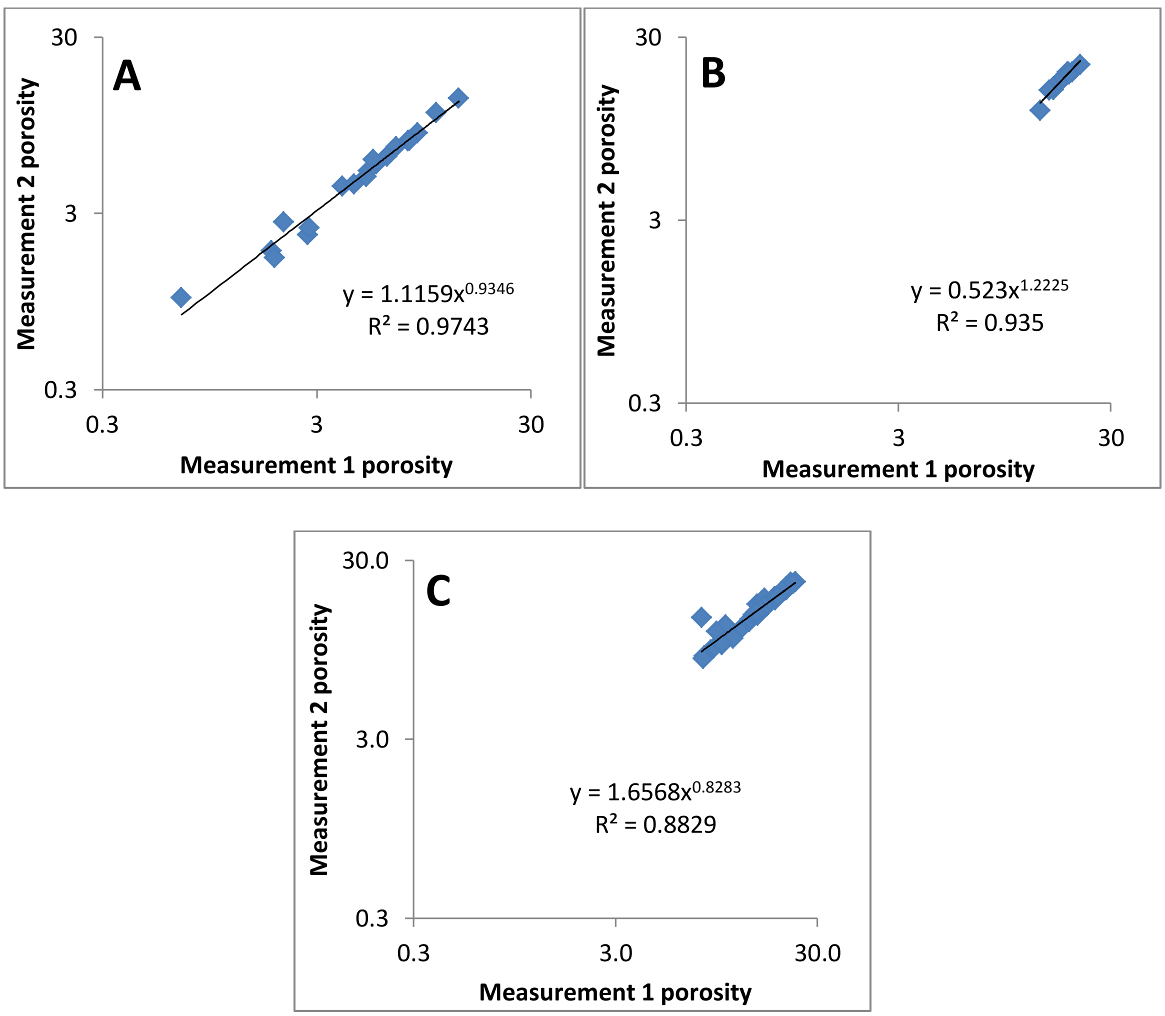

Figure 16. Porosity reproducibility between measurements shown for the (A) Cairn, (B) Sheep, and (C) Lysite (BCDE & WXYZ) slabs. All show good reproducibility, minus several small outliers in the Lysite dataset.

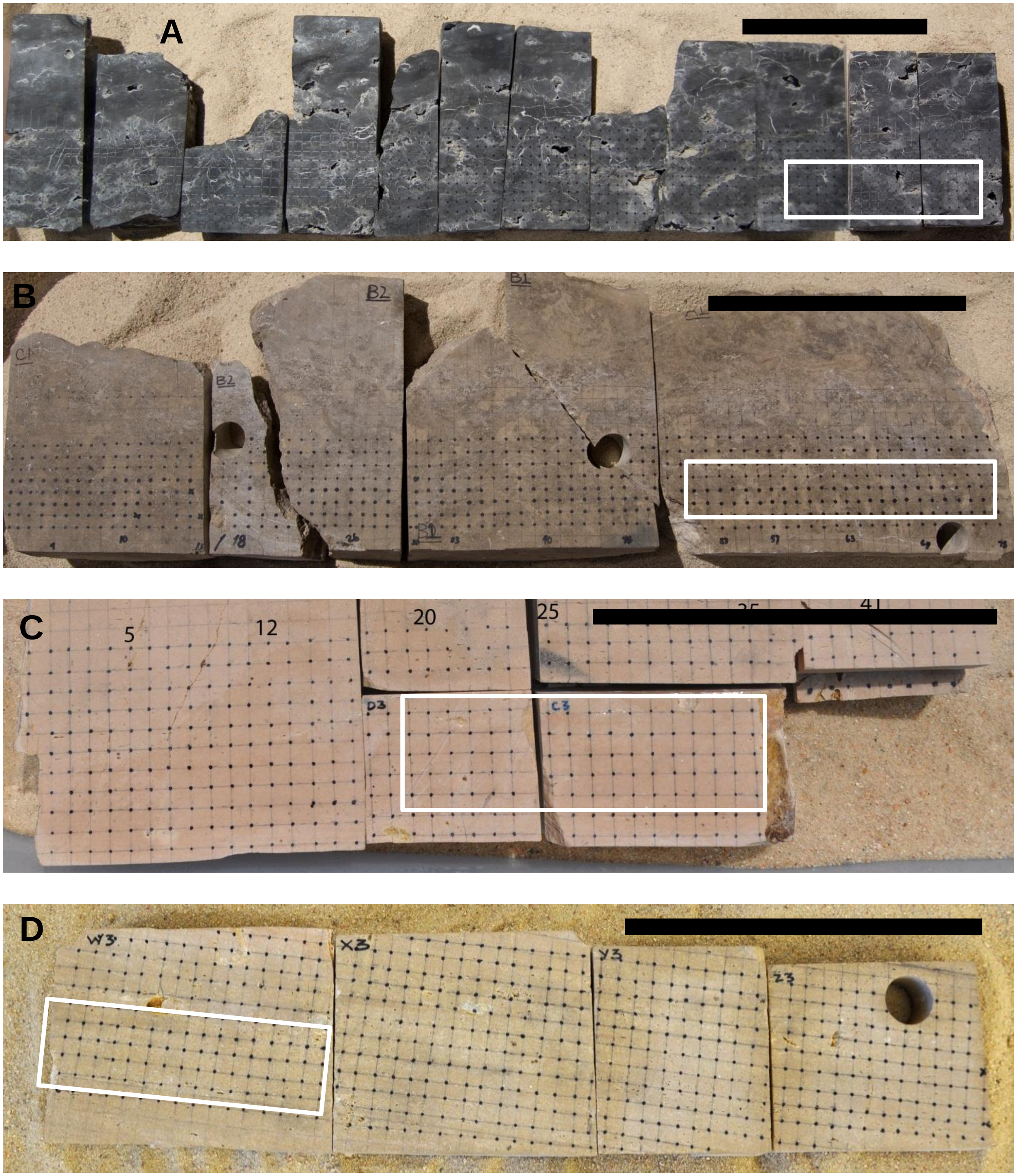

Figure 17. Continued on next page.

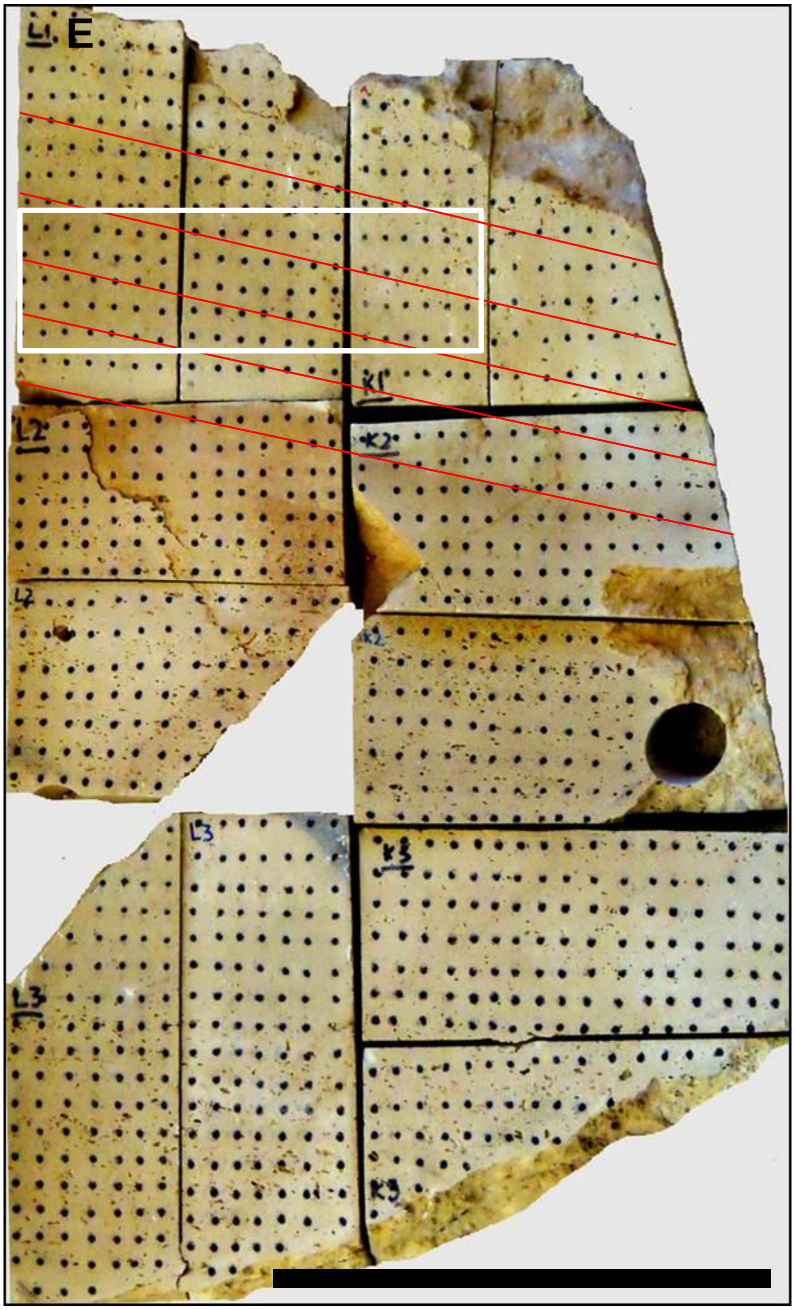

Figure 17. Five outcrop slabs studied herein: (A)Cairn, (B) Sheep, (C) Lysite BCDE, (D) Lysite WXYZ, and (E) Lysite KL. Locations of thin-sections are represented by white rectangles. Black dots are 1-cm apart on all slabs and represent points at which permeability was measured. Two of the Lysite slabs exhibit cross-bedding. The WXYZ slab was analyzed parallel to the cross-beds. The KL is cross-bedded on its upper half, as annotated by the red lines, but horizontally laminated on its lower half. All scale bars are 20cm long.

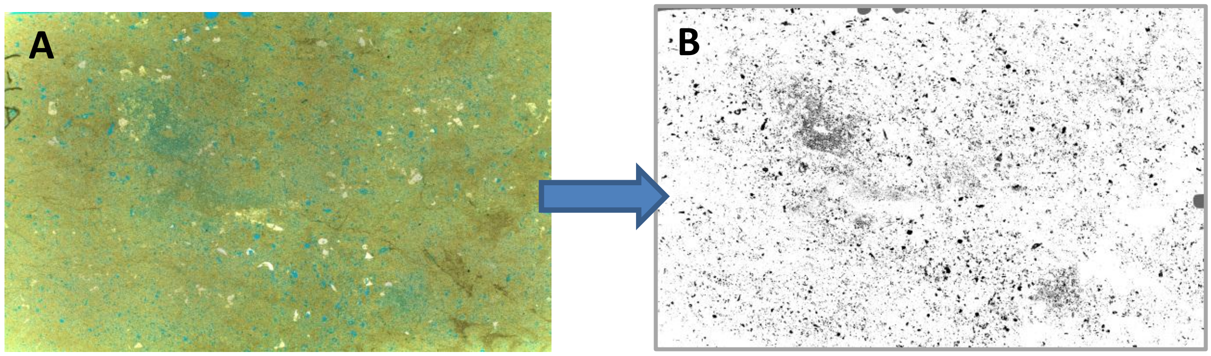

Figure 18. Example of thin-section analysis. (A) Oversized thin-section from the Sheep slab (left) has been stitched together from 12 photographs. (B) Same image with porosity converted to black and dolomite to white.

One of the issues faced with the analysis of the thin-sections was an overabundance of data due to the resolution of the photograph. The original plan was to create a variogram based on a pixel to pixel spacing, however each photomicrograph's ASCII grayscale file contained approximately 27 million pixels. With a spacing of 1-pixel, calculating an anisotropic variogram would require computing the variance for over 80 billion data pairs and an isotropic variogram would compute over 350 billion data pairs. This presented a computing problem because an isotropic variogram based on every pixel in a thin-section would theoretically take about 3 days to compute. Secondly, anything over around 20 billion data pairs required so much computer memory that the program would frequently crash.

Two solutions were identified for this computing problem. (1) Decrease the resolution of the photograph to a point at which variography could be performed on a pixel by pixel basis or (2) retain the high resolution but use a larger sampling distance (lag) to compute the variogram. There were advantages and disadvantages to both methods. The main problem with decreasing the resolution was that too much information was lost from the photograph. In particular, small features tended to be washed out. Using a larger lag also "lost" information where pixels were being skipped, but small features were not preferentially removed. Experimentation yielded positive results with a lag of 200 microns (18 pixels on the photograph) because it seemed to capture any present long range structure without also capturing noise from shorter lag distances. Thus analysis of all thin-sections used option 2.

The method for analysis of outcrop photomosaics was the same used for analysis of porosity in thin-sections. For example, Figure 19 shows a processed version of Figure 10 in which vugs have been converted to black pixels and dolomite matrix has been converted to white pixels. Since outcrop photographs were differentiated based on color, some noise may be present due to other surface features. For example, Cairn vugs were resolved based on their darker color, which could be confused with shadows on the irregular outcrop surface. Another potential source of noise is that some of the outcrop photomosaics exhibit foreshortening towards the edges of the photo. A standard sample spacing for variography was not used on the outcrop photographs because the field of view varied by location and ranged from 1 meter up to 20 meters.

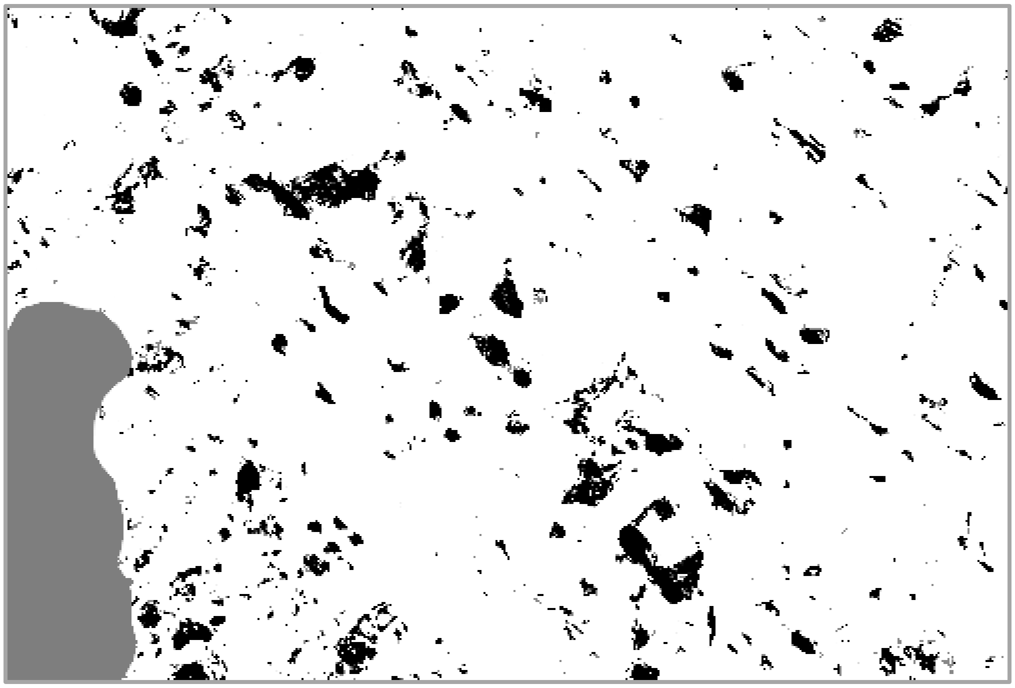

Figure 19. Grayscale processed version of Figure 10, where vugs have been converted to black pixels and dolomite matrix has been converted to white pixels. Note that the person in the bottom left corner has been converted to gray pixels, which would be counted as null data values.

Variography

Variography was performed using GS+, which is an environmental sciences geostatistics software package created by Gamma Design Software, LLC (http://gammadesign.com/). Variogram calculation is done by inserting attribute values and coordinates into the software's spreadsheet and running the variogram command. Semivariance was calculated by the equation:

$$\gamma(h) = [1 / 2N(h)]\ \Sigma\ [\ z_i - z_{i+h}\ ]^2$$

where $\gamma(h)$ is the semivariance at a given lag (h), $N(h)$ is the number of sample pairs at lag (h), z_i is the value at point (i), and z_{i+h} is the value at point (i+h). Permeability semivariance was calculated using the natural log (ln) of measured permeability values. Porosity semivariance was calculated from normalized values using the GSLIB nscore program (Deutsch and Journel, 1998). These transformations were done to avoid outliers dominating the semivariance.

An advantage of GS+ is its capability to create semivariance maps, which display semivariance as a two dimensional surface rather than as a single experimental semivariogram (e.g., Figure 1). A semivariance map is a useful geostatistical tool where there may be interesting heterogeneities to quantify in more than just the lateral direction. For example, Figure 20A shows a grid of porosity values, the horizontal anisotropic semivariogram (Figure 20B), and the semivariance map (Figure 20C). The anisotropic semivariogram captures the correlation range of 10 mm and small hole effects in the horizontal direction. The semivariance map depicts heterogeneity at all angles, not just the horizontal (0°) captured by the anisotropic semivariogram. Semivariance is depicted on the map with hot colors (i.e., pink, red, orange) associated with high variance and cool colors (i.e., green, blue) associated with low variance. The semivariance map is always interpreted from the origin (0,0) such that the anisotropic semivariogram corresponds with a horizontal line through the center of the map (Figure 20C). Semivariance can be assessed at any angle between +90° (vertically up) and -90° (vertically down). Since this thesis is concerned with lateral variability, the semivariance map is used as a check on how representative the horizontal anisotropic semivariogram is of subhorizontal variability in general. Each semivariance map presented in this thesis will show the anisotropic semivariogram as a black horizontal line. For comparison to subhorizontal variability, lines at +10° and -10° will be shown on either side of the anisotropic semivariogram (e.g. Figure 20C). Semivariance maps were calculated for the photomicrographs and outcrop photomosaics. Outcrop slabs lacked sufficient data in the vertical direction for variance mapping.

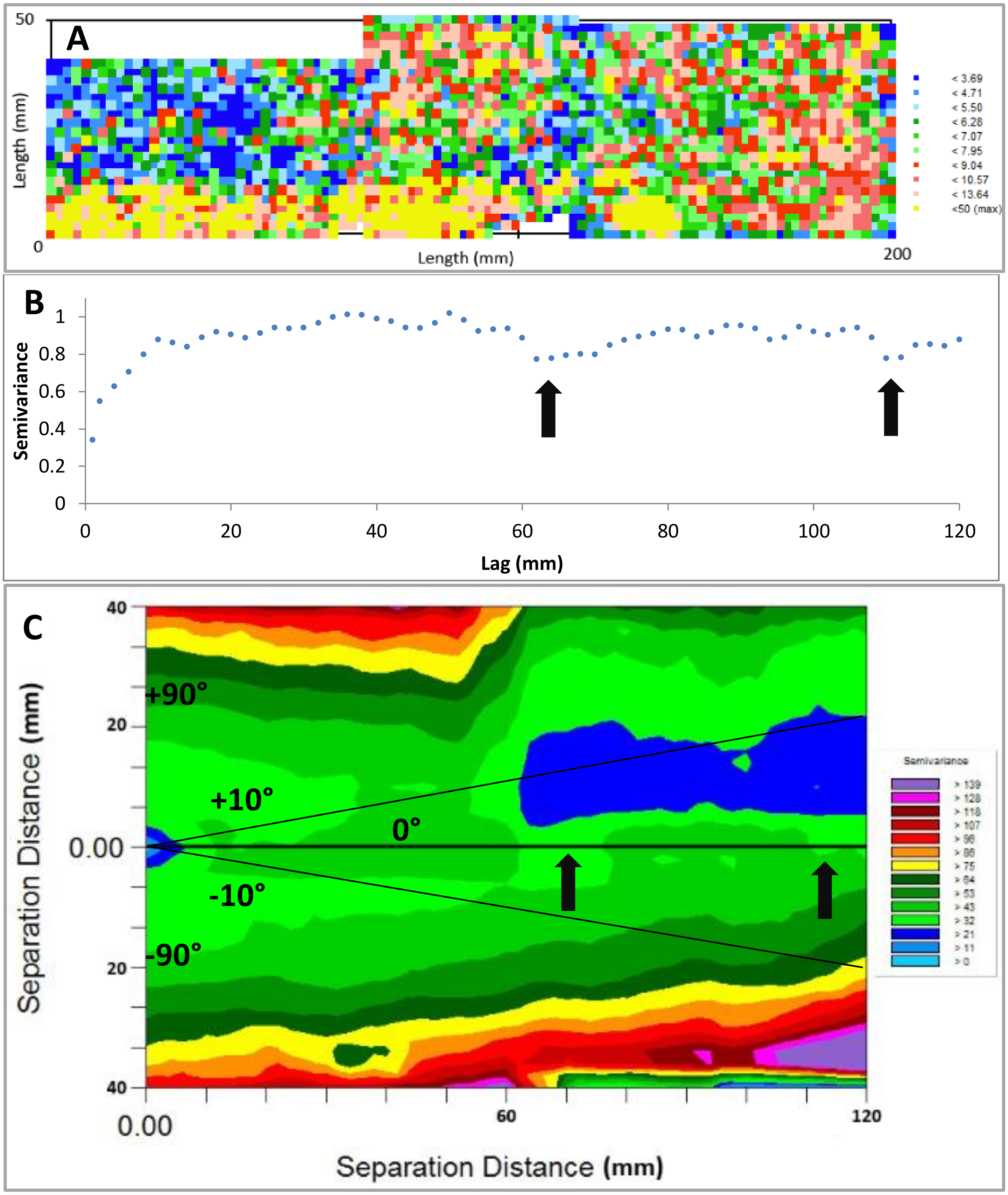

Figure 20. (A) Grid of porosity values with spatial heterogeneity. (B) Horizontal snisotropic semivariogram of that porosity data. Range is ~12 mm. Hole effects are marked by black arrows and have a wavelength of 50 mm. (C) Semivariance map calculated in all directions from values in porosity grid. Horizontal black line (0°) represents the anisotropic variogram shown in B with hole effects marked by black arrows. Diagonal black lines represent 10° divergence on either side of the anisotropic semivariogram. In this case, the anisotropic semivariogram resembles the semivariance map in the +10° direction, but the -10° direction differs because there are no hole effects and there is a long-range trend of constantly increasing variance.

CHAPTER 3: BACKGROUND GEOLOGY

Madison Formation Geology

The Madison Formation was formed on a shallow carbonate ramp during the early to middle Mississippian (Smith et al., 2004). This was a broad carbonate ramp (Figure 21) that covered an area from New Mexico to Western Canada (Sonnenfeld, 1996). The ramp was bound by the Antler highlands on the West and the Transcontinental Arch to the east (Smith et al., 2004). The Madison Formation is interpreted as being one second-order sequence, which is further subdivided into six third-order sequences and even higher frequency depositional cycles (Sonnenfeld, 1996). The intervals of interest for this study are the 1st and 2nd third-order sequences as defined by Sonnenfeld (1996). The bioturbated skeletal dolowackestone sampled at Sheep Canyon, is interpreted to have been deposited in a middle ramp setting as part of Sequence 1's transgressive systems tract (Smith et al., 2004). The skeletal dolograinstone sampled at Lysite Mountain is interpreted to be part of a high-energy shoal deposited in the highstand systems tract of Sequence II (Smith et al., 2004; Pranter et al., 2006). The majority of dolomite in Sequences I and II was interpreted by Sonnenfeld (1996) to be the result of early dolomitization by refluxing evaporative brines. Evidence for this conclusion is based on relatively heavy whole-rock $\delta^{18}O$ values and widespread evaporative lagoon deposits at the base of Sequence III (Sonnenfeld, 1996; Smith et al., 2004). Smith et al. (2004) also suggested there was some early burial dolomitization, as evidenced by clear rims on dolomite rhombs, coarse void-filling dolomite crystals, and negative $\delta^{18}O$ values, although these burial dolomites are comparatively minor (Smith et al., 2004). In contrast, Budai et al. (1987) suggested that there were two stages of dolomitization, an early hypersaline reflux stage followed by a volumetrically dominant meteoric mixing stage driven by transgressive-regressive cycles across the Madison shelf. Most recently, Katz (2008) interpreted Madison dolomite as having formed early by altered seawater, followed by dolomite recrystallization in the deep-burial setting as evidenced by high $^{87}Sr/^{86}Sr$ ratios. Katz (2008) also found evidence for a volumetrically significant phase of hydrothermal dolomitization in Sequences I and II, which is evidenced by coarse-crystalline, geochemically zoned crystals with high-temperature fluid inclusions. These hydrothermal dolomites are easily distinguished on outcrop and where not present at the Lysite Mountain and Sheep Canyon sample sites (Budd, pers. comm.)

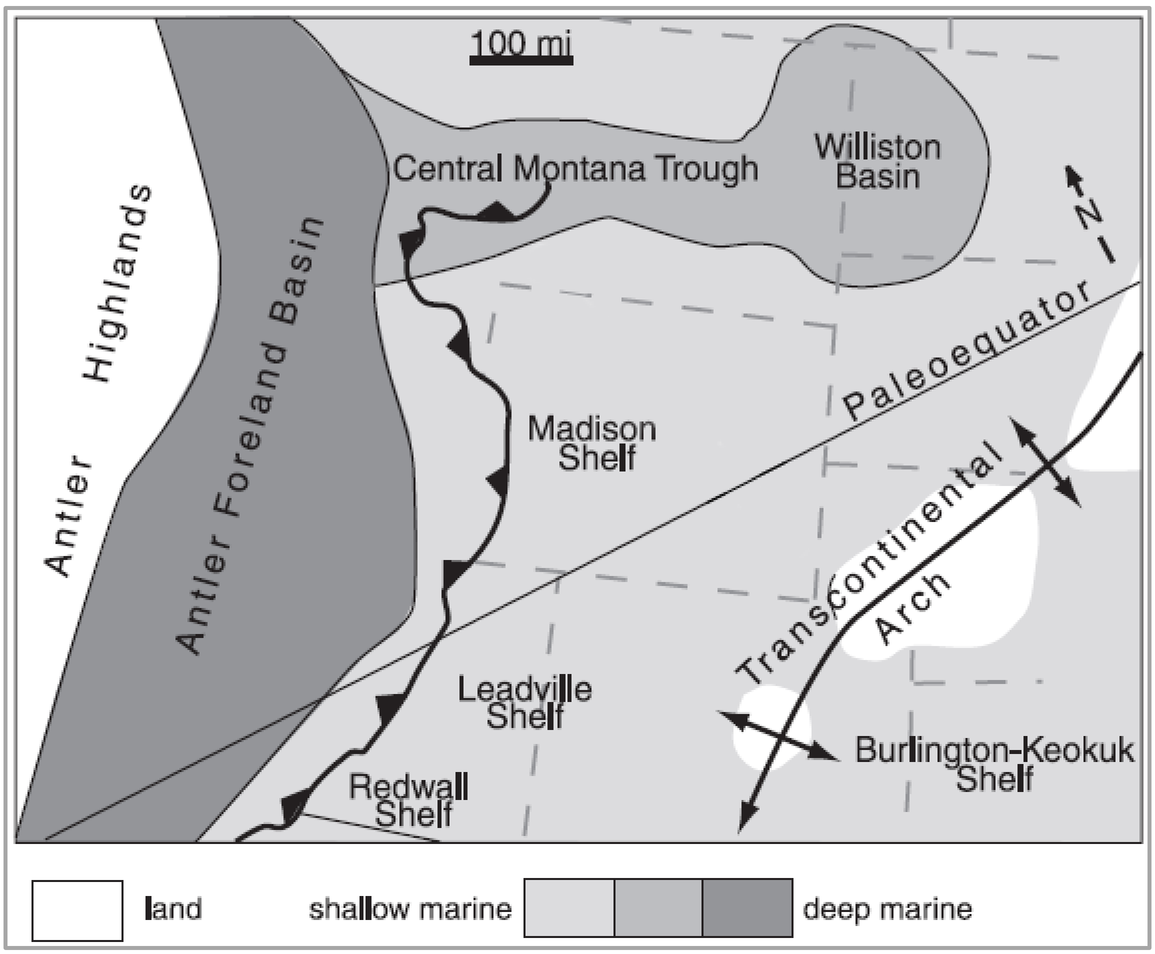

Figure 21. Regional paleogeography of the Madison shelf during Mississippian time. The shelf was bound by the Transcontinental Arch, the Central Montana Trough and the Antler Foredeep and sat a few degrees north of the paleoequator. (Smith et al., 2004)

Petrographically, the Lysite slabs are cross-bedded sucrosic euhedral dolograinstones. Porosity is primarily composed of moldic dissolution voids and intercrystalline porosity (Figure 22), although there is very minor intracrystalline porosity as well. Crystal sizes range from a few tens of microns to several hundred microns with average crystal sizes around 80 microns. Crystals are cloudy with inclusions, which generally suggests one generation of dolomite growth, although there is some evidence of a later phase of dolomitization where there are clear rims surrounding inclusion-rich dolomite cores (Figure 23). Dolomitization was mainly fabric destructive, although there are occasional ghosts of skeletal grains (Figure 24). The KL slab in particular has common ghost fabrics of brachiopods, crinoids, and red algae. These ghost fabrics are visible because the replacive dolomite crystals are generally smaller in the precursor grains than in the intervening originally interparticle pore space.

Petrographically, the Sheep slab is a sucrosic, euhedral to subhedral dolowacketone. Porosity is primarily intercrystalline and moldic, with both being of approximately equal volume. Crystal sizes range from about 20-50 microns, with most crystals being close to 50 microns. Bioturbation has played a role in the distribution of porosity and crystal size. Burrows are common and can be seen in both the slab (Figure 14) and thin-sections (Figure 25). Burrows are typically about 5-10 mm across, several centimeters in length and are circular or cylindrical in shape. Most burrow infillings have only intercrystalline porosity and moldic pores adjacent to the burrows are commonly filled with calcite (Figure 25), which formed as a late burial cement (Smith et al., 2004).

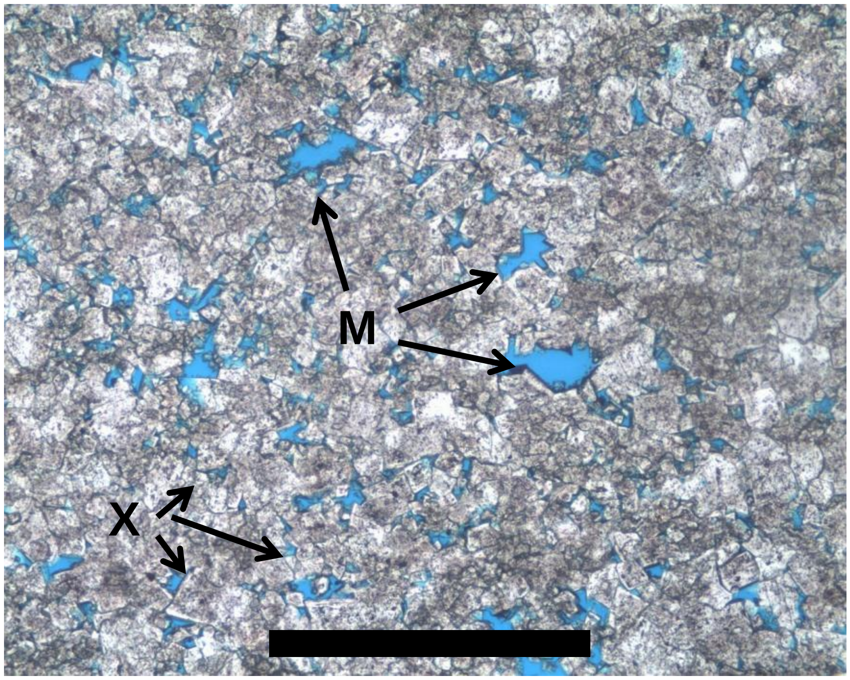

Figure 22. Thin-section photomicrograph of a Madison dolograinstone. (M) moldic pores and (X) Intercrystalline pores are illustrated. Scale bar is 1mm.

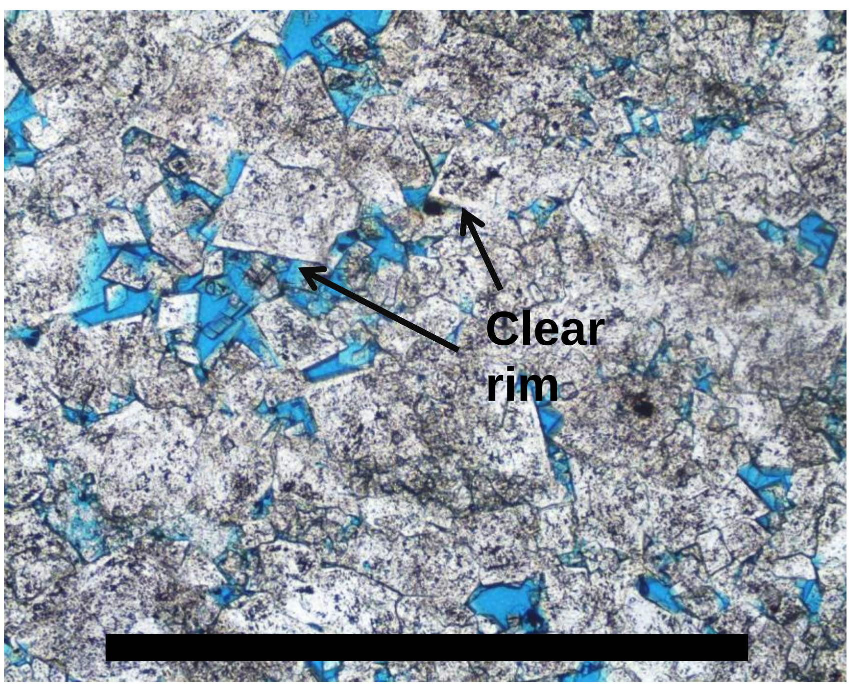

Figure 23. Thin-section photomicrograph of a Madison dolograinstones illustrating the dominance of inclusion-rich dolomite crystals that occasionally exhibit clear rims (arrows). Scale bar is 1mm.

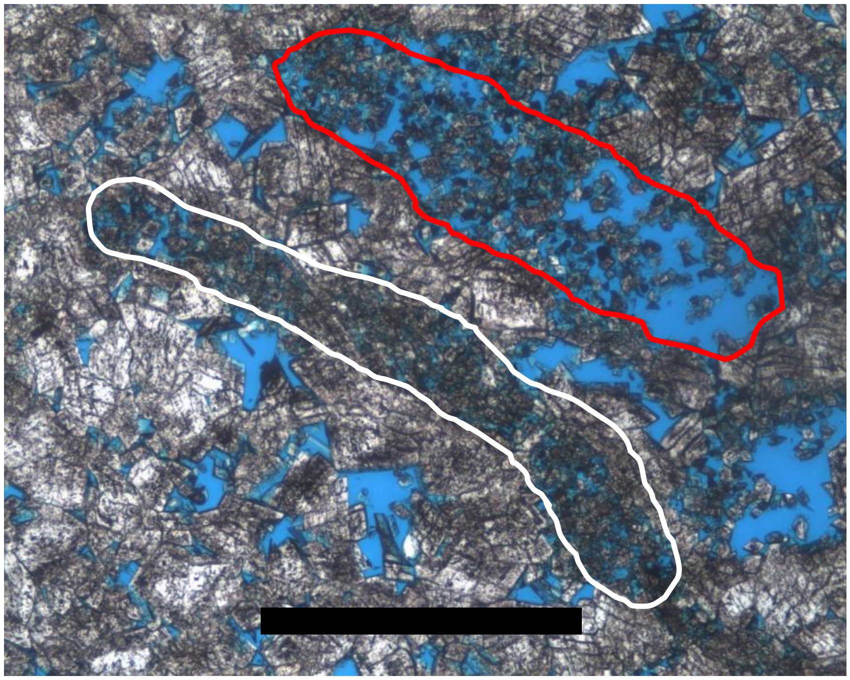

Figure 24. Thin-section photomicrograph of ghost fabrics (outlined in white and red) of former skeletal grains in a Madison dolograinstone. Ghost fabrics are visible where skeletal grains have been replaced and the dolomite crystals are inclusion rich or from a skeletal mold (red outline). Scale bar is 1mm.

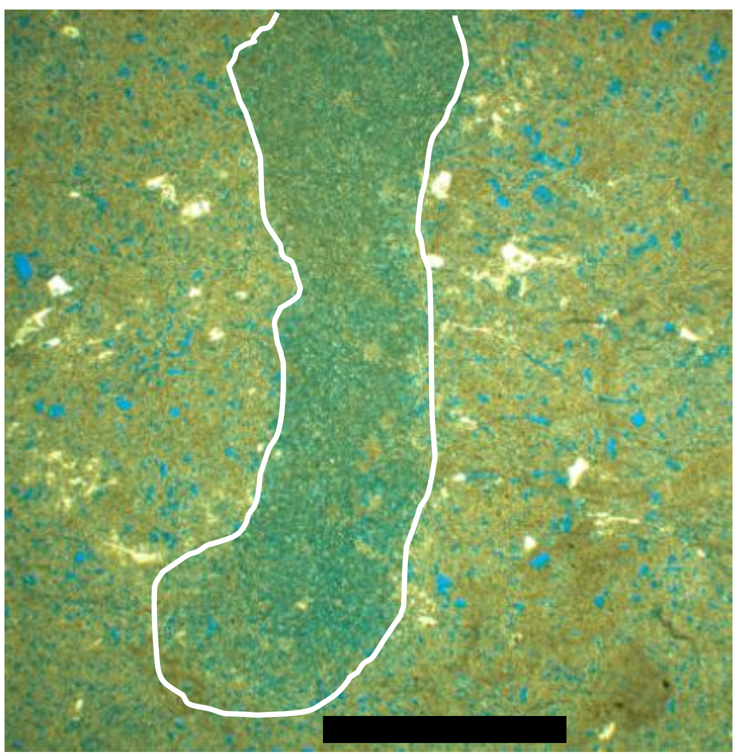

Figure 25. Thin-section photomicrograph illustrating bioturbation in a Madison dolowackestone. The burrow (white outline) is filled with fine crystalline, inclusion-rich dolomite. The surrounding dolomite matrix is slightly coarser crystalline, contains small moldic pores, and calcite cement (white crystals). Scale bar is 6mm.

Cairn Formation Geology

The Cairn Formation was deposited as a part of the Southesk-Cairn Carbonate Complex (Figure 26), which was a series of biostromal mounds and carbonate buildups on a large carbonate shelf that comprises the Cooking Lake Formation (Vandeginste et al., 2009a). These biostromes were in a restricted platform setting, landward of the Cooking Lake margin (McNamara et al., 1991). The Cairn Formation can be further broken down into two members, the lower Flume Member and the Upper Cairn Member. This thesis sampled the Upper Cairn Member, which was deposited as stromatoporoid boundstones and *Amphipora* floatstones in a stable subtidal setting (Vandeginste et al., 2009a). In the subsurface, the Upper Cairn Member is equivalent to the Leduc Formation, an important hydrocarbon reservoir which is ultimately expected to produce 3.1 billion bbl of oil and 9.4 tcf of gas (Vandeginste et al., 2009b; Atchley et al., 2006).

Most studies of Devonian carbonates in the Alberta Basin have interpreted the dolomitization process as occurring during shallow burial between 500-2000 meters (Buschkuehle et al., 2002; Machel et al., 2008; Vandeginste et al., 2009b). Evidence for this is the apparent coeval relationship with stylolitization (Machel, 2008), depleted $\delta^{18}O$ values (Machel et al., 2008; Vandeginste et al., 2009b), and $^{87}Sr/^{86}Sr$ data (Buschkuehle et al., 2002) indicative of hot, radiogenic fluids. However, as shown in Figure 27, the Southesk-Cairn Complex was subject to a very complex diagenetic history, with multiple phases of dissolution and recrystallization of dolomite (Machel et al., 2008). Large moldic pores (Figure 10) developed during and after dolomitization where calcitic stromatoporoids were leached, although some stromatoporoids remain calcite filled. These molds are generally 10-20 cm

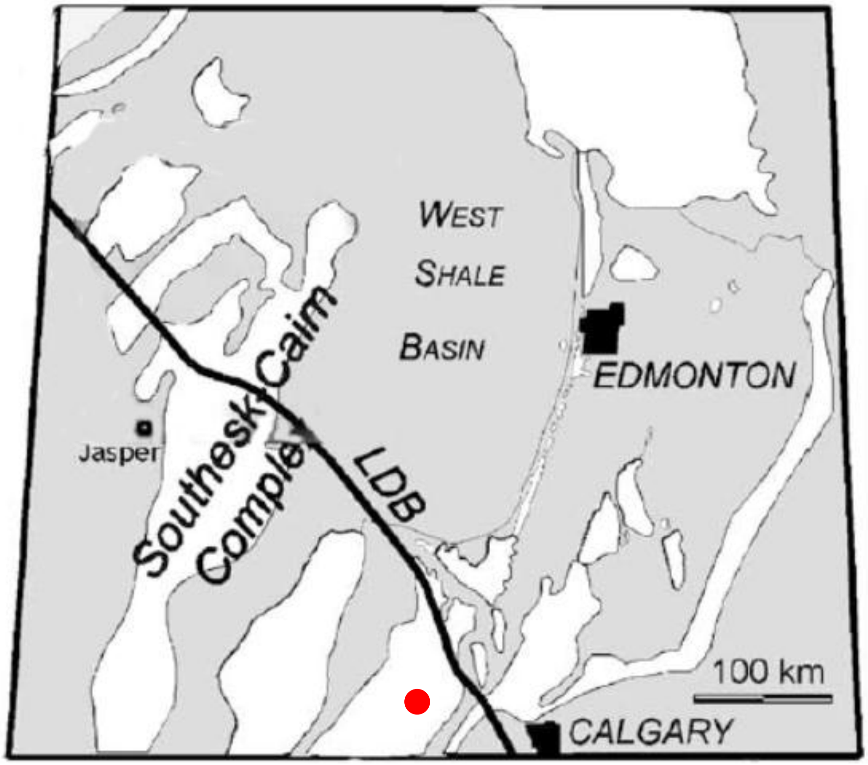

Figure 26. Regional paleogeography of the Southesk-Cairn carbonate complex in white bound by the West Shale Basin in gray. The Cairn Formation was sampled at the red dot on the map, a location now outcropping at Grassi Lakes, Alberta. LDB is the limit of the disturbed belt. Modified from Buschkuele and Machel (2002)

PHASE	---- TIME ---->	STAGE
1	Micrite envelopes	I
2	Anhydrite I, Dolomite I	
3	Dissolution I	
4	Pyrite I	
5	Calcite I	
6	Calcite II	
7	Calcite III	
8	Calcite IV	
9	Dolomite II	II
10	Dissolution II	
11	Pressure solution	
12	Dolomite III	
13	Pyrite II	
14	Fractures I	
15	Calcite V	
16	Secondary anhydrite	
17	Fractures II	III
18	Hydrocarbons	
19	Fractures III, Dissolution III	IV
20	Dolomite IV and V	
21	Elemental sulfur	
22	Calcite VI, Calcite VII	
23	Pyrite III, Sphalerite	
24	Fractures IV, Tertiary anhydrite	V

Figure 27. Complex diagenetic history for the Southesk-Cairn Carbonate Complex, which was subject to up to five different phases of dolomitization, from Machel et al. (2008).

wide, but are occasionally larger (Machel et al., 2008; Mcnamara et al., 1991).

In thin-section, the Cairn Formation slab from Grassi Lakes consists of a dark matrix dolomite and lighter dolomitized skeletal grains (in particular stromatoporoids). Large moldic pores are common where skeletal grains have been dissolved, although the moldic pores are frequently lined with large subhedral crystals of clear saddle dolomite (Figure 28). Matrix dolomite tends to be anhedral cyrstals typically about 50 microns or less in size. Dolomitized skeletal grains tend to be composed of larger, subhedral crystals that are generally 100-200 microns in size (Figure 29). Stylolites are common and are typically marked by accumulation of dark organic material (Figure 30). Parting has also occurred along many stylolites, resulting in linear porosity conduits (Figure 30). Stromatoporoid moldic pores are interconnected by these stylolite conduits (Figure 31).

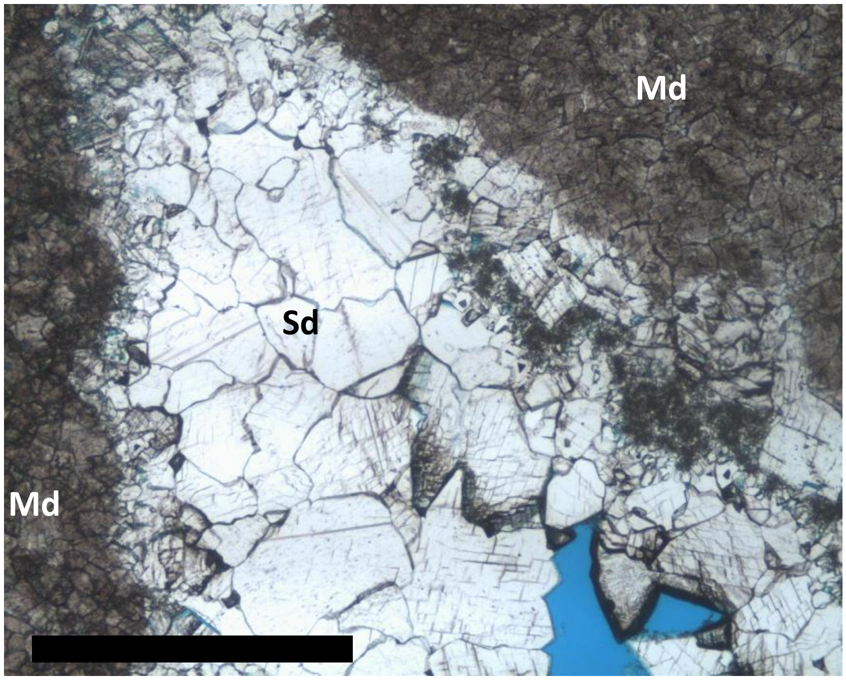

Figure 28. Thin-section photomicrograph showing stromatoporoid mold that has been partially occluded by saddle dolomite (Sd) and is surrounded by inclusion-rich matrix dolomite (Md). Matrix dolomite represents diagenetic phase 9 (Dolomite II) in Figure 27. Saddle dolomite represents diagenetic phase 20 (Dolomite IV and V) in Figure 27. Scale bar is 1mm.

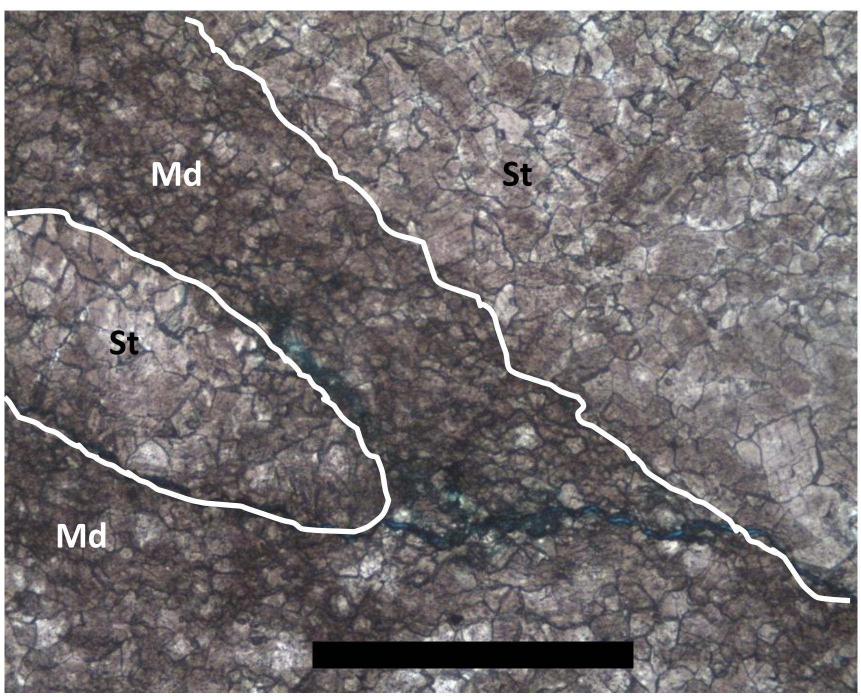

Figure 29. Thin-sectin photomicrograph showing dark matrix dolomite (Md) of anhedral, 50 micron sized crystals and replaced stromatoporoids (outlined in white) consisting of subhedral, 100-200 micron sized crystals (St). Scale bar is 1mm.

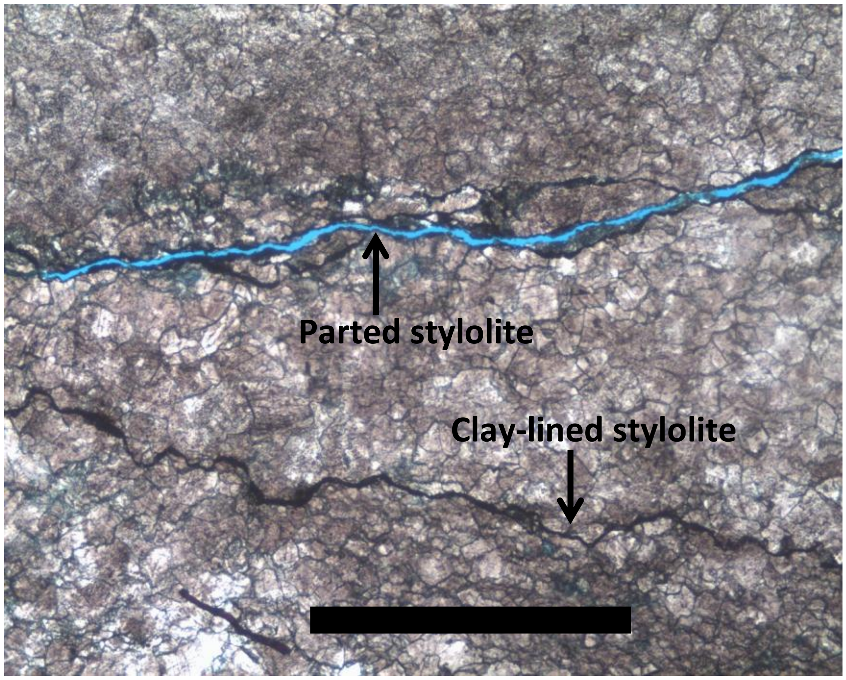

Figure 30. Thin-section photomicrograph showing a stylolite lined with clay and a parted stylolite that forms a porosity conduit. Scale bar is 1mm.

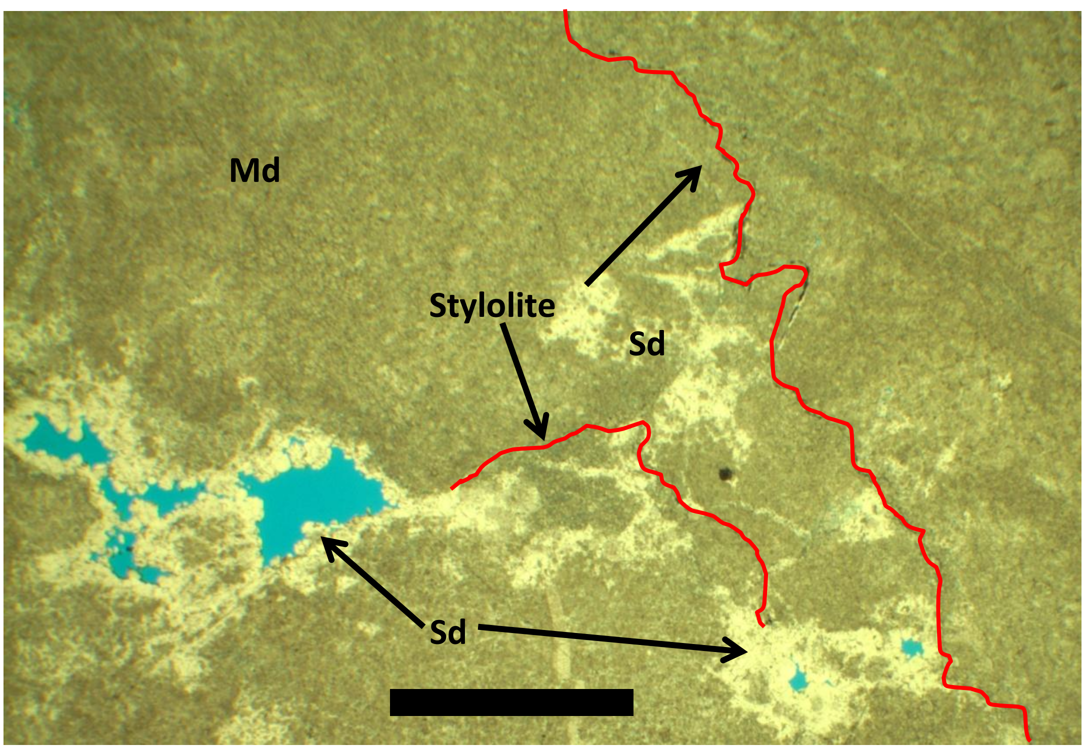

Figure 31. Thin-section photomicrograph showing stylolites (traced in red) that act as conduits between moldic pores. Inclusion-rich matrix dolomite (Md) dominates volumetrically. Light-colored saddle dolomite (Sd) lines or fills molds. Scale bar is 6mm.

San Andres and Tansill Formation Geology

The San Andres Formation and Tansill Formation are both Permian carbonates that formed in the Permian Basin. The Wolfcampian-Leonardian-Guadalupian section of the Permian Basin is subdivided into fourteen composite sequences and these fourteen composite sequences are further subdivided into 4^{th} order high-frequency depositional sequences (Kerans and Fitchen, 1995). The San Andres Formation comprises composite sequences 9 and 10, each recording a third-order rise and fall of sea level across a carbonate ramp (Kerans and Fitchen, 1995). The San Andres was deposited in a shallow, arid setting. Restricted areas of the ramp were composed of evaporative deposits, and carbonate deposition dominated the seaward margin (Figure 32) (Meissner, 1972). Dolomitization is interpreted to have occurred as refluxing brines mixed with meteoric groundwater, thus setting up convective circulation (Garcia-Fresca, 2009; Garcia-Fresca et al., 2012). These evaporative brines were periodically fed by marine flooding via storms. Over time, falling sea levels drove seaward progradation of the brine source areas and thus dolomitizing fluids were transported through the entire platform (Garcia-Fresca, 2009; Kerans and Fitchen, 1995). At the base of the dolomitized section, dolomitization produced pods of dolomite in limestone. The pods are centimeters to meters wide (Figure 33).

The younger Tansill Formation records the 14^{th} composite sequence in the Permian strata (Kerans and Fitchen, 1995; Frost et al., in press). The Tansill Formation represents the final phase of reef and platform building within the Permian Basin and contains synsedimentary fractures that are parallel to the platform margin trend. Strataform dolomite and a fracture-related dolomite are both present in the outer-shelf Tansill deposits exposed in Dark Canyon, NM (Frost et al., in press). The synsedimentary fractures played an important role in the

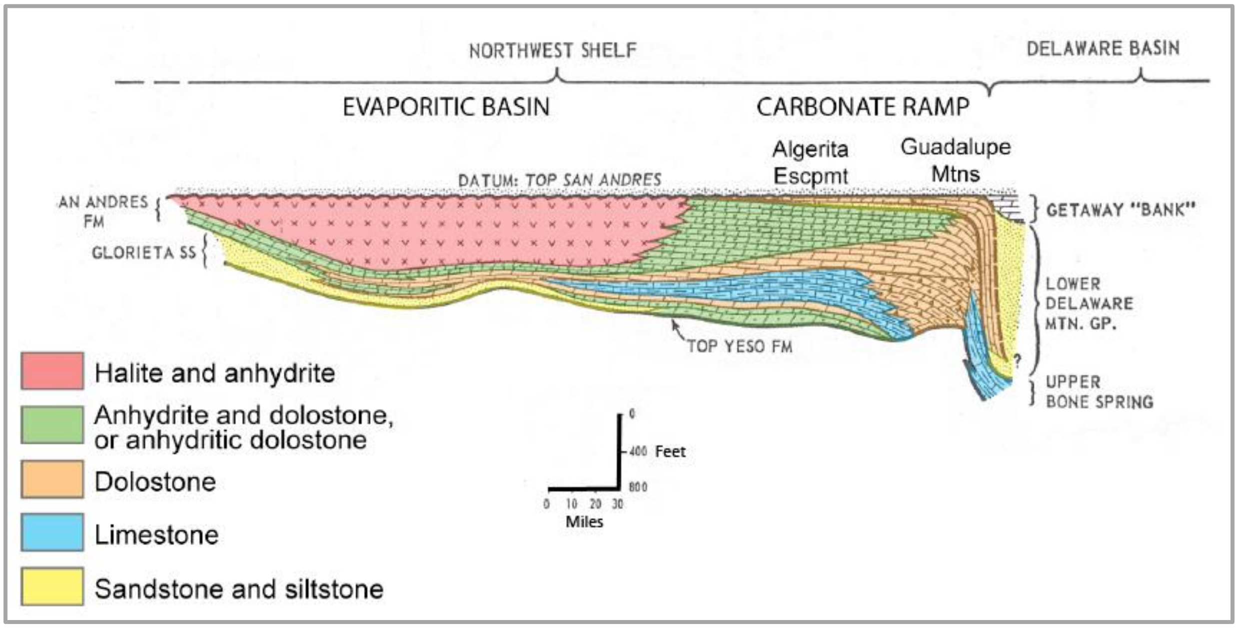

Figure 32. Regional cross section of the San Andres Formation showing landward restricted evaporative deposits and seaward carbonate ramp. (From Garcia-Fresca, 2009 after Meissner, 1972)

Figure 33. Outcrop photo showing dolostone pods (red-brown) interfingering with limestone (gray) in the San Andres Formation. Rock hammer for scale.

dispersal of dolomitizing fluids, which were formed as hypersaline brines in the backreef setting that then refluxed through the permeable substrate and the fracture network (Melim and Scholle, 2002; Frost et al., in press). An interpretation of early dolomitization by refluxing seawater brines is supported by the fact that dolomitization predates all diagenetic events aside from early marine cementation (Frost et al., in press). The fracture-related dolomite bodies extend away from their fracture source and consist of irregular, coalescing pods of dolomite (Figure 34). As described by Frost et al. (in press), the largest bodies are 10s of centimeters to 5 meters thick and 10s of meters long, do not necessarily replace all the limestone in a bed, and have smaller (~5 cm to 1 m wide), spherical to elliptical, bodies below and at the down-dip margins of the larger bodies.

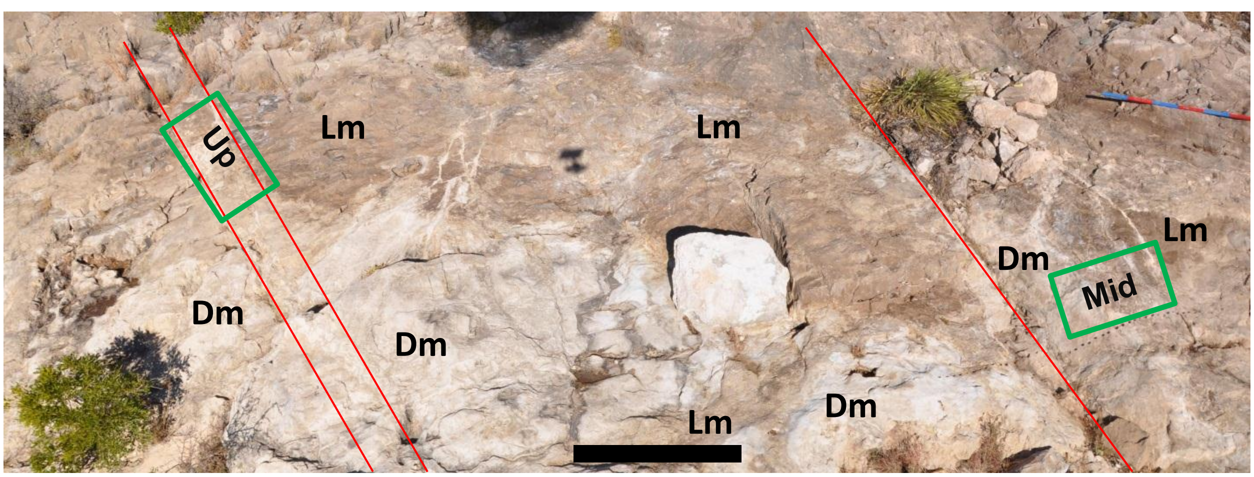

Figure 34. Outcrop photomosaic showing dolostone pods (Dm) and limestone (Lm). Dolomite originates at fractures (red lines) and coalesces into larger pods. The green boxes represent the areas where the "midstream" and "upstream" photomosaics were taken for the Tansill Formation. Scale bar is 2 meters.

CHAPTER 4: RESULTS

Results are presented on a slab by slab basis, first with results of the petrophysical and thin-section attributes of each slab, and then the variography of each slab. This is followed by variography from the outcrop photomosaics of the Cairn, Tansill, and San Andres formations. Figure 35 shows porosity-permeability crossplots for all of the collected slab data. A summary of all variography results discussed herein is presented in Table 2.

Slab Data

BCDE Observations

The BCDE slab was analyzed for permeability on a 47 cm by 10 cm grid and contained 347 data points and 123 null data points (Figure 17). The mean, median, minimum and maximum permeability are 15.1, 9.3, 4.9, and 188 mD respectively. The BCDE slab's porosity grid is 25 cubes by 6 cubes, which yields a possible 150 data points of which 132 were measurable. The mean, median, minimum, and maximum porosities are 12.8, 12.7, 7.2, and 18.6% respectively. Across the slab, both porosity and permeability show alternating horizontal bands of higher and lower values (Figure 36), with bands reflecting the horizontal laminations across the slab.

The BCDE thin-section transect (Figures 17 and 37) is comprised of a grid of 225,972 points. There are 18,871 porosity points, 201,884 dolomite points, and 5,217 null data points. This gives a porosity value of 8.5% for the entire thin-section. The average slab porosity from the same exact area is 12.4%. The discrepancies in values in this and all other slabs could be a result of higher porosity in the third dimension of the cubes (i.e., a pore volume) as opposed to the thin-section, which is a measure of porosity in just two dimensions (i.e., a pore area).

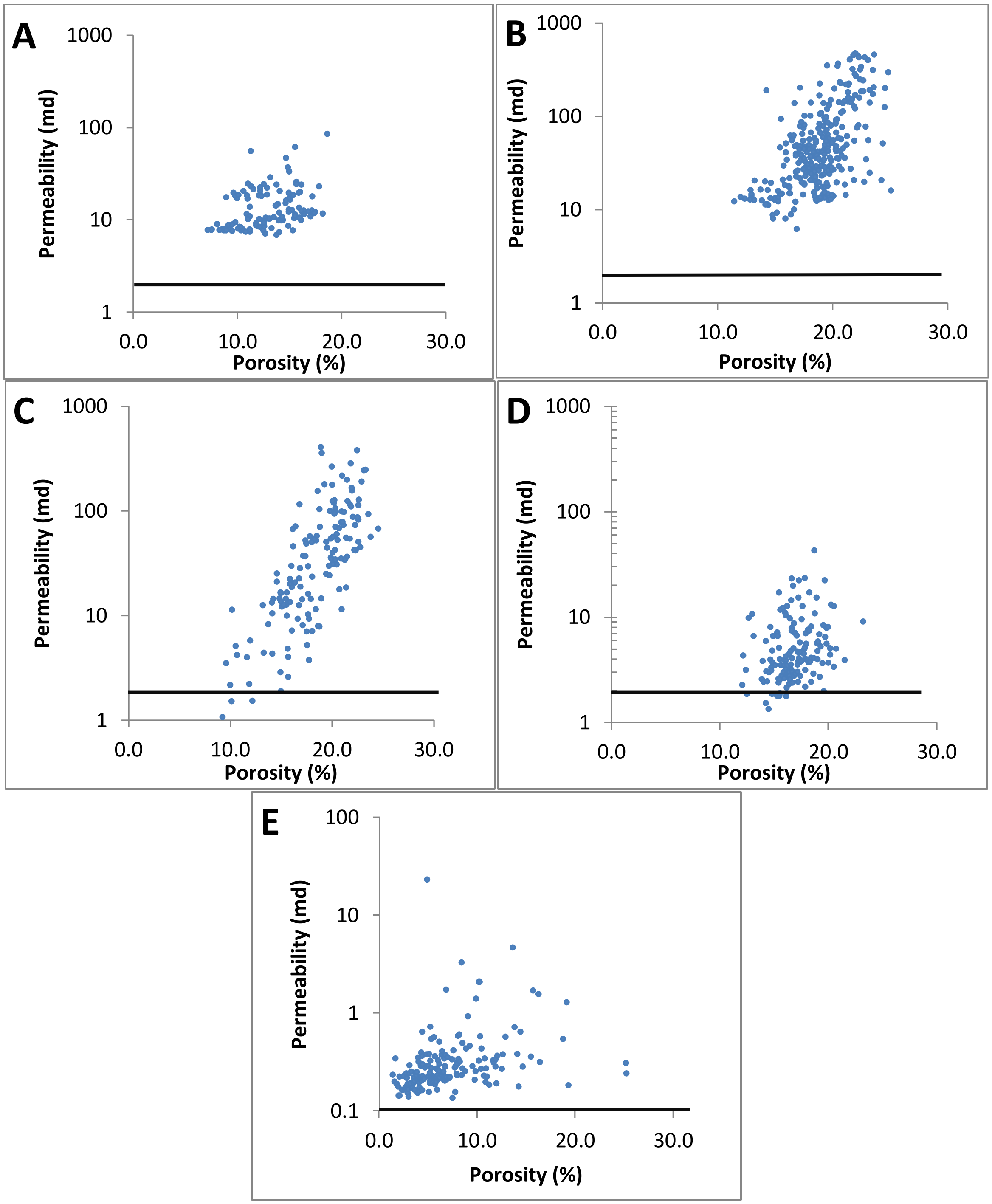

Figure 35. Porosity and permeability crossplots for all slabs: (A) BCDE, (B) KL, (C) WXYZ, (D) Sheep, and (E) Cairn. Two of the Lysite dolograinstones (slabs B and C) show the strongest correlation between porosity and permeability; the Sheep and Cairn slabs both show more scatter. Detection limits are denoted by the horizontal black line on each plot.

Source	Variable	Variogram Type	Sample Spacing (cm)	Range (cm)	Hole-Effect wavelength (cm)	**Hole amplitude % of total variance**	Transect Length (cm)
BCDE slab	Permeability	Continuous	1	-	-		46
BCDE slab	Porosity	Continuous	2	4	20	7%	46
BCDE thin-section	Porosity	Indicator	0.02	0.4	4.6	3.5%	21
KL slab	Permeability	Continuous	1	13	-		32
KL slab	Porosity	Continuous	2	-	-		32
KL thin-section	Porosity	Indicator	0.02	0.2	-		21
WXYZ slab	Permeability	Continuous	1	8	29	30%	54
WXYZ slab	Porosity	Continuous	2	20	20	40%	54
WXYZ thin-section	Porosity	Indicator	0.02	0.25	-		15
Sheep slab	Permeability	Continuous	1	4	-		76
Sheep slab	Porosity	Continuous	2	-	22	20%	76
Sheep thin-section	Porosity	Indicator	0.02	0.2	-		21
Cairn slab	Permeability	Continuous	1	10	30	25%	109
Cairn slab	Porosity	Continuous	2	10	-		109
Cairn thin-section	Porosity	Indicator	0.02	0.5	2.9	7%	21
Cairn outcrop D	Macropore	Indicator	2.5	20	320	4%	823
Cairn outcrop E	Macropore	Indicator	2.5	10	-		2012
Cairn outcrop H	Macropore	Indicator	3	20	-		549
Tansill downstream	Lithology	Indicator	4.5	230	560	8%	335
Tansill midstream	Lithology	Indicator	0.2	15	-		75
Tansill upstream	Lithology	Indicator	0.3	5	-		137
San Andres outcrop A	Lithology	Indicator	2.5	25	70	6%	549
San Andres outcrop B	Lithology	Indicator	0.9	50	220	8%	1158

Table 2. Summary of variography results for all slabs, thin-sections and outcrop photomosaics. Data are listed in the same order as they are presented in the text

Experimental semivariograms were created for the BCDE slab's permeability, porosity, and the thin-section porosity. The BCDE experimental permeability semivariogram (Figure 38A) defines a trend with no correlation range, sill, or discernible hole-effects. Forty-five percent of the total semivariance occurs at the nugget and the balance occurs in the long-range trend. The experimental semivariogram of BCDE porosity (Figure 38b) has a modeled nugget of 0 and the correlation range is at 4 cm. There are two hole-effects with amplitudes equivalent to 7% of the total semivariance occur at lags of 16 and 36 cm (wavelength of 20 cm). The experimental semivariogram for thin-section porosity (Figure 38C) exhibits a modeled nugget of 0 and a correlation range of 4 mm. There are four hole-effects at 23 mm, 67 mm, 117 mm, and 151 mm. When fit with a hole-effect variogram model, the wavelength of these hole-effects is 46 mm and the amplitude is 3.5% of the total semivariance. The semivariance map (Figure 38D) shows vertical (green) bands of similar variance reflecting the hole-effects seen in the anisotropic semivariogram (Figure 38C). As a result, the semivariance in subhorizontal directions (±10°) is very similar to the anisotropic semivariogram. Thus, the anisotropic semivariogram is representative of all lateral transects.

KL Observations

The KL slab was analyzed for permeability on a 32 cm by 44 cm grid and contained 908 data points and 500 null data points (Figure 17). The mean, median, minimum and maximum permeability are 72.6, 30.6, 1.7, and 754 mD respectively. The KL slab's porosity grid is 17 cubes by 25 cubes, which yields a possible 425 data points of which 307 were measureable. The mean, median, minimum, and maximum porosities are 18.9, 18.9, 11.5, and 26.6%

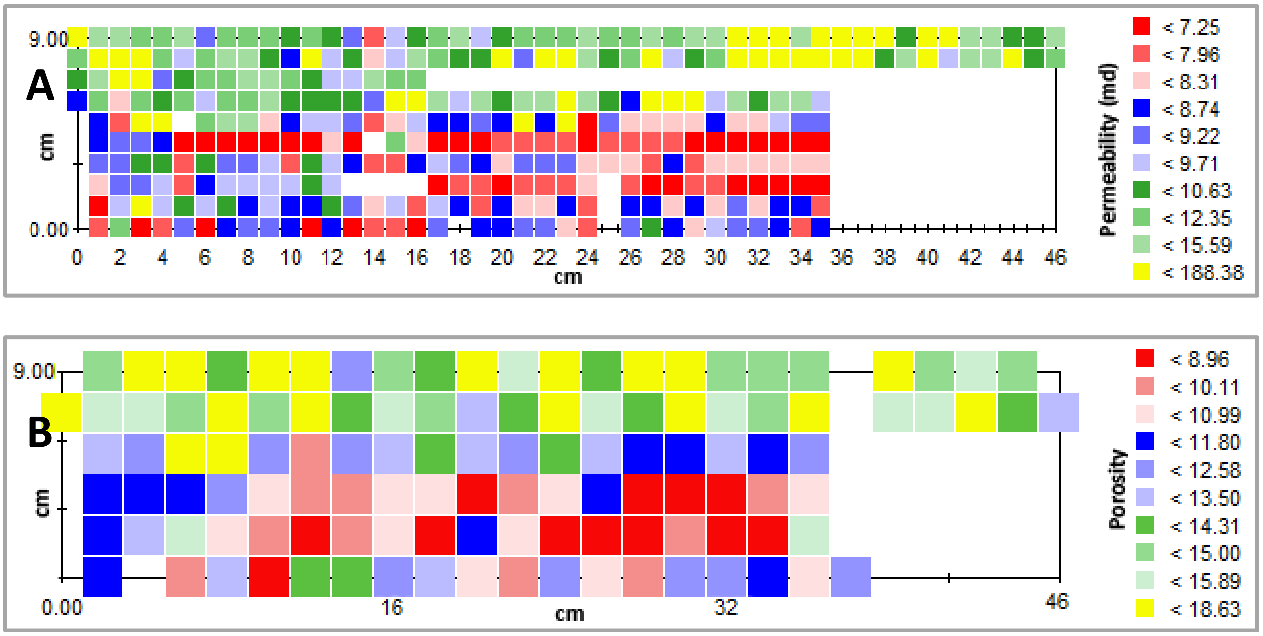

Figure 36. Pixel plots showing the distribution of (A) permeability and (B) porosity on the BCDE slab. Both attributes exhibit low values on the lower half of the slab and high values on the upper half of the slab, a pattern that parallels the horizontal laminations across the slab.

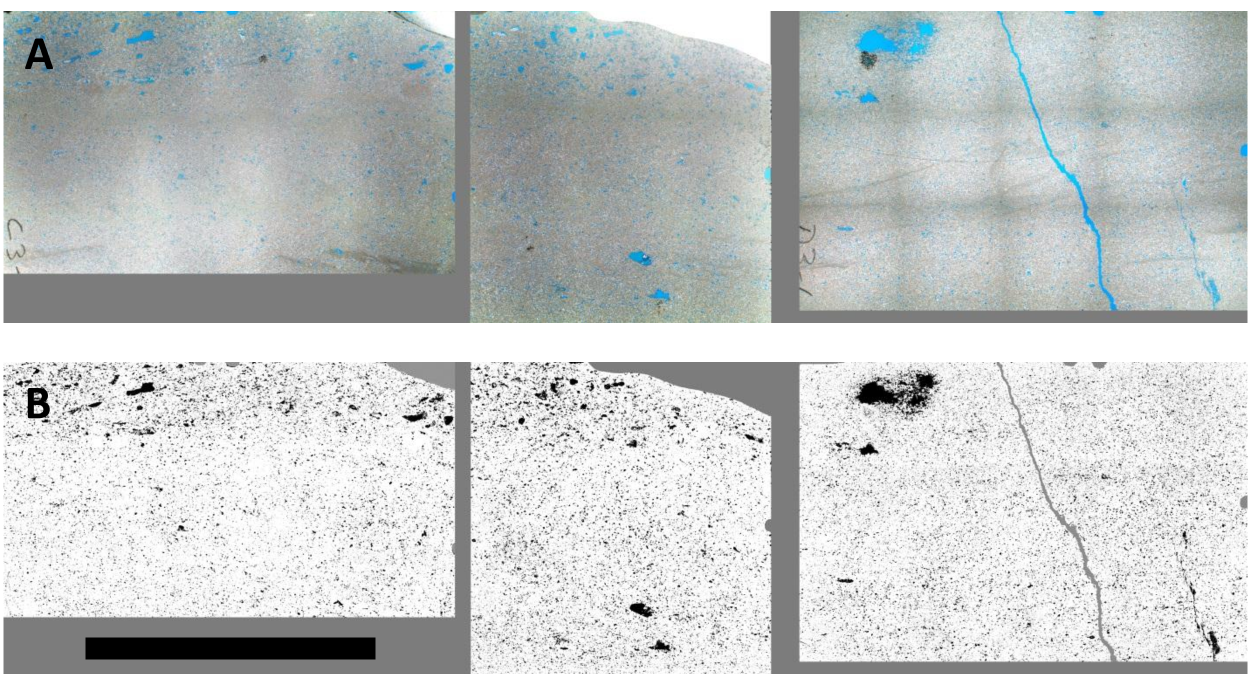

Figure 37. (A) Photomicropgraph showing the BCDE thin-section transect. Gray shadows in a grid pattern are artifacts created by the assembly (stitching) of the photomosaic. Dark gray space between images reflects rock cut away when sawing the samples for sectioning. (B) Same field of view as A, converted to grayscale. Dolomite is white, porosity is black and null data points are gray. Larger pores are molds which help define horizontal laminations. See Figure 17 for location on BCDE slab. Scale bar is 50mm.

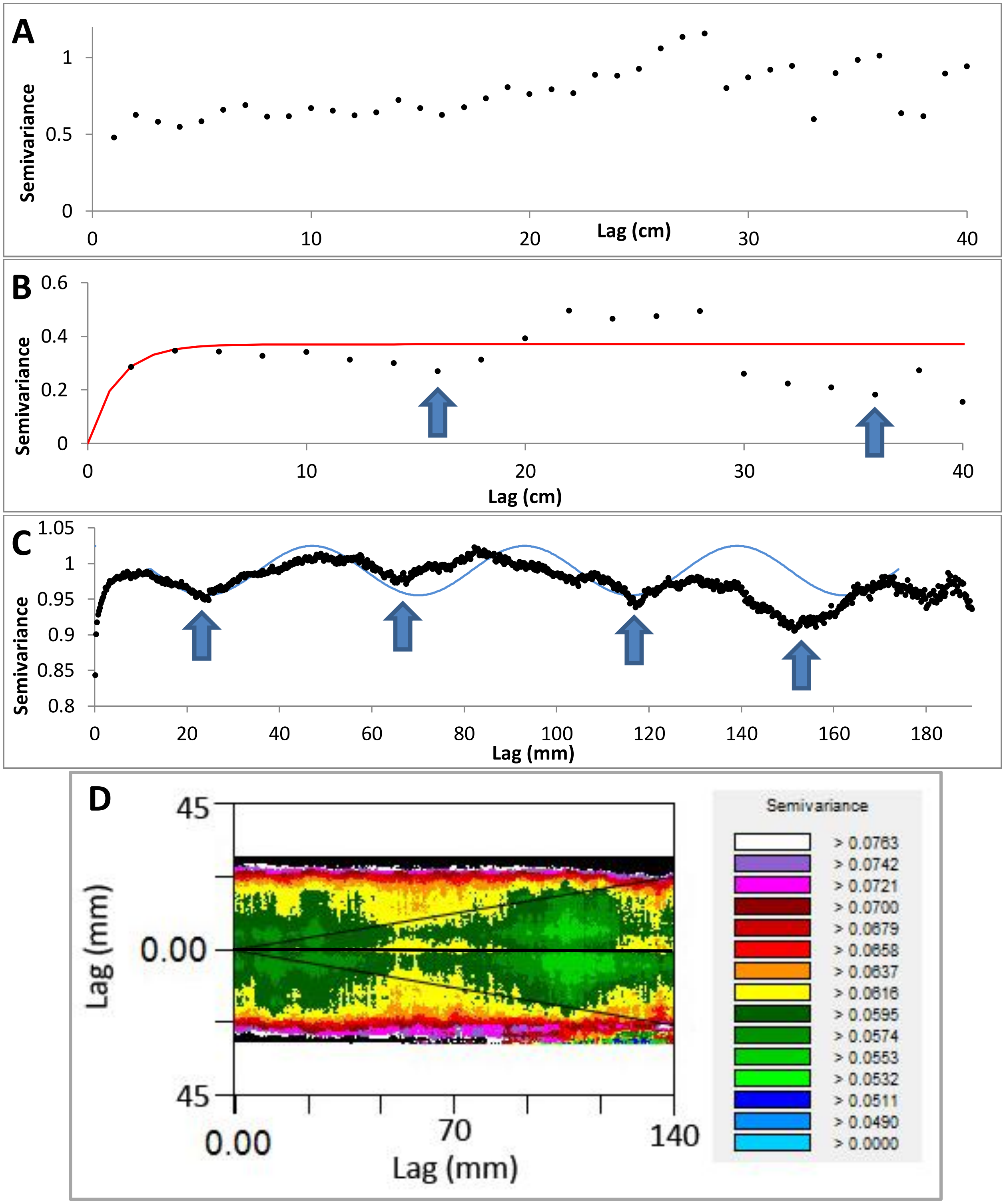

Figure 38. Experimental semivariograms of slab permeabililty (A), slab porosity (B), and thin-section porosity (C) for the BCDE slab. Exponential (red line) and hole-effect (blue line) models are fit to the data. Slab permeability exhibits just a long-range trend with no range, sill, or hole-effects. Slab porosity has a range of 4 cm and hole-effects with a wavelength of 20 cm. Thin-section porosity has a range of 4 mm and hole-effects with a wavelength of 46 mm. (D) Semivariance map for the thin-section transect showing that the anisotropic semivariogram (horizontal black line) is representative of all subhorizontal transects (black lines at ±10° from horizontal).

respectively. The upper half of the slab is cross-bedded and has lower porosity and permeability values than the lower half of the slab, which is horizontally laminated (Figure 39).

The KL thin-section transect (Figure 40) was cut from the cross-bedded portion of the slab (Figure 17) and is comprised of a grid of 240,843 points. There are 40,657 porosity points, 194,628 dolomite points, and 5,558 null data points. This gives a porosity value of 17.3% for the thin-section transect. The average slab porosity from the same area is 19.4%.

Experimental semivariograms were created for the KL slab's permeability, porosity, and the thin-section porosity. The KL experimental permeability semivariogram (Figure 41A) has a modeled nugget that accounts for 10% of the total semivariance. The correlation range is 13 cm and there are no hole-effects. The experimental semivariogram of KL porosity (Figure 41B) is a trend with no resolvable correlation range or sill, indicating the horizontal length of the slab (32 cm) was too short. Ten percent of the total semivariance occurs at the nugget, the balance is in the trend. The experimental semivariogram for the KL thin-section porosity (Figure 41C) has a modeled nugget of 0, the correlation range is 2 mm and there is a single hole-effect at a lag of 60 mm. A hole-effect model suggests that there may be long range pattern with a wavelength of 180 mm and an amplitude of 3.5% of the total semivariance, however the transect is not long enough to capture a second hole so the presence of a cyclic hole-effect cannot be concluded with certainty. The semivariance map (Figure 41D) shows that semivariance in positive subhorizontal direction (i.e., to +10°) is similar to the anisotropic semivariogram. However, semivariance in the negative subhorizontal directions (i.e., to -10°) has lower semivariance overall, thus the anisotropic semivariogram is not representative of all low-angle lateral transects. This is likely related to cross-bedding, as annotated on Figures 17 and 40B. The horizontal and positive angle semivariograms would cross laminations while the slightly negative angle semivariograms would be parallel to subparallel to cross-beddings, thus having lower semivariance overall, and likely no hole-effects as seen in Figure 41D.

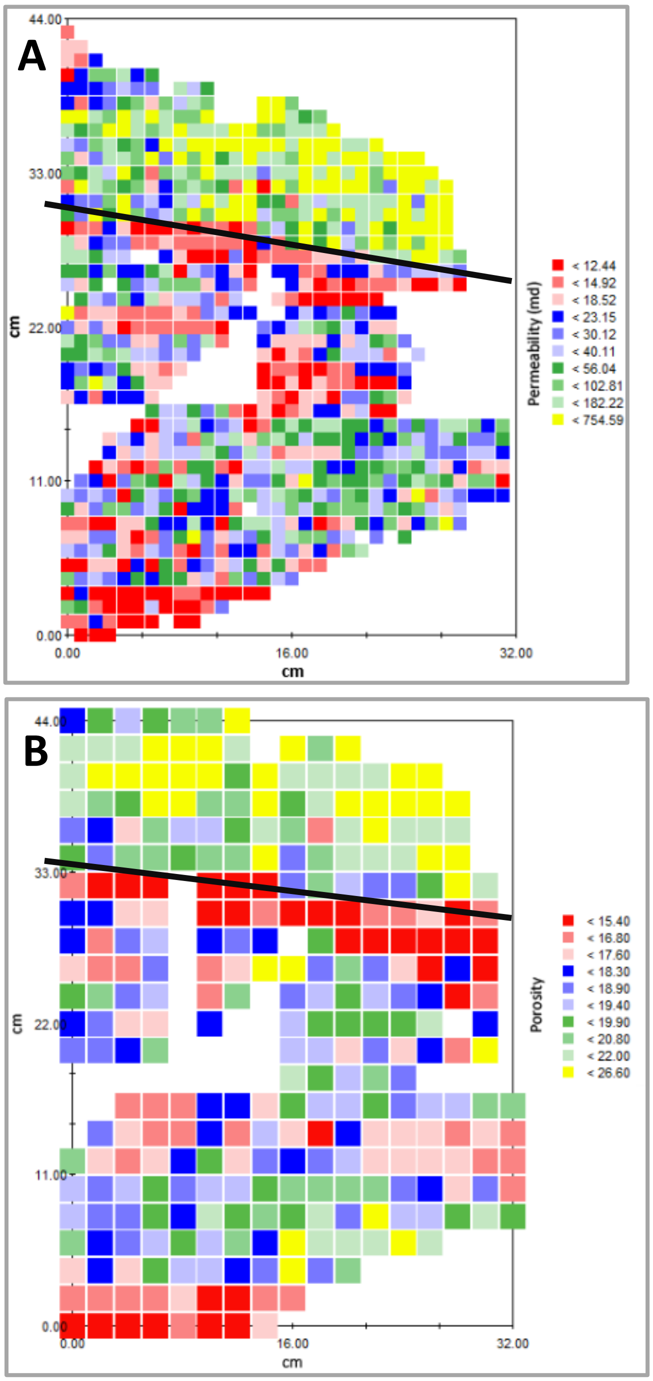

Figure 39. Pixel plots showing the distribution of (A) permeability and (B) porosity on the KL slab. Above the inclined black line, the slab is cross-bedded and generally of higher porosity and permeability; below the line the slab is horizontally laminated and generally has lower porosity and permeability. This spatial pattern may explain variance trends in the semivariance map (Figure 41D).

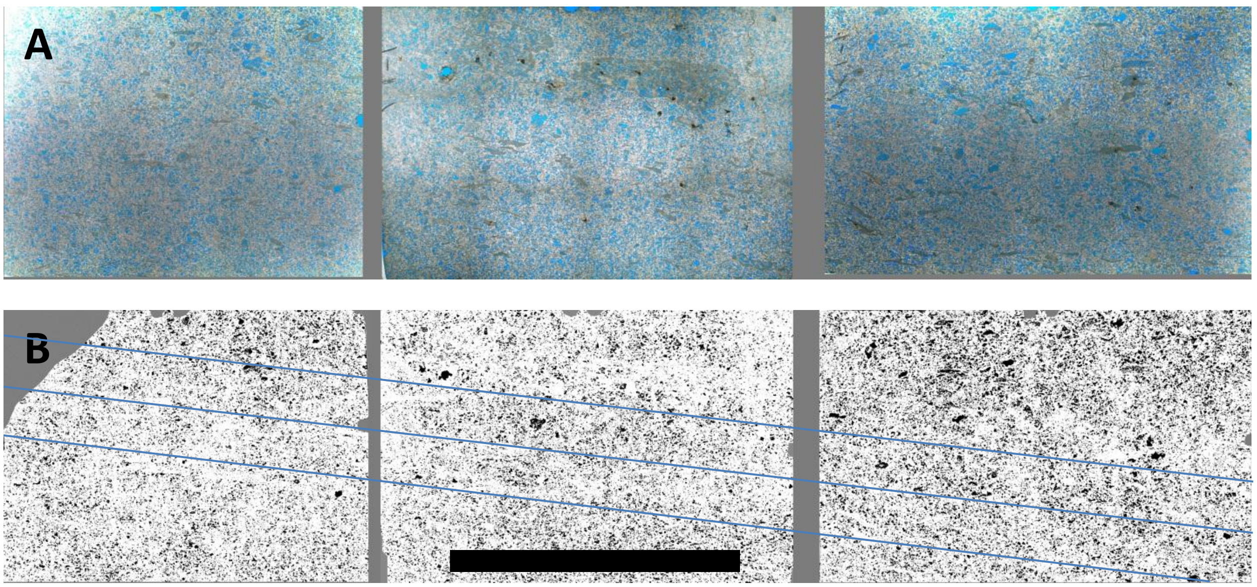

Figure 40. (A) Photomicropgraph showing the KL thin-section transect. Gray shadows in a grid pattern are artifacts created by the assembly (stitching) of the photomosaic. Dark gray space between images reflects rock cut away when sawing the samples for sectioning. (B) Same field of view as A, converted to grayscale. Dolomite is white, porosity is black and null data points are gray. Skeletal molds define cross-laminations (blue lines). See Figure 17 for location on KL slab. Scale bar is 50mm.

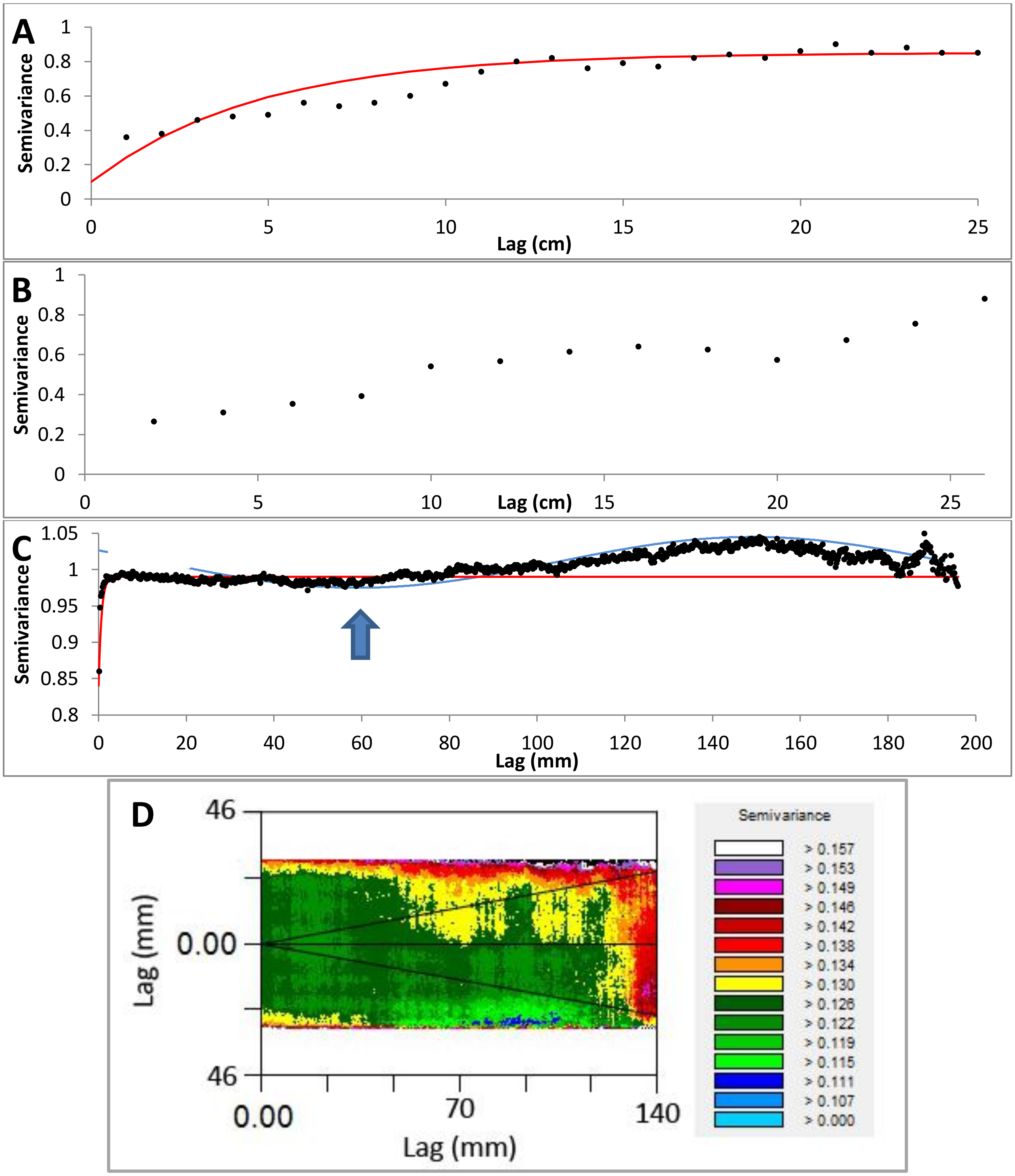

Figure 41. Experimental semivariograms of slab permeability (A), slab porosity (B), and thin-section porosity (C) for the KL slab. Exponential (red line) and hole-effect (blue line) models are fit to the data. Slab permeability has a range of 13 cm and no hole-effects. Slab porosity exhibits a long-range trend with no range, sill, or hole-effects. Thin-section porosity has a range of 2 mm and a modeled hole-effect with a 180 mm wavelength. (D) Semivariance map for the thin-section transect showing that the anisotropic semivariogram (horizontal black line) is representative of subhorizontal transects at positive angles, but not representative of transects at negative angles. This is likely due to cross lamination shown in Figures 40.

WXYZ Observations

The WXYZ slab was analyzed for permeability and porosity along a diagonal 7° from horizontal that parallels cross bedding. This was done so variography analysis was not biased by transecting cross laminations. Permeability was analyzed on a grid of 54 cm by 17 cm and contained 527 data points and 391 null points (Figure 17). The mean, median, minimum, and maximum horizontal permeabilities are 59.3, 25.2, 0.60 and 790 mD respectively. The diagonal porosity grid was 30 by 6 cubes, which yields a possible 180 data points of which 149 were measureable. The mean, median, minimum, and maximum diagonal porosities are 18.9, 18.5, 10.0, and 24.6% respectively. Cross laminations, which roughly parallel the horizontal grid are expressed as horizontal bands of alternating higher and lower permeability (Figure 42A). The coarse gridding of the porosity data, higher porosities are only evident in the laminations in the lower half of the slab (Figure 42B).

The WXYZ thin-section transect (Figures 17 and 43) is comprised of a grid of 166,618 points. There are 31,254 porosity points, 133,043 dolomite points, and 2,321 null data points. This gives a porosity value of 19.0% for the thin-section transect, which is in close agreement to the average slab porosity for the same area of 20.1%.

Experimental semivariograms were created for the diagonal WXYZ slab's permeability, porosity, and thin-section porosity. The experimental permeability semivariogram (Figure 44A) has a nugget that accounts for 10% of the total semivariance and the correlation range is 8 cm. Two hole-effects are present with a modeled wavelength of 29 cm and an amplitude equivalent to 30% of the total semivariance. The porosity experimental semivariogram (Figure 44B) has 10% of the total semivariance at the modeled nugget, the correlation range is 20 cm, and there is a modeled hole-effect with a wavelength of 20 cm and an amplitude equivalent to 40% of the total semivariance. The experimental semivariogram for thin-section porosity (Figure 44C) has a modeled nugget of 0, a correlation range of 2.5 mm, and no hole-effects. The semivariance map (Figure 44D) shows that the anisotropic semivariogram (Figure44C) is not representative of semivariance in positive or negative subhorizontal directions. That is, the horizontal semivariogram shows that variance is relatively constant after the sill has been reached, which is interpreted to mean that the horizontal semivariogram does parallel laminations. However, both the positive and negative subhorizontal directions exhibit decreasing and increasing, respectively, variance with increasing lag (i.e., long range trends) that are not present in the anisotropic semivariogram. These long range trends arise because subhorizontal directions cross laminations. Therefore, the optimum variogram is the horizontal (anisotropic semivariogram).

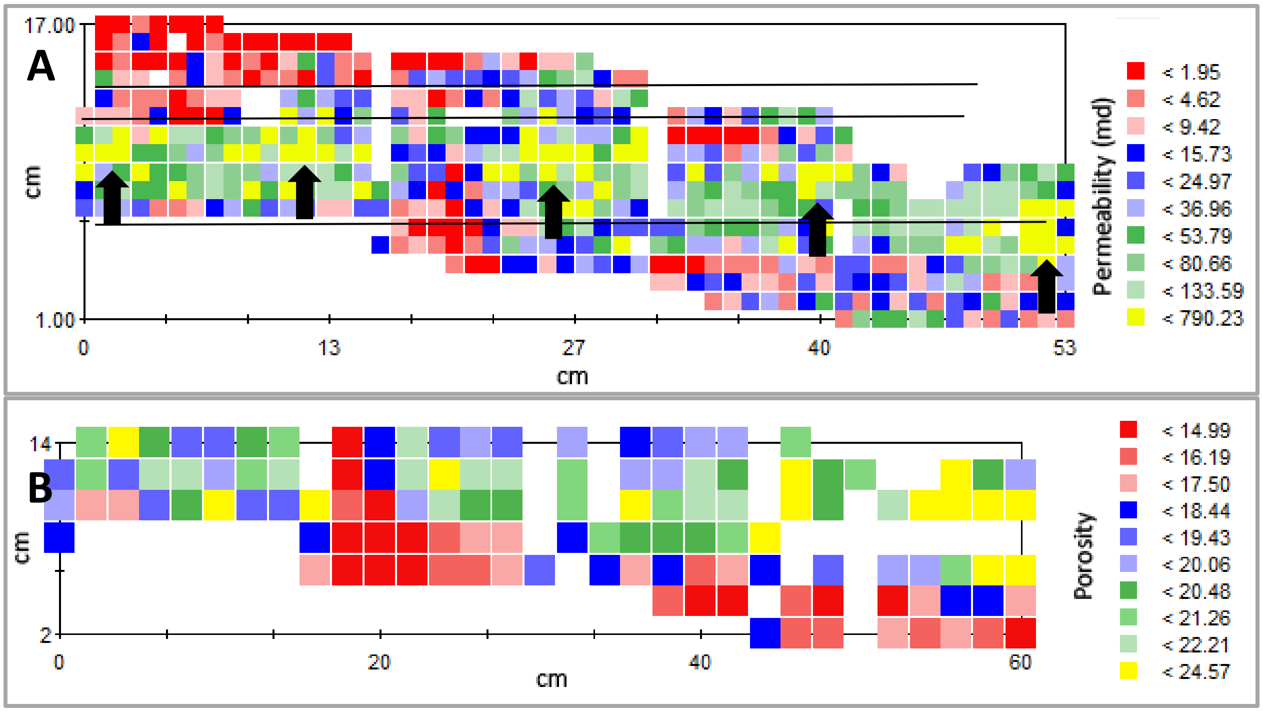

Figure 42. Pixel plots showing the distribution of (A) permeability and (B) porosity on the WXYZ slab. On the permeability plot, black lines represent laminations and black arrows denote a spatial pattern in the distribution of high permeability values.

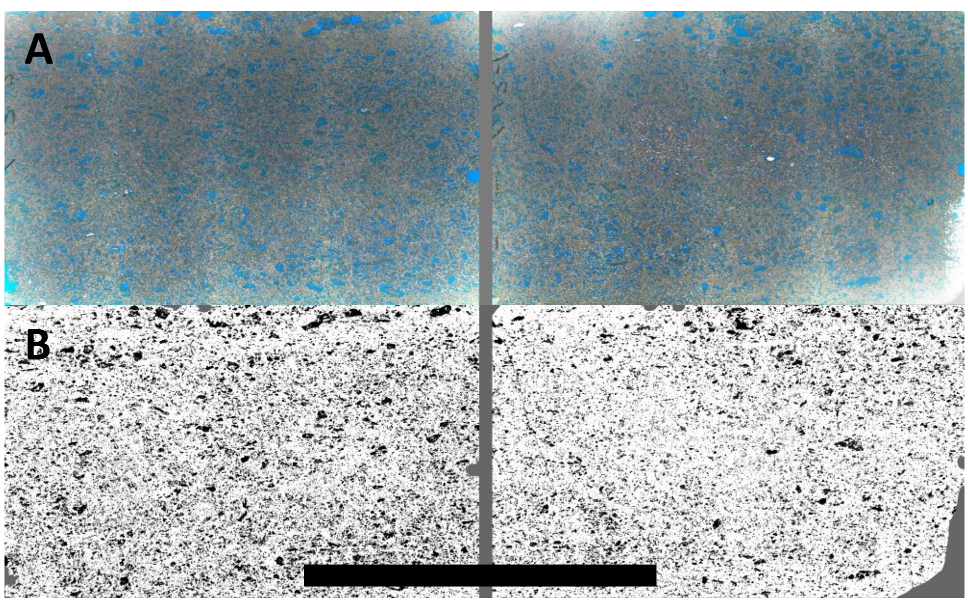

Figure 43. (A) Photomicropgraph showing the WXYZ thin-section transect. Large moldic pores and few skeletal ghost fabrics are visible. Gray shadows in a vertical pattern are artifacts created by the assembly (stitching) of the photomosaic. Dark gray space between images reflects rock cut away when sawing the samples for sectioning. (B) Same field of view as A, converted to grayscale. Dolomite is white, porosity is black and null data points are gray. See Figure 17 for location on WXYZ slab. Scale bar is 50mm.

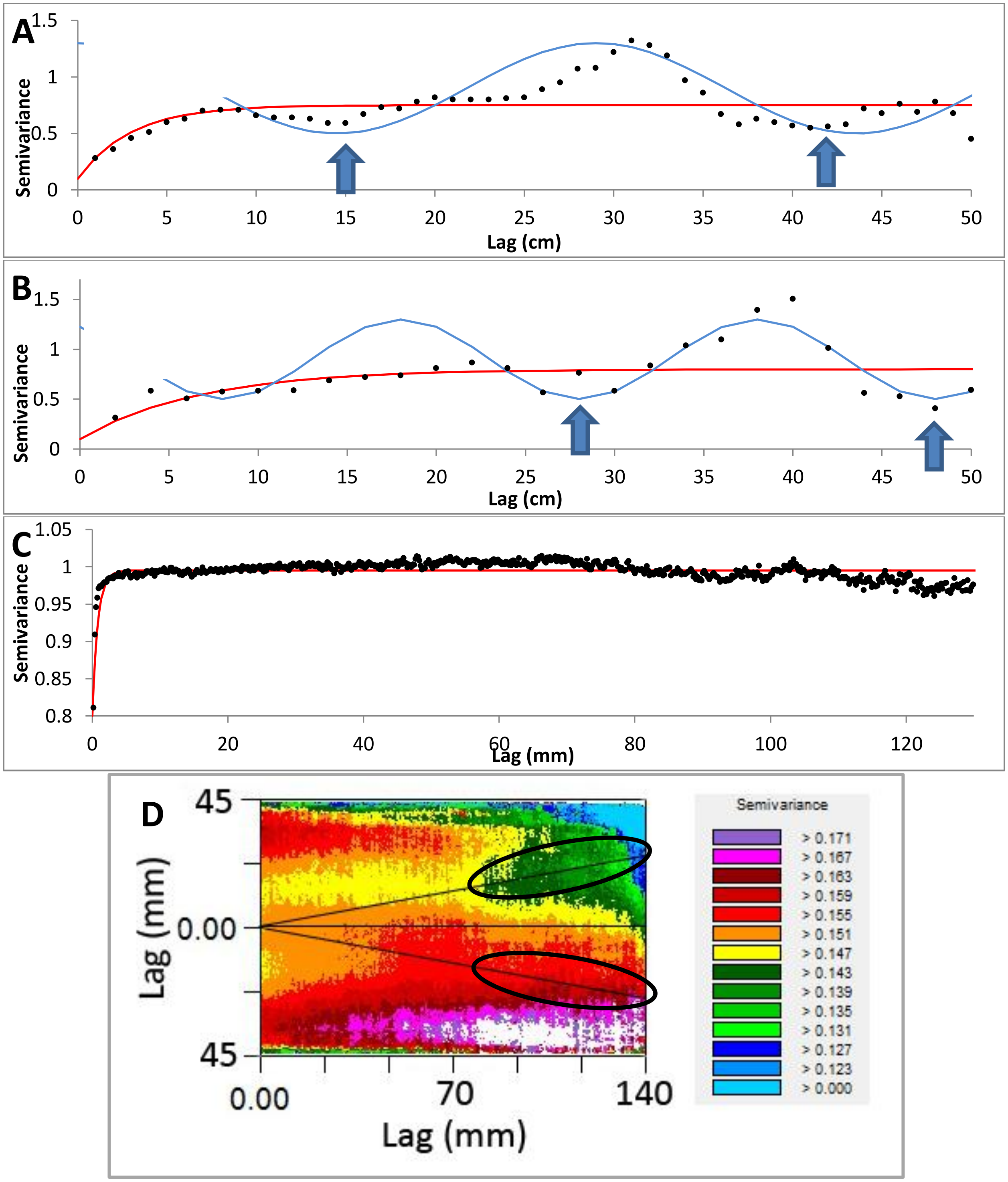

Figure 44. Experimental semivariograms of slab permeability (A), slab porosity (B), and thin-section porosity (C) for the WXYZ slab. Exponential (red line) and hole-effect (blue line) models are fit to the data. Slab permeability has a range of 8 cm and hole-effects with a wavelength of 29 cm. Slab porosity has a range of 20 cm and hole-effects with a wavelength of 20 cm. (C) Thin-section porosity has a range of 2.5 mm and no hole-effects. (D) Semivariance map for the thin-section transect which shows that subhorizontal transects (lines at ±10°) exhibit long-range trends in semivariance that are not captured by the horizontal transect. The +10° transect has a long range decreasing trend and the -10° transect has a long range increasing trend (black circles).

Sheep Observations

The Sheep slab was analyzed for permeability on a 76 cm by 8 cm grid and contained 556 data points and 52 null data points (Figure 17). The mean, median, minimum, and maximum permeability are 5.2, 2.0, 0.4 and 121 mD respectively. The Sheep slab's porosity grid is 40 cubes by 4 cubes which yields a possible 160 data points of which 140 were measured. The mean, median, minimum and maximum porosities are 16.9, 16.7, 12.1, and 23.2% respectively. Visually, the spatial distribution of permeability and porosity appears heterogenous and with no discernible patter (Figure 45), although one could argue for a mottled pattern of high and low permeability values reflective of the burrow mottling seen on the slab face (Figure 17).

The Sheep thin-section transection (Figures 17 and 46) is comprised of a grid of 316,889 points. There are 19,948 porosity points, 296,941 dolomite points, and 25,814 null points. This gives a porosity value of 6.3% for the thin-section transect. The average slab porosity for the same area is 16%. This large discrepancy is difficult to explain, but may be due in large part to intercrystalline porosity between very fine crystalline dolomite. These pores can be the size of an individual pixel and therefore may not be well resolved in the image. This would act to lower the thin-section porosity measurement while not effecting cube porosity.

Experimental semivariograms were created for the Sheep slab's permeability, porosity, and thin-section porosity. The permeability experimental semivariogram (Figure 47A) exhibits 50% of its total semivariance at the nugget. The correlation range is 4 cm and there are no hole- effects, although there is a long range decline in semivariance at lags greater than 40 cm. The porosity experimental semivariogram (Figure 47B) exhibits 30% of its total semivariance at the nugget, no correlation range, and no sill. Rather, there is a trend of increasing semivariance with increasing lag and three hole-effects superimposed on that trend. Those hole-effects have a modeled wavelength of 22 cm and an amplitude equivalent to 20% of the total semivariance. The experimental semivariogram for thin-section porosity (Figure 47C) exhibits a modeled nugget of 0 and a correlation range of 2 mm. A hole-effect model fit to the experimental data between lags of 25 and 175 mm suggests a possible hole-effect with a wavelength of 220 mm and an amplitude equivalent to 5% of the total semivariance. However there is no second hole so the presence of a cyclic hole-effect cannot be concluded with certainty. The semivariance map (Figure 47D) shows that semivariance in subhorizontal directions are generally similar to the anisotropic semivariogram. Subtle difference occur at long lags. For example, at positive angles a very high variance area occurs at a horizontal lag of 165 mm. At negative angles, there is a very low variance area at a lag of about 250 mm. These are subtle variations that would not differ greatly from the anisotropic semivariogram, but may change the amplitude of observed hole-effects. Overall, the anisotropic semivariogram is concluded to be a good representative of all subhorizontal transects.

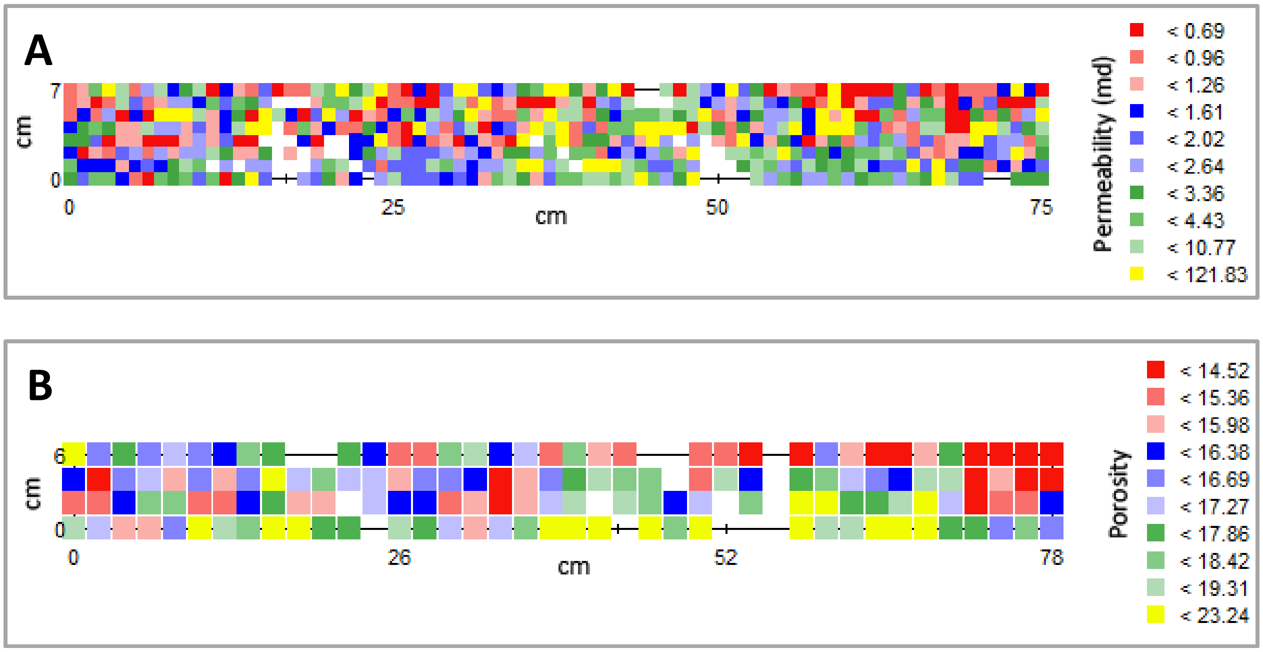

Figure 45. Pixel plots showing the distribution of (A) permeability and (B) porosity on the Sheep slab. No spatial patterns are readily apparent from these plots.

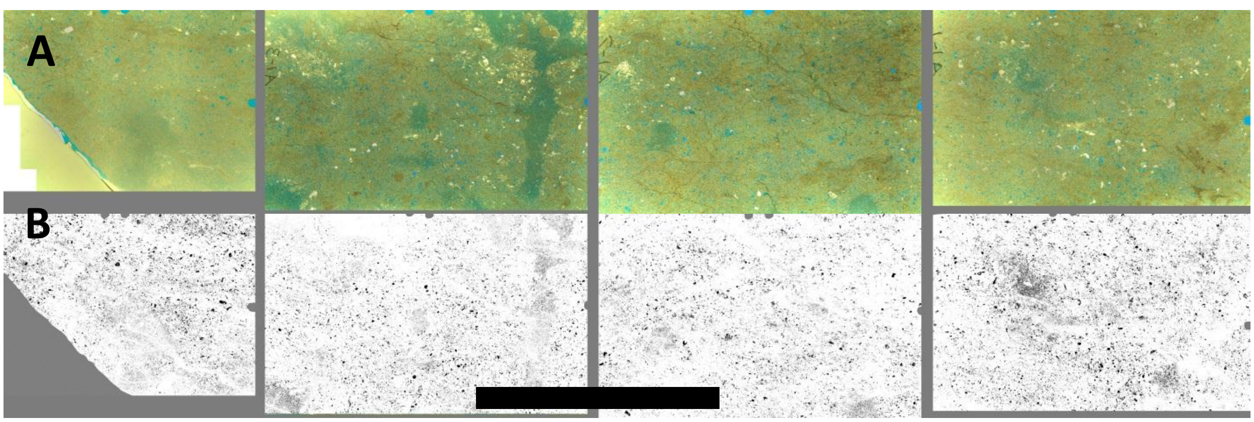

Figure 46. (A) Photomicropgraph showing the Sheep thin-section transect. Larger pores are grain molds, white areas are calcite cement and blue mottling is porosity associated with bioturbation. Dark gray space between images reflects rock cut away when sawing the samples for sectioning. (B) Same field of view as A, converted to grayscale. Dolomite and calcite are white, porosity is black and null data points are gray. See Figure 17 for location on Sheep slab. Scale bar is 50mm.

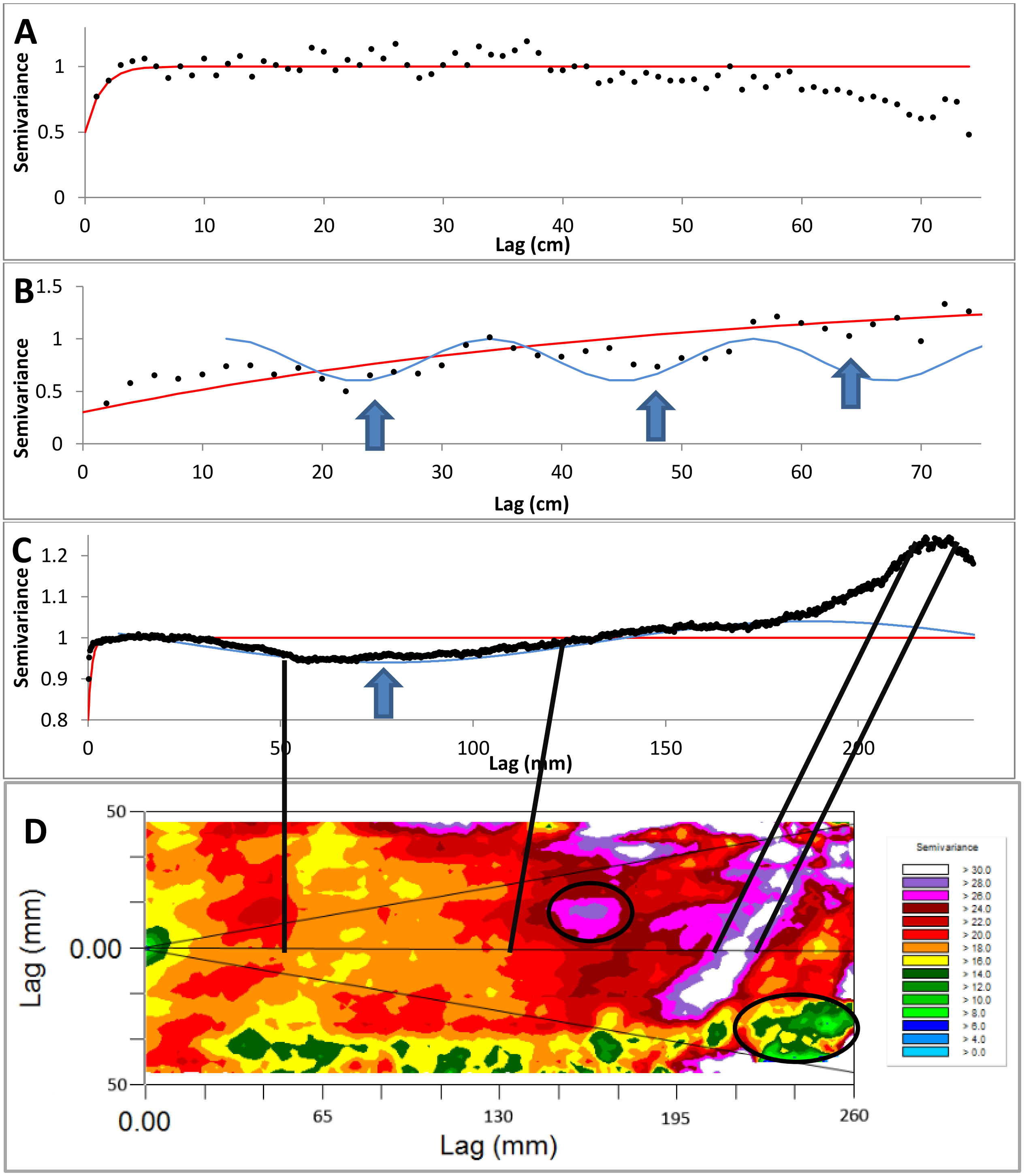

Figure 47. Experimental semivariograms of slab permeability (A), slab porosity (B), and thin-section porosity (C) for the Sheep slab. Exponential (red line) and hole-effect (blue line) models are fit to the data. Slab permeability has a range of 4 cm and no hole-effects. Slab porosity shows a long-range trend with a superimposed hole-effect at a wavelength of 22 cm. Thin-section porosity has a range of 2 mm and a potential hole-effect of 220 mm wavelength. (D) Semivariance map for the thin-section transect showing that the anisotropic semivariogram is representative of all subhorizontal transects. Subtle differences exist between thepositive and negative angle transects as discussed in the text and denoted by black circles. Black lines link the anisotropic semivariogram in C to the horizontal transect on the map.

Cairn Observations

The Cairn slab was analyzed for permeability on a 109 cm by 8 cm grid and contained 751 data points and 121 null data points (Figure 17). The mean, median, minimum, and maximum permeability are 0.5, 0.2, 0.1 and 91.1 mD respectively. The Cairn slab's porosity grid is 55 cubes by 6 cubes, which yielded 238 measured data points and 92 null data points. The mean, median, minimum, and maximum porosities are 7.1, 5.9, 0.7, and 43.2% respectively. The permeability and porosity maps of the slab (Figure 48) depict regularly spaced pods of low permeability and porosity in the lower half of the slab.

The Cairn thin-section transect (Figures 17 and 49) is comprised of a grid of 239,566 points. There are 2,929 porosity points, 235,684 dolomite points, and 953 null data points. This gives a thin-section porosity of 1.2%, which compares poorly to the average slab porosity from the same area of 7%. Again, this discrepancy is likely a function of the slab porosity being a measure of pore volume in three dimensions. A moldic pore in the z-direction would be captured in the cube, but not in the thin-section. In addition, some of the small intercrystalline pores in the thin section might have been smaller than the resolution of a single pixel.

Experimental semivariograms were created for the Cairn slab's permeability, porosity, and thin-section porosity. The experimental semivariogram of permeability (Figure 50A) exhibits 30% of its total semivariance at the modeled nugget. The correlation range is 10 cm and there are three hole-effects at lags of 30, 60, and 90 cm, giving a wavelength of 30 cm and an amplitude equivalent to 25% of the total semivariance. The experimental semivariogram of porosity (Figure 50B) exhibits 10% of the total semivariance at the modeled nugget, a correlation range of 10 cm, and no hole-effects of a consistent wavelength. The experimental semivariogram for thin-section porosity (Figure 50C) exhibits 30% of its total semivariance at the modeled nugget and a correlation range of 5 mm. There are five hole-effects with a wavelength of 28 mm and an amplitude equivalent to 7% of total semivariance. The semivariance map (Figure 50D) confirms that variance along subhorizontal transects is similar to the anisotropic semivariogram with many small hole-effects. Subhorizontal transects at positive angles have higher semivariance overall and subhorizontal transects on negative angles cross the largest amplitude hole-effects. All angles exhibit their lowest semivariance beyond the range at long lags, which may indicate a long-range trend.

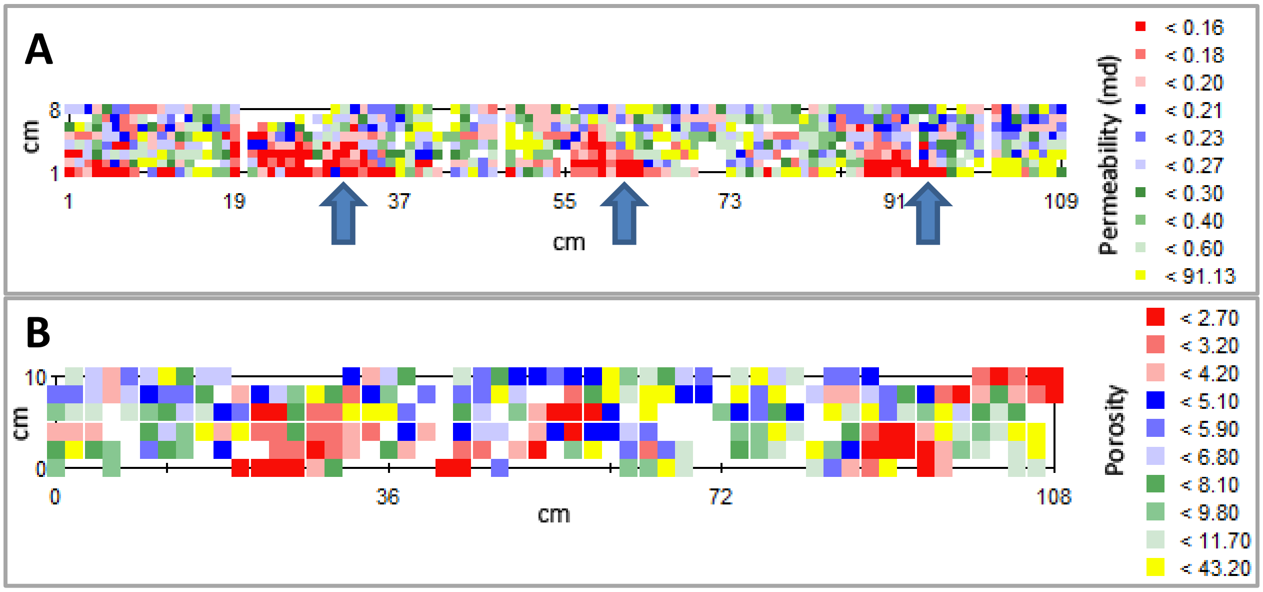

Figure 48. Pixel plots showing the distribution of (A) permeability and (B) porosity on the Cairn slab. Both plots exhibit three low value areas (blue arrows in A) that likely correspond to hole-effects seen on Figure 50A.

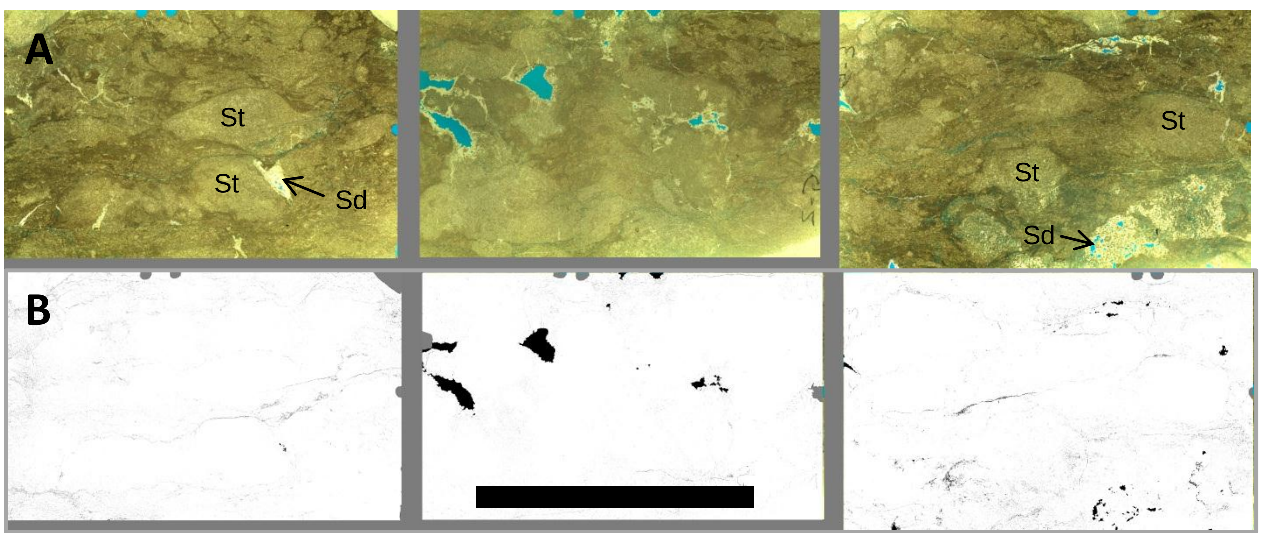

Figure 49. (A) Photomicropgraph showing the Cairn thin-section transect. Large pores are stromotoporoid molds. Other molds have been occluded by saddle dolomites (Sd). Some stromotoporoids have not been leached (St). Dark gray space between images reflects rock cut away when sawing samples for sectioning. (B) Same field of view as A, converted to grayscale. Dolomite is white, porosity is black and null data points are gray. See Figure 17 for location on Cairn slab. Scale bar is 50 mm.

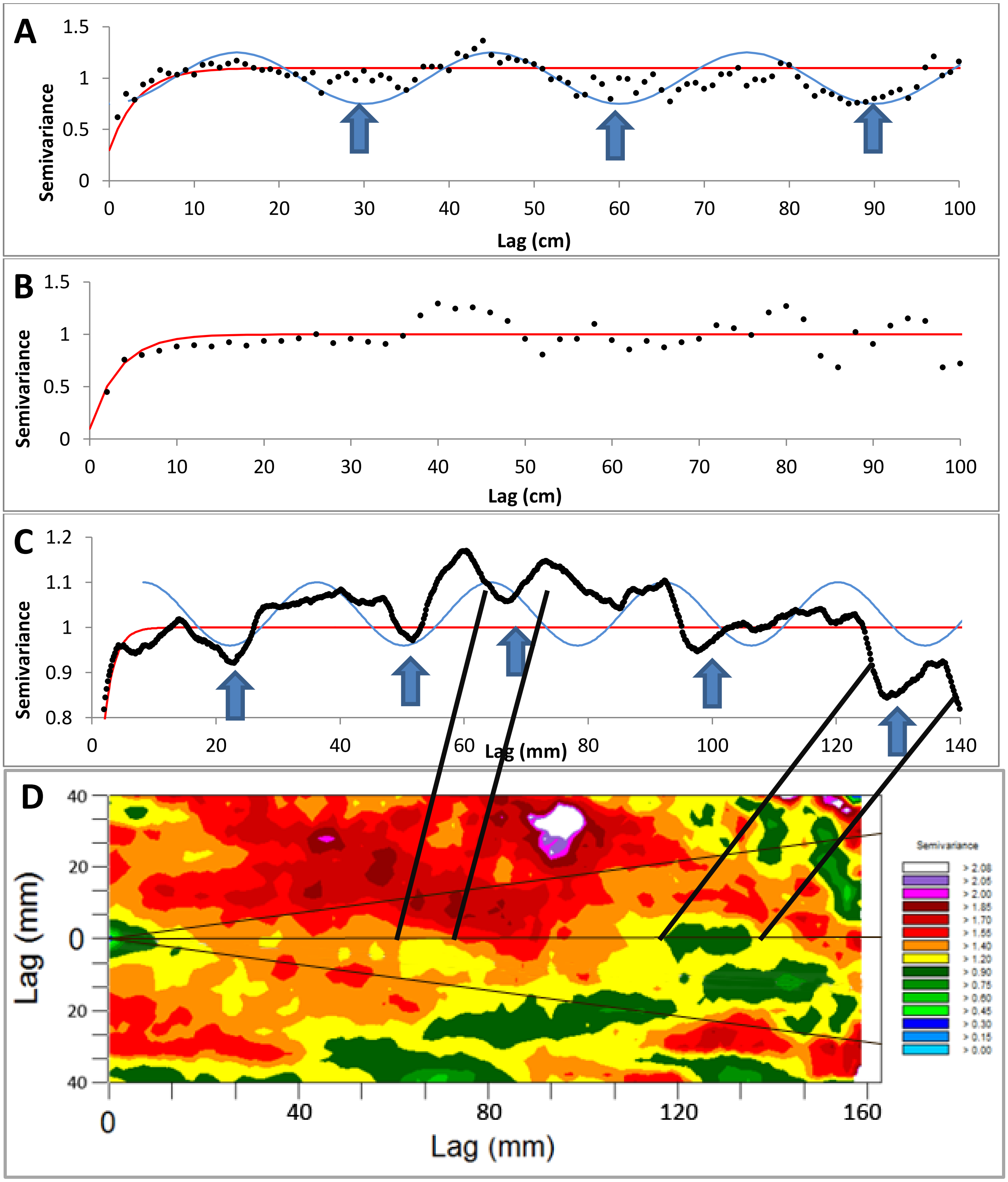

Figure 50. Experimental semivariograms of slab permeability (A), slab porosity (B), and thin-section porosity (C) for the Cairn slab. Exponential (red line) and hole-effect (blue line) models have been fit to the data. Slab permeability has a range of 10 cm and hole-effects at a wavelength of 30 cm. Slab porosity has a range of 10 cm and no hole-effect. Thin-section porosity has a range of 5 mm and hole-effects at a wavelength of 28 mm. (D) Semivariance map for the thin-section transect showing that the anisotropic semivariogram is similar to subhorizontal semivariograms. Semivariance is higher at positive angles and all angles exhibit low semivariance at long lags. Black lines link the anisotropic semivariogram in C to the horizontal transect on the map.

Outcrop Photomosaic Data

Cairn Observations

Three outcrop photomosaics were analyzed for the Cairn Formation, herein called (1) outcrop D, (2) outcrop E, and (3) outcrop H. The outcrop D photomosaic (Figure 51A) is 8 meters wide and 4 meters tall. Sample spacing on the photomosaic was 2.5 cm, which yielded a grid of 53,584 data points, of which 3,733 were vuggy pores, giving a vug porosity of 7.0%. The experimental indicator semivariogram of vuggy pores (Figure 51C) exhibits 32% of its total semivariance at the modeled nugget. The correlation range is 20 cm and there is a long range structure that may be interpreted as a hole-effect with a wavelength of 320 cm and an amplitude equivalent to 4% of total semivariance. This hole-effect appears to dampen beyond a lag of 550 cm.

The outcrop E photomosaic (Figure 52A) was collected perpendicular to the outcrop, but it images a slight dip to the bedding. Only the main bed in the outcrop was analyzed. It is 20 meters wide and 3 meters tall. Sample spacing on the photomosaic was 2.5 cm, which yielded a grid of 95,280 data points, of which 10,578 were vuggy pores and 29,573 were null points. This gives a vuggy porosity of 16.1%. The experimental indicator semivariogram of vuggy pores (Figure 52C) exhibits 30% of its total semivariance at the modeled nugget. The correlation range is 10 cm and there are no hole-effects. However, there is a long range increasing trend in semivariance beyond a lag of 800 cm.

The outcrop H photomosaic (Figure 53A) is a close-up view of three beds of vuggy dolomite. The rock face imaged is 5.55 m wide and 2.76 cm tall. A sample spacing of 3 cm yielded a grid of 17,021 data points, of which 1,085 were vuggy pores (6.4% vuggy porosity).

The experimental indicator semivariogram of vuggy pores (Figure 53C) exhibits 40% of its total variance at the modeled nugget. The correlation range is 20 cm and there are no hole-effects.

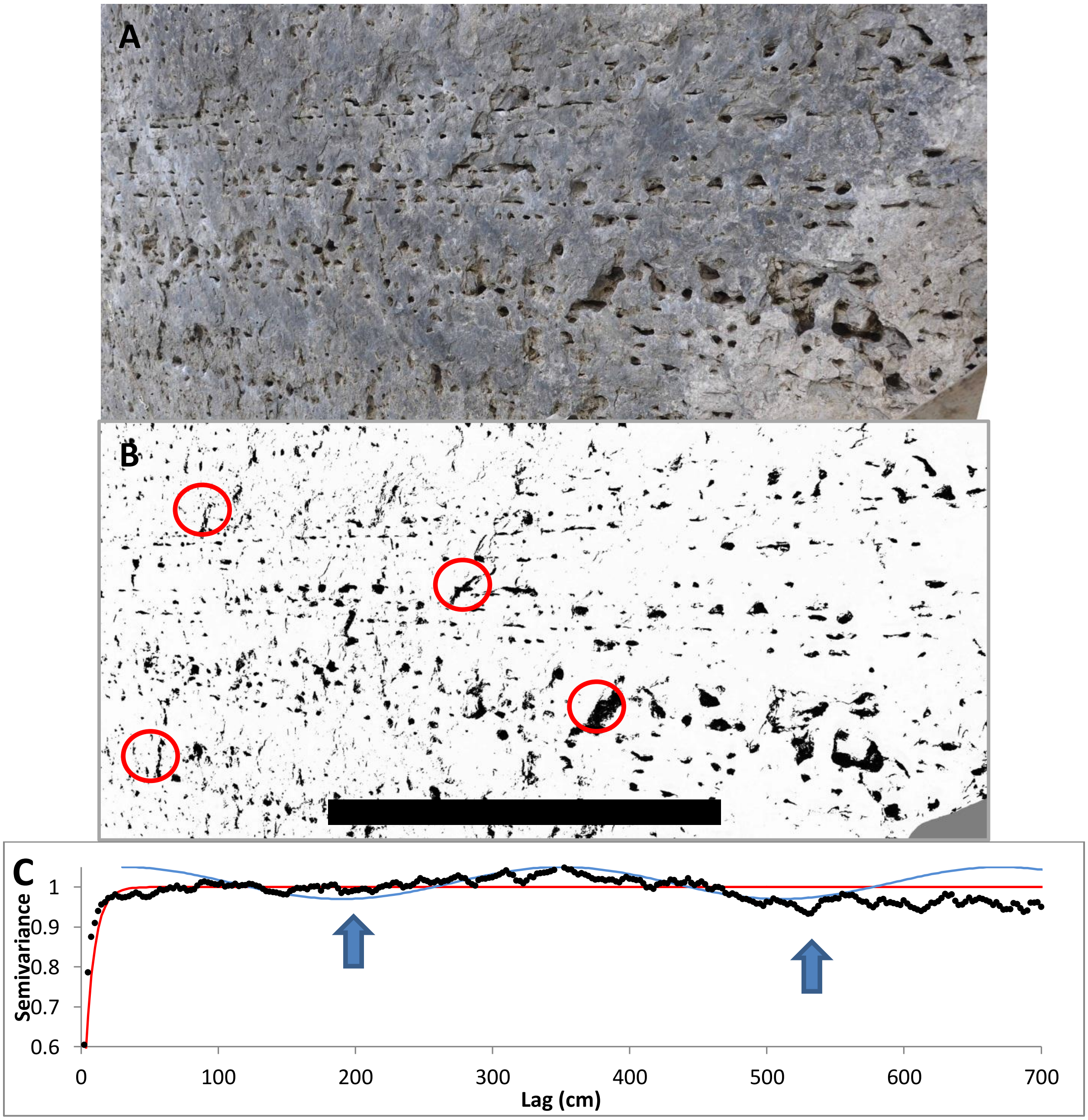

Figure 51. Outcrop photomosaic and corresponding variogram for "outcrop D" of the Cairn Formation. (A) Color and (B) grayscale images of the outcrop face where vuggy porosity is black and matrix dolomite is white. Red circles represent areas where surface irregularities create noise in the semivariogram. Scale bar is 3.5 meters. (C) Experimental semivariogram of vuggy porosity with exponential (red) and hole-effect (blue) models fit to the data. Correlation range is 20 cm and modeled hole-effect wavelength is 320 cm.

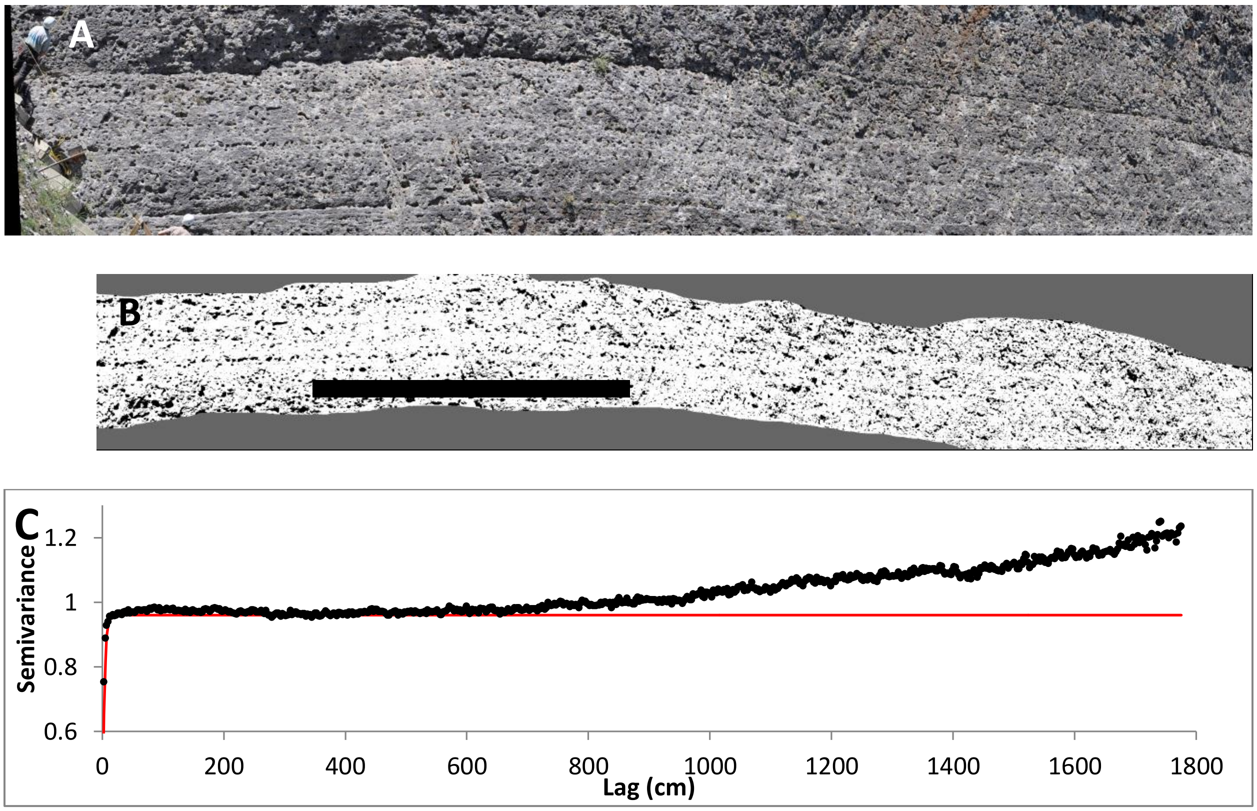

Figure 52. Outcrop photomosaic and corresponding variogram for "outcrop E" of the Cairn Formation. (A) Color and (B) grayscale images of the outcrop face where vuggy porosity is black and matrix dolomite is white. Bedding dip and foreshortening towards the right edge of the photomosaic are sources of noise in the semivariogram. Scale bar is 5 meters. (C) Experimental semivariogram of vuggy porosity with an exponential model (red) fit to the data. Correlation range is 10 cm and there is a long-range increasing trend in semivariance, but no hole-effects are present.

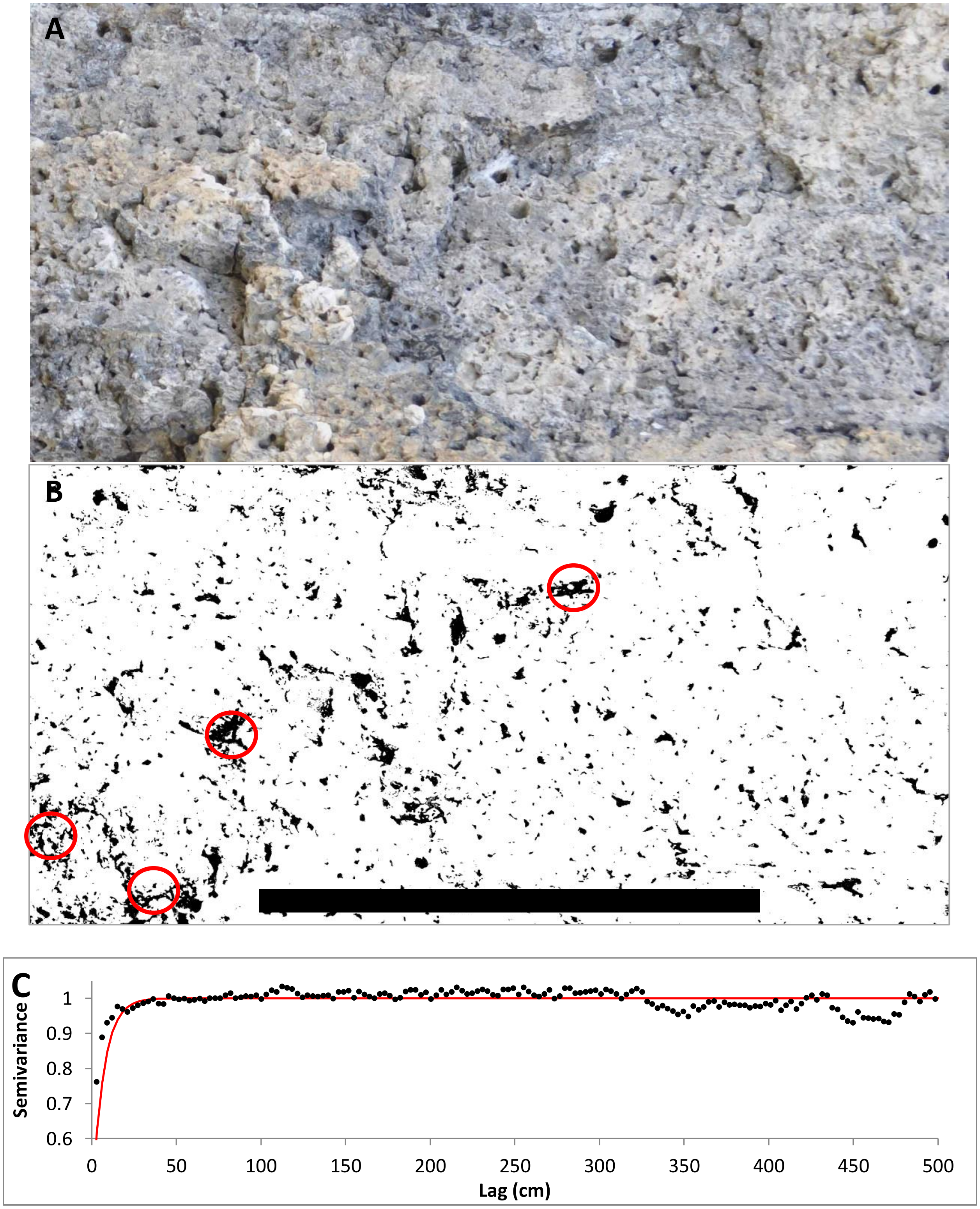

Figure 53. Outcrop photomosaic and corresponding variogram for "outcrop H" of the Cairn Formation. (A) Color and (B) grayscale images of the outcrop face where vuggy porosity is black and matrix dolomite is white. Red circles represent areas where surface irregularities create noise in the semivariogram. Scale bar is 3 meters. (C) Experimental semivariogram of vuggy porosity with exponential model (red) fit to the data. Correlation range is 20 cm.

Tansill Observations

Three outcrop photomosaics were analyzed across limestone-dolostone transitions in the Tansill Formation, and are herein called (1) downstream, (2) midstream, and (3) upstream. The downstream photomosaic (Figure 54A) depicts an outcrop that is 17.7 meters wide and 1.7 meters tall. It was sampled at a spacing of 4.5 cm, which yielded 15,010 data points, of which 5,416 were dolomite and 7,137 were limestone (43% dolomite). The experimental indicator semivariogram of dolomite (Figure 54C) exhibits 35% of its total semivariance at the modeled nugget. The correlation range is 230 cm and there is a hole-effect with a wavelength of 560 cm and an amplitude equivalent to 8% of the total semivariance. The semivariance map (Figure 54D) indicates that the anisotropic semivariogram is fairly representative of all subhorizontal semivariograms. However, the horizontal semivariogram has a longer correlation range as shown by the horizontally elongate low variance area at the origin (0,0). Also, the hole-effect present at a lag of 1000 cm on the anisotropic semivariogram is not present at similar lags on the subhorizontal transects.

The midstream photomosaic (Figures 34 and 55A) is 75 cm wide and 30 cm tall and was sampled at a spacing of 2 mm. This yielded a grid of 54,604 data points, of which 20,746 were dolomite and 33,858 were limestone (38% dolomite). The experimental indicator semivariogram of dolomite (Figure 55C) exhibits 35% of its total semivariance at the modeled nugget and a correlation range of 150 mm. There is one hole-effect at a lag of 450 mm that has an amplitude equivalent to 11% of the total semivariance, however the wavelength could not be modeled because no other holes occur. The semivariance map (Figure 55D) shows that the variogram shape is the same in all subhorizontal directions with a hole-effect at a lag of 450 mm. Subhorizontal transects at positive angles experience the highest amplitude hole-effect (green areas on map at a lag of 450 mm).

The upstream photomosaic (Figures 34 and 56A) is 140 cm wide and 60 tall and was sampled at a spacing of 2.8mm. This yielded a grid of 110,025 data points, of which 61,649 were dolomite and 40,440 were limestone (60% dolomite). The experimental indicator semivariogram of dolomite (Figure 56C) exhibits 20% of its total semivariance at the modeled nugget. The correlation range is 50 mm and there are no hole-effects. The semivariance map (Figure 56D) shows that the anisotropic semivariogram is representative of all subhorizontal transects. The minor difference revealed on the map is that semivariograms at negative angles reach higher overall levels of semivariance at long lags (red and yellow area on map between 0° and -10°).

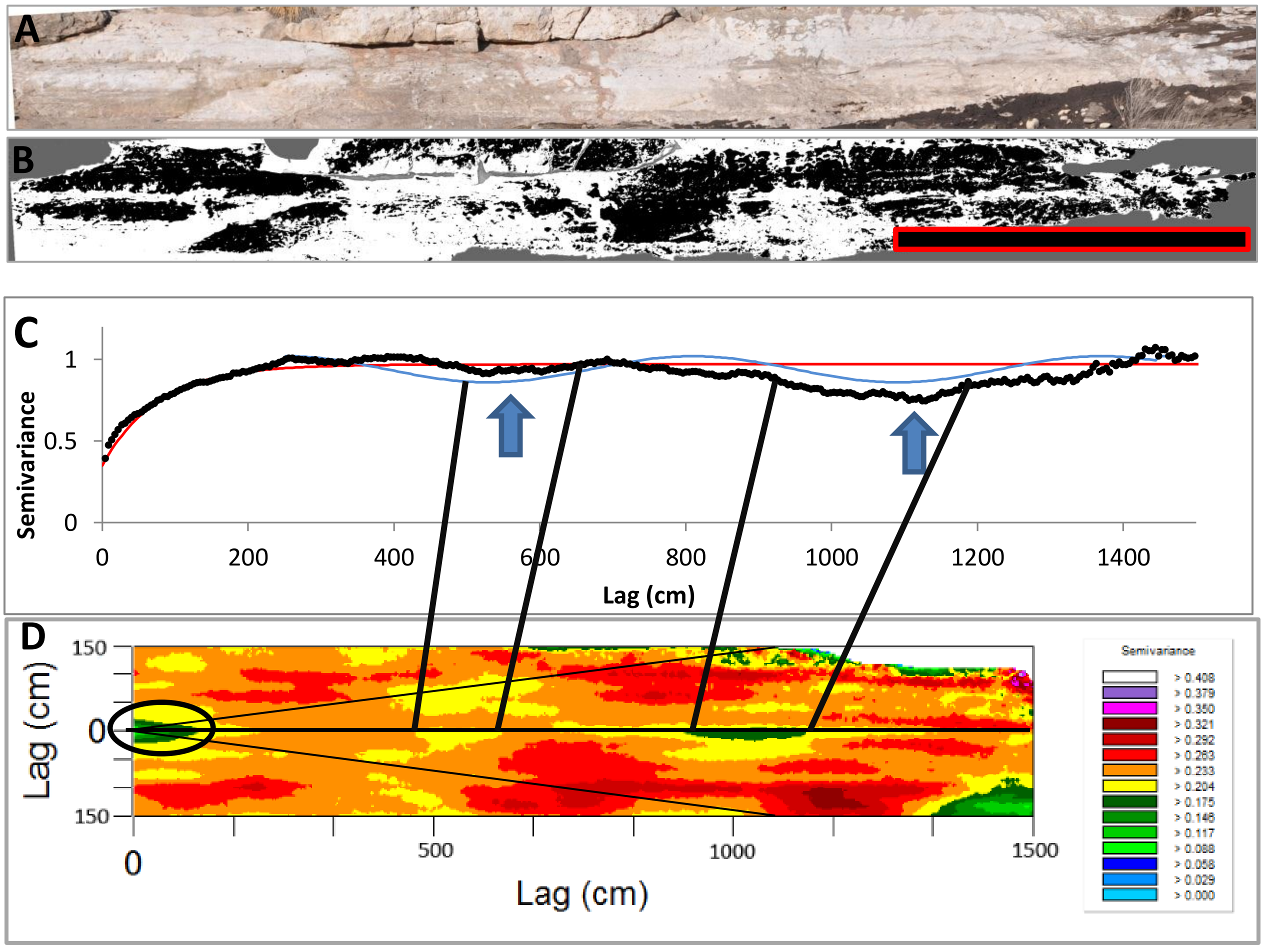

Figure 54. "Downstream" outcrop photomosaic and corresponding semivariogram in the Tansill Formation. (A) Color and (B) grayscale images of the outcrop where dolomite is converted to black and limestone to white. Scale bar is 5 meters. (C) Experimental semivariogram of lithology with exponential (red) and hole-effect (blue) models fit to the data. Correlation range is 230 cm and there are two hole-effects with a wavelength of 560 cm. (D) Semivariance map that shows that the anisotropic semivariogram (horizontal line) is representative of the distribution of semivariance in all other subhorizontal directions (±10°). In particular, all variograms would pass through multiple hole-effects, as indicated by the color mottling in the map. The correlation range is longest for horizontal transects as shown by the elongate green patch at the origin (circled in black).

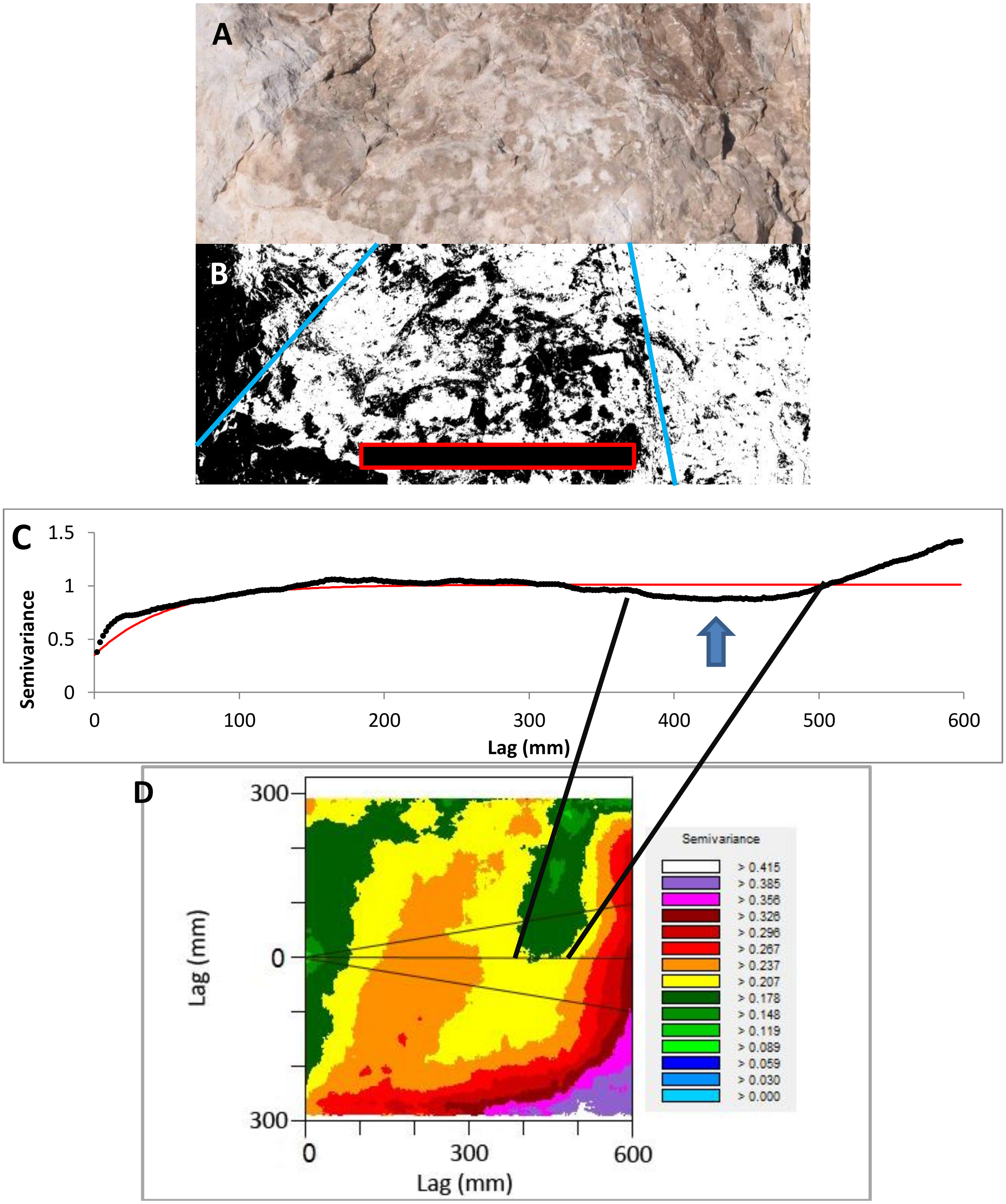

Figure 55. "Midstream" outcrop photomosaic and corresponding variogram in the Tansill Formation. (A) Color and (B) grayscale images with dolomite black, limestone white, and blue lines representing fractures traces. See Figure 34 for position of this midstream location relative to upstream photomosaic. Scale bar is 30 cm. (C) Experimental semivariogram of lithology with exponential model (red) fit to data. Correlation range is 150 mm and there is one hole-effect (blue arrow) at a lag of 450 mm. (D) Semivariance map showing that semivariogram attributes are similar in all subhorizontal directions. The hole-effect amplitude is greatest for positive angle directions (green area at a lag of 450 mm).

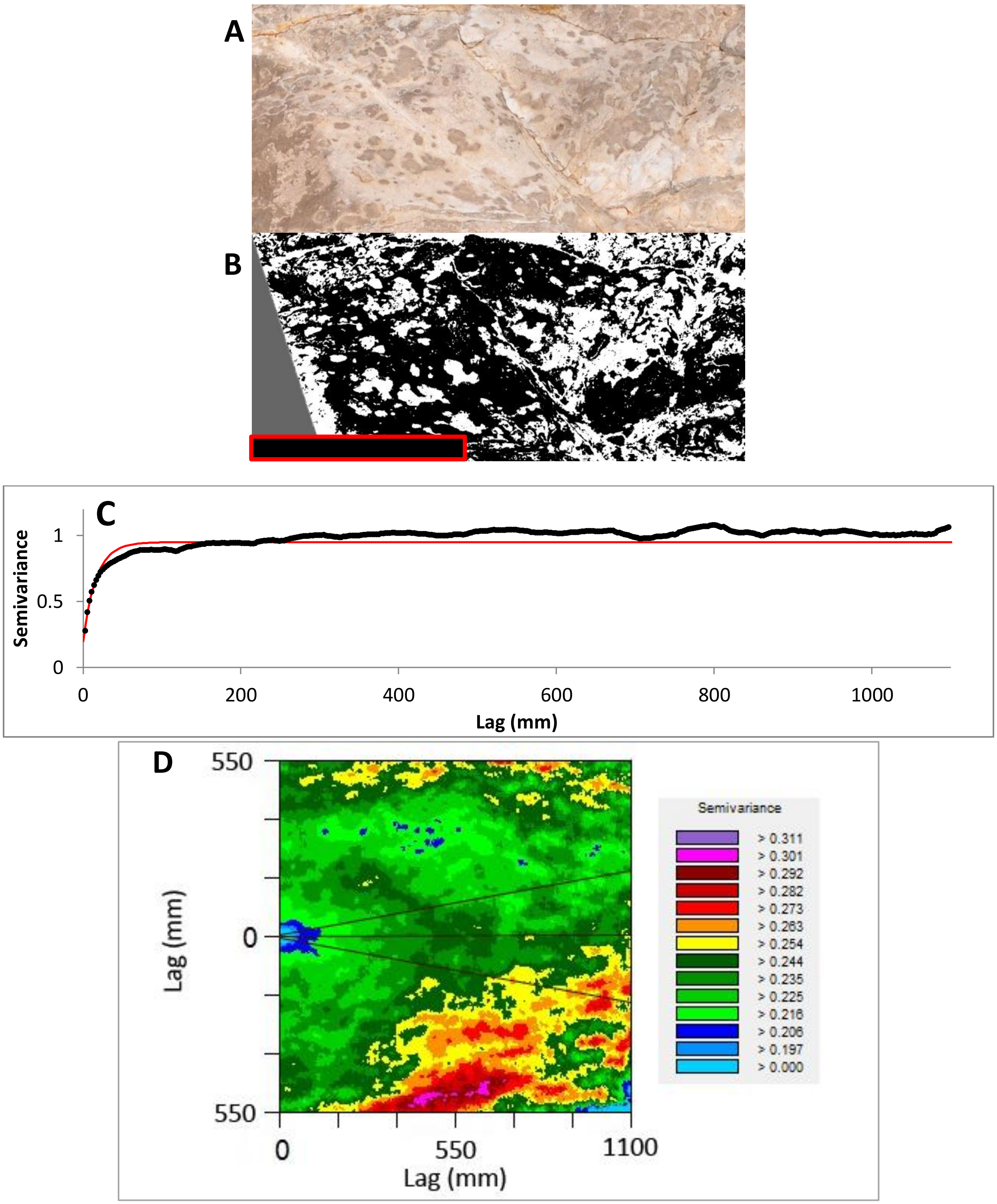

Figure 56. "Upstream" outcrop photomosaic and corresponding variogram in the Tansill Formation. (A) Color and (B) grayscale images of the outcrop where dolomite is black and limestone is white. See Figure 34 for of the upstream location relative to the midstream photomosaic. Scale bar is 50 cm. (C) Experimental semivariogram of lithology with exponential (red) model fit to the data. Correlation range is 50 mm. (D) Semivariance map showing the anisotropic semivariogram (horizontal line) as reasonably representative of variance in all subhorizontal directions.

San Andres Observations

Two outcrop photomosaics were analyzed for the San Andres Formation, herein called outcrop A and outcrop B, which are separated by about 30 meters. The outcrop A photomosaic (Figure 57A) is 5.75 m wide and 1.5 m tall and was sampled at a spacing of 2.5 cm. This yielded a grid of 12,882 data points, of which 6,866 were dolomite and 4,104 were limestone (63% dolomite). The experimental indicator semivariogram for dolomite (Figure 57C) exhibits 30% of its total semivariance at the modeled nugget. The correlation range is 25 cm. There are three hole-effects at lags of 330 cm, 410 cm, and 480 cm that yielded a wavelength of 70 cm and an amplitude equivalent to 6% of the total semivariance. The semivariance map (Figure 57D) shows that the anisotropic semivariogram is representative of all subhorizontal semivariograms. Total semivariance is the same along all angles and hole-effects are distributed similarly at all angles, especially beyond lags of 250 cm (distribution of red and green between lags of 250-500 cm is similar at all angles).

The outcrop B photomosaic (Figure 58A) is 10.3 m wide and 1.2 m and was sampled at a spacing of 2 cm. This yielded a grid of 29,580 data points, of which 21,977 were dolomite and 4,948 were limestone points (82% dolomite). The experimental indicator semivariogram for dolomite (Figure 58C) exhibits 30% of its total semivariance at the modeled nugget. The correlation range is 50 cm and there are four hole-effects with a modeled wavelength of 220 cm and an amplitude equivalent to 8% of the total semivariance. The semivariance map (Figure 58D) shows that the +10° transect has very high semivariance at its longest lag and the -10° transect has very low semivariance at its longest lag, which is inconsistent with the anisotropic semivariogram. This may be caused by the fact that the outcrop is much longer in the horizontal direction. Lower angle semivariograms (i.e., less than ±5°) are similar to the anisotropic semivariogram. The semivariance near the origin is elongate in the horizontal direction, indicating that the correlation range is longest in the horizontal direction. Overall, the anisotropic semivariogram is representative of very low angle subhorizontal transects (i.e., less than ±5°) ; in particular they all would exhibit small hole-effects (color mottling in the map).

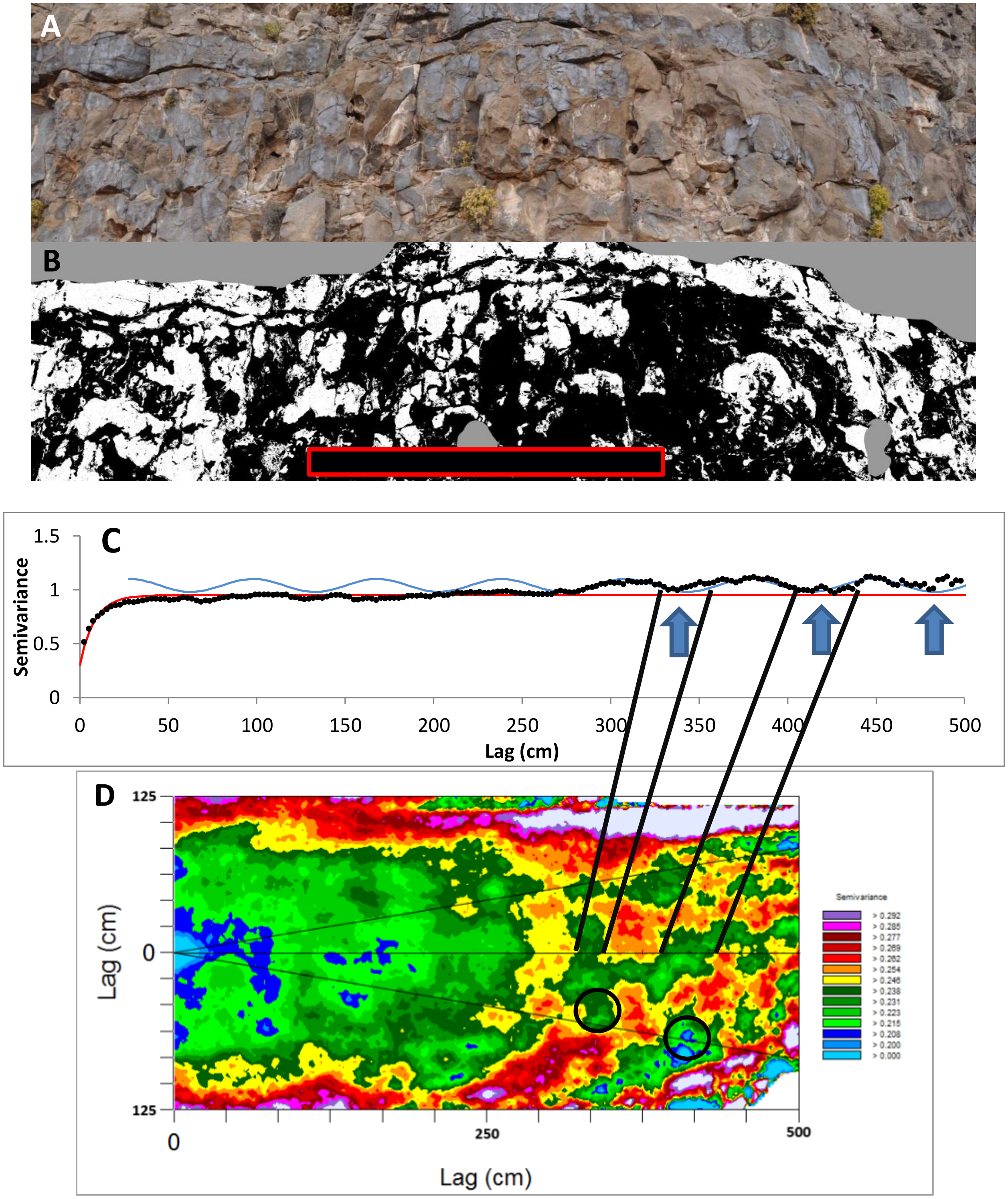

Figure 57. Outcrop "A" photomosaic and corresponding variogram, San Andres Formation. (A) Color and (B) grayscale images of the outcrop where dolomite is black and limestone is white. Scale bar is 2m. (C) Experimental semivariogram of lithology with exponential (red) and hole-effect (blue) models fit to the data. Correlation range is 25 cm and blue arrows mark hole-effects that have a modeled wavelength of 70 cm. (D) Semivariance map showing that the anisotropic semivariogram is representative of variance in all subhorizontal directions. Lines between (C) and (D) show how the anisotropic variogram matches the semivariance map. Hole-effects with similar wavelengths and amplitudes exist (e.g. black circles) in other directions.

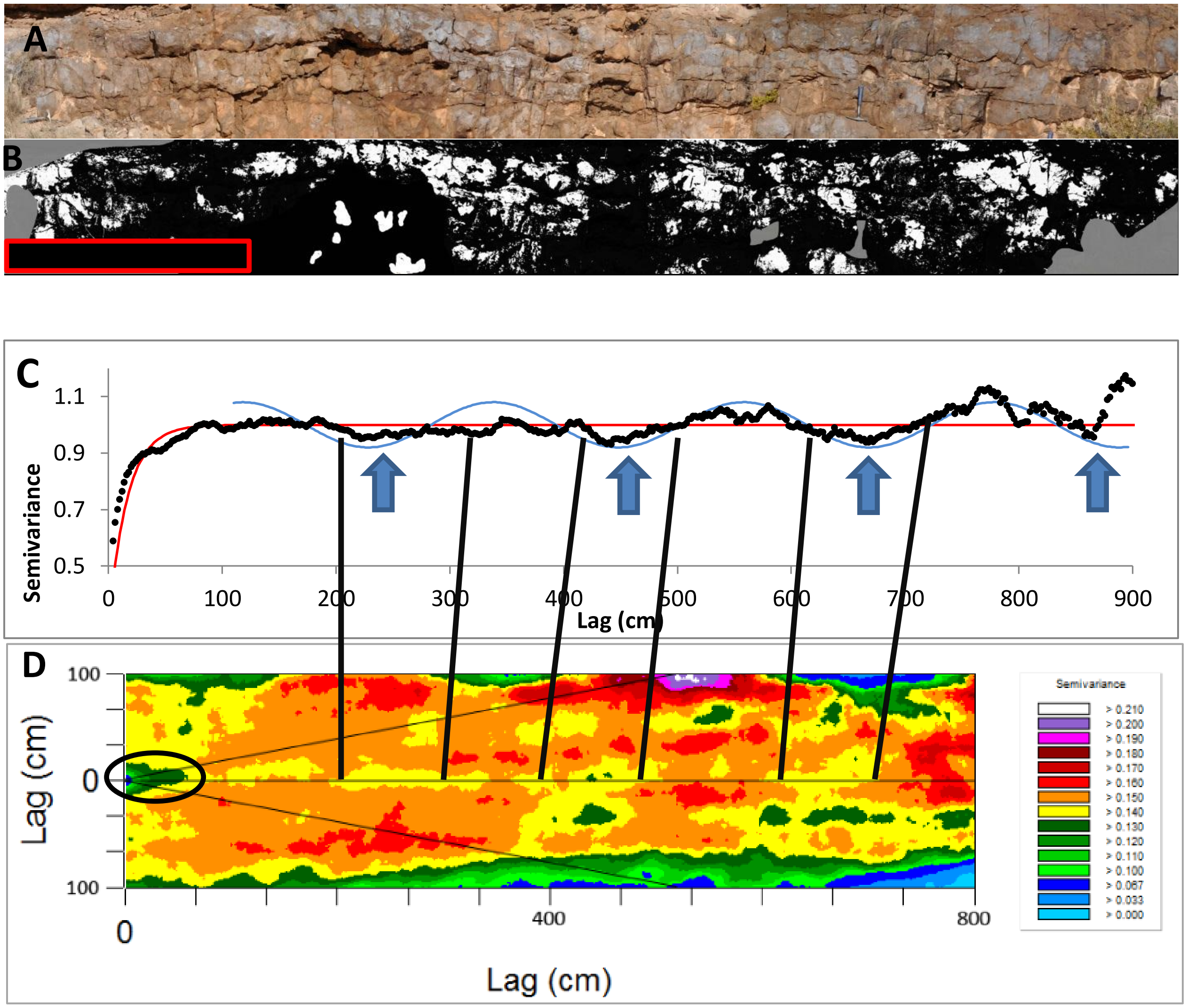

Figure 58. Outcrop "B" photomosaic and corresponding variogram, San Andres Formation. (A) Color and (B) grayscale images of the outcrop where dolomite is black and limestone is white. Scale bar is 2 m. (C) Experimental semivariogram of lithology with exponential (red) and hole-effect (blue) models fit to the data. Correlation range is 50 cm. and modeled hole-effect wavelength is 220 cm. (D) Semivariance map showing that the anisotropic semivariogram is representative variance in all low angle (<5°) directions. Correlation range is longest in the horizontal direction as shown by the elongate green patch at the origin (circled in black). Hole-effects are present (color mottling) across the entire map.

CHAPTER 5: DISCUSSION

This thesis has shown that permeability and porosity data collected at the slab scale (1-2 cm spacing) has correlation ranges of 4-20 cm and hole effects with wavelengths between 20-30 cm. Thin-section porosity variograms exhibited correlation ranges of 0.2-0.5 cm and hole effects with wavelengths of 2.8-4.6 cm. Several thin sections showed single hole effects with apparently long wavelengths, but these did not exhibit a second hole and so they are not reported here. It is possible that these longer wavelengths are associated with holes seen at the slab scale. The outcrop photomosaics exhibited correlation ranges of 5-230 cm and hole effects with wavelengths of 70-560 cm. The wide range in both correlation ranges and hole effect wavelengths for the outcrop photomosaics may arise from the wide range in sampling scale.

The data presented herein were collected at a variety of small scales in order to address the question of whether a power-law relationship exists between sample spacing and the correlation range and hole-effect wavelength interpreted on variograms of dolomite attributes. The data collected herein (Table 2) and by prior workers (Table 1) are consistent with a power-law relationship (Figure 59) between sample spacing, correlation range, and hole-effect wavelength.

The presence of both short-range correlation structures and longer ranging hole effects in the spatial patterns of dolomite attributes (Tables 1 and 2), and particularly porosity, means that dolomite attributes form nested structures. That is, the overall structure contains other structures as members. In addition to nesting, the relationship between sample spacing and variogram attributes shown in Figure 59 suggests that the spatial characteristics of petrophysical properties in dolomites also correlate across multiple spatial scales. The data suggest that dolostone properties exhibit a scale invariant nesting of spatial patterns.

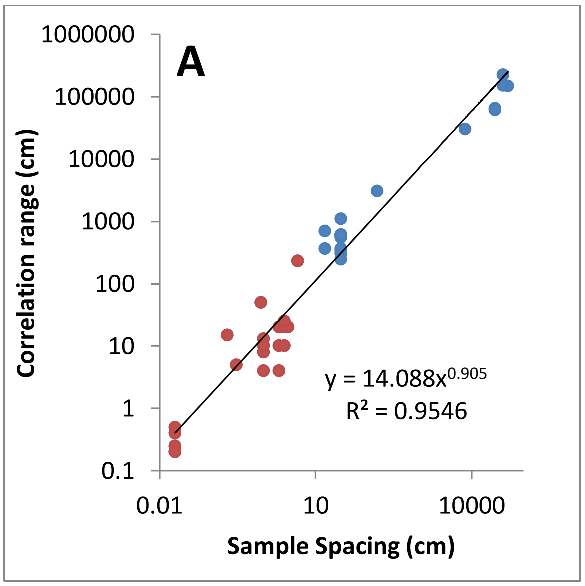

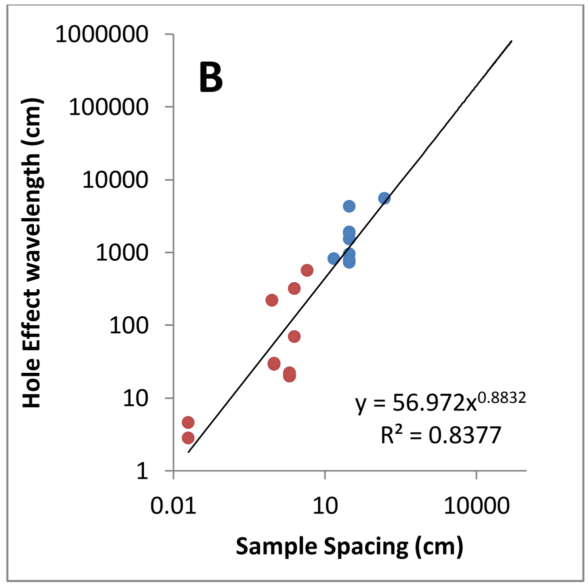

Figure 59. Relationship between sample spacing and (A) correlation range and (B) hole effect wavelength. Red points are data collected herein (Table 2) and blue points are published data (Table 1). Both plots show a strong power-law regression, thus supporting the hypothesis that sample spacing is correlated to range and hole effect wavelength.

Three hypotheses could explain why nested patterns apparently follow a power law: (1) variogram attributes are related to the spacing between samples, (2) variogram attributes are related to the volume of investigation of each sample, or (3) variograms generated with short sample spacings cover transect lengths that are too short and thus violate the assumption of stationarity (mean and variance do not vary significantly in space), which is required for variography, thus the power-law relationship in Figure 59 is illusory. These hypotheses are systematically evaluated and compared to the observations documented herein to determine the most plausible explanation for the power-law relationship seen in Figure 59.

Hypothesis 1: Variogram attributes are related to sample spacing

The hypothesis that correlation range and hole-effect wavelength are strictly related to sample spacing can be easily tested with a sufficiently long data transect. For example, the BCDE thin-section transect can be used to create a continuous lateral dataset that is 18,000 data points long (200 mm), where each point is the average of all pixels in that column. That is, the value of point 1 is the percentage of points in column 1 that are inside a pore. Using a constant volume of investigation (i.e., constant number of pixels analyzed in each sample) and transect length, three experimental semivariograms were created with 1-pixel, 10-pixel, and 100-pixel spacings (Figure 60). All three experimental semivariograms exhibit the same general shape with very similar correlation ranges and hole effects. This same test was conducted using outcrop minipermeability data from the 314 m long San Andres Formation transect reported by Jennings et al. (2000). Two experimental semivariograms were created with 30 cm and 300 cm spacings (Figure 61). Again, the correlation range and hole-effect wavelength are consistent between the two different sample spacings. These two tests indicate that the power-law seen in Figure 59 is not simply a relationship between sample spacing and variogram attributes. That is, sample spacing itself is not the dependent variable. Instead, sample spacing must be acting as a proxy for the actual dependent variable. Hypotheses 2 and 3 explore possibilities of what sample spacing may represent.

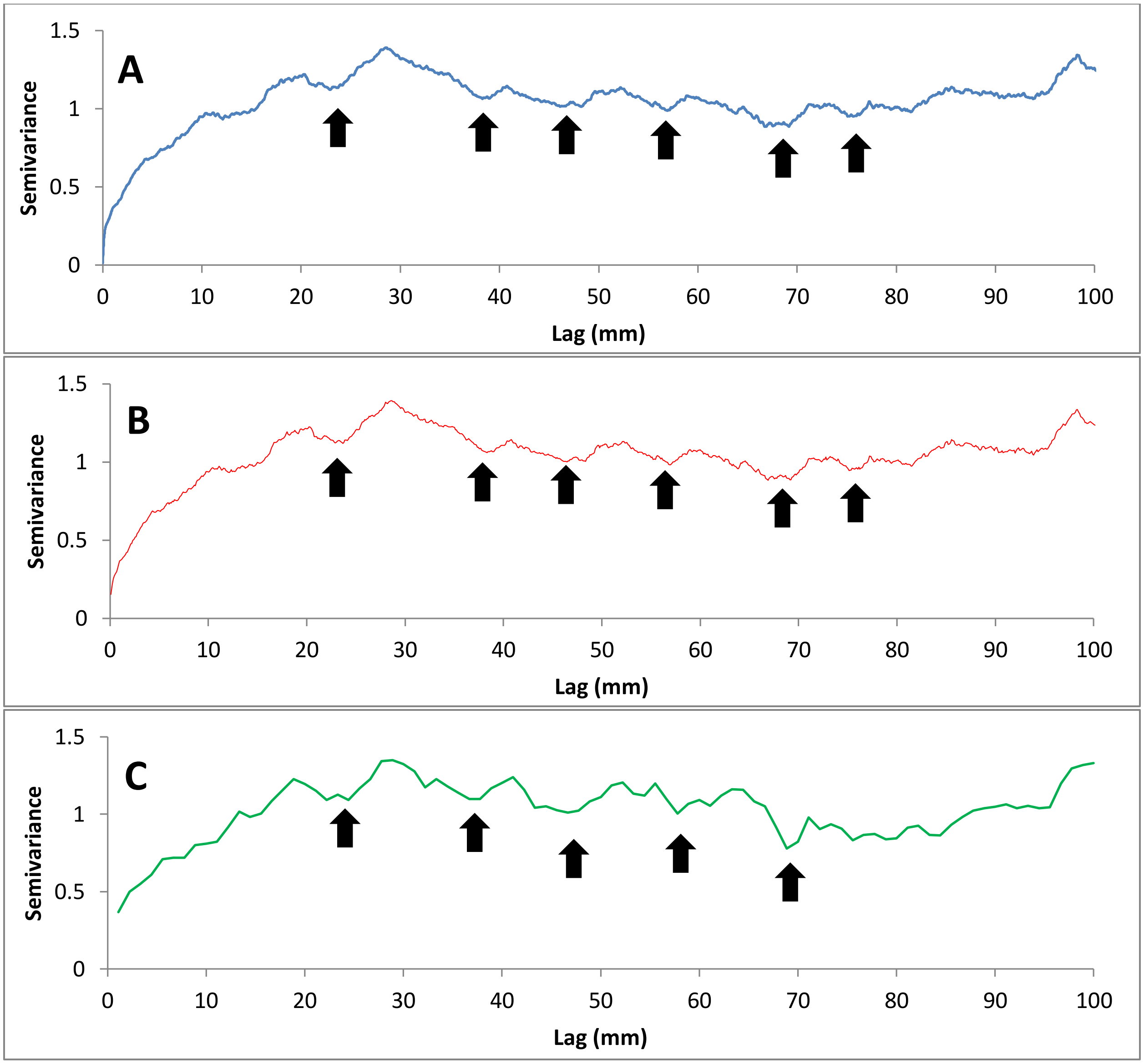

Figure 60. Experimental semivariograms of thin-section porosity based on a 18,000 pixel long (200 mm) transect across the thin sections from sample BCDE. (A) 1-pixel spacing, (B) 10-pixel spacing and (C) 100-pixel spacing variograms all exhibit nearly identical variogram attributes, including the same correlation range (~20 mm) and low amplitude hole-effects (arrows) across two orders of magnitude variation in sample spacing.

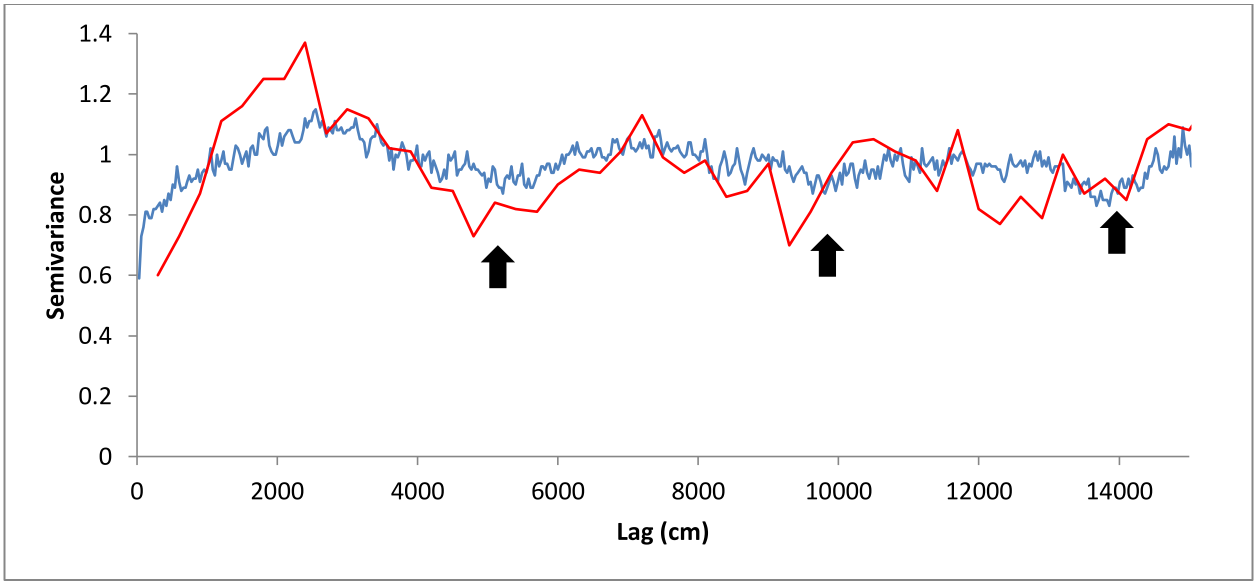

Figure 61. Experimental semivariograms of ln(k) from a 314 m long San Andres Formation outcrop transect (data from Jennings et al., 2000). The blue line represents sampling at 30 cm and the red line represents sampling at 300 cm. Correlation range and hole effects (arrows) are essentially the same despite varying the sample spacing by an order of magnitude.

Hypothesis 2: Variogram attributes are related to the support volume at each sampling scale

Some rock properties are known to follow a power-law relationship dependent on the volume of rock investigated (i.e., the support volume). For example, Whitaker and Smart (2000) showed that the apparent hydraulic conductivity of carbonate aquifers increases exponentially as progressively larger and larger volumes of rock are analyzed. This is because small scales of investigation (e.g., core plugs) only sample connected matrix pores, but progressively larger scales of investigation (e.g., well tests, field tests) include fractures and ultimately karst systems (Whitaker and Smart, 2000). The larger support volumes for the large scale tests allowed for the larger geologic features to be defined. Neuman (1990) and Gelhar (1992) described a similar power law relationship between the support volume and lateral dispersivity within a variety of aquifer types. While these studies provide examples of rock properties that follow a power law as a function of the support volume, they do not suggest that variogram properties would follow a similar power law. Nonetheless, a second hypothesis to explain the trends in Figure 59 is that sample spacing is a proxy for the amount of rock investigated, with the amount of rock investigated at each point along a transect (i.e., scale of investigation) affecting correlation range and wavelength of the hole effect.

Indeed, smaller sample spacings in the database (Tables 1, 2) generally are associated with smaller support volumes (or areas). At the thin-section scale, areas of ~10^{-6} cm^2 were measured at spacings of 10^{-2} cm. The outcrop photomosaics analyzed areas of $10^{-1.7}$ to $10^{1.3}$ cm^2 and sampled at $10^{-0.7}$ to $10^{0.7}$ cm scales, respectively. At the slab (10^0 cm) and outcrop ($10^{1.5}$ cm) sampling scales, porosity measurements were made on ~10 cm^3 of rock and permeabilities were measured on 10s of mm^3 of rock. Lastly, the subsurface data analyzed many meters of borehole data (≥10^3 cm^3 of rock) at spacings of 10^4 to $10^{4.5}$ cm.

One very simple test for the support volume hypothesis uses the same 18,000 data points used for hypothesis 1. In this test, the transect length remained the same at 200 mm (18,000 pixels). Support volume, in this case the area of the thin-section investigated at each point on the transect, was set at 1 pixel, 5 pixels, and 20 pixels for the three respective semivariograms (Figure 62). The sampling points were offset so that no points were shared between the 1 and 5 pixel datasets. That is, the first semivariogram (1 pixel area) analyzed points 10, 20, 30, 40…etc. and the second semivariogram (5 pixel area) analyzed the averages of points 13-17, 23-27, 33-37, 43-47…etc. The 20 pixel semivariogram analyzed the averages of points 1-20, 21-40,…etc. The resultant semivariograms are identical (Figure 62) and suggest that the power law relationship is not simply a function of the support volume (or area) if the different scales of investigated rock contain nothing different.

By analogy to the work of Whitaker and Smart (2000), the increased volume of rock must also contain something that the smaller volume did not. For example, the larger volume captures a fracture network that the smaller volume did not define. In order to test this, a second test was performed that used the same 18,000 point data set from hypothesis 1, but simulated a vug network with a 100 pixel spacing. The presence of a “vug” was achieved by randomly increasing the original value by two orders of magnitude every 90-110 pixels (thus an average “vug” spacing of 100 pixels). Semivariograms were then run using a large area of investigation (20 pixels) that would presumably capture this simulated vug network within the matrix pore system and a small area of investigation (1 pixel) that would not capture the vugs as effectively (i.e., the small area of investigation used the original values). Semivariograms for this test (Figure 63) differ. At the small area of investigation, there is a short correlation range of ~20 mm and possibly some low amplitude hole-effects. In contrast, the semivariogram done with a large area of investigation shows no short range correlation; semivariance is essentially at the sill for all lags thus meaning a random distribution of the property. This example demonstrates that differing scales of investigation can effect variogram properties when the different scales capture different scales of heterogeneity. This is true despite sample spacing and transect length being the same for the two different scales.

Obtaining different correlation ranges and wavelengths of hole effects due to the volume of material investigated for any one data point might be the cause for the subsurface data to exhibit variogram attributes so much greater than all other data sets in Tables 1 and 2.

Thin-sections were sampled in such a way that the semivariogram captured the spatial relationship between individual pores. The volume of rock investigated for the outcrop samples captures matrix networks of porosity and permeability and the semivariogram reflects the spatial variability in those networks. The volume of investigation for subsurface data captures enough rock that matrix porosity and permeability networks are no longer the primary source of heterogeneity. Instead, subsurface variograms likely reflect spatial heterogeneity and patterning contributed by varied facies types, facies attributes, or fractures. Since the amount of rock sample at each point defines progressively larger types of heterogeneity at larger scales, it is reasonable to assume that the support volume is a significant cause for the power-law relationship in Figure 59, particularly from outcrop to subsurface scale.

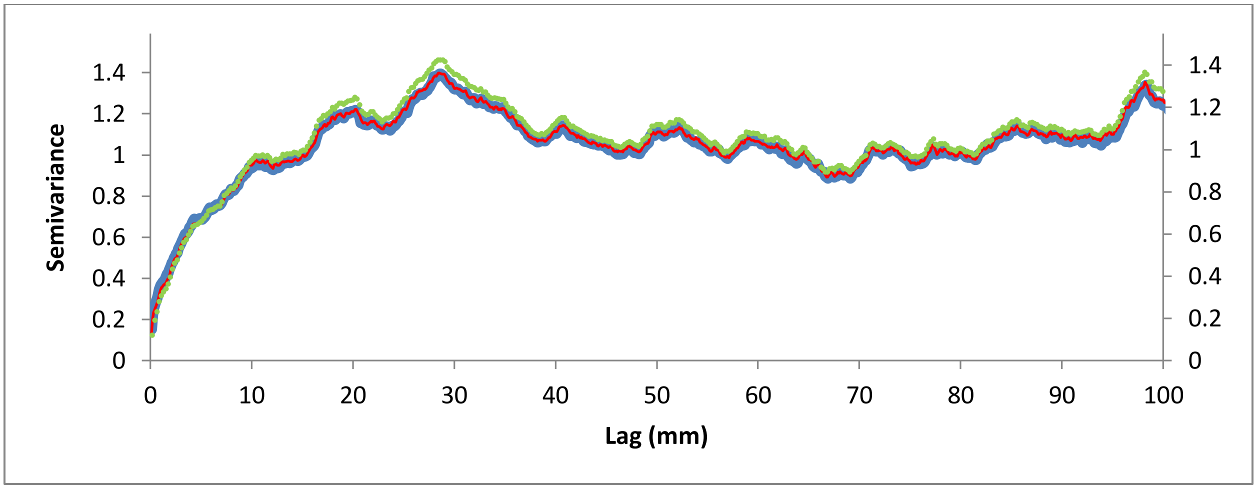

Figure 62. Experimental semivariograms of thin-section porosity using different areas of investigation. The blue line represents semivariance with a 1 pixel area of investigation. The red line represents semivariance with a 5 pixel area of investigation. The green line represents semivariance with a 20 pixel area of investigation. All semivariograms have been normalized to a sill of 1. The semivariograms are identical despite the difference in area of investigation (i.e., support volume).

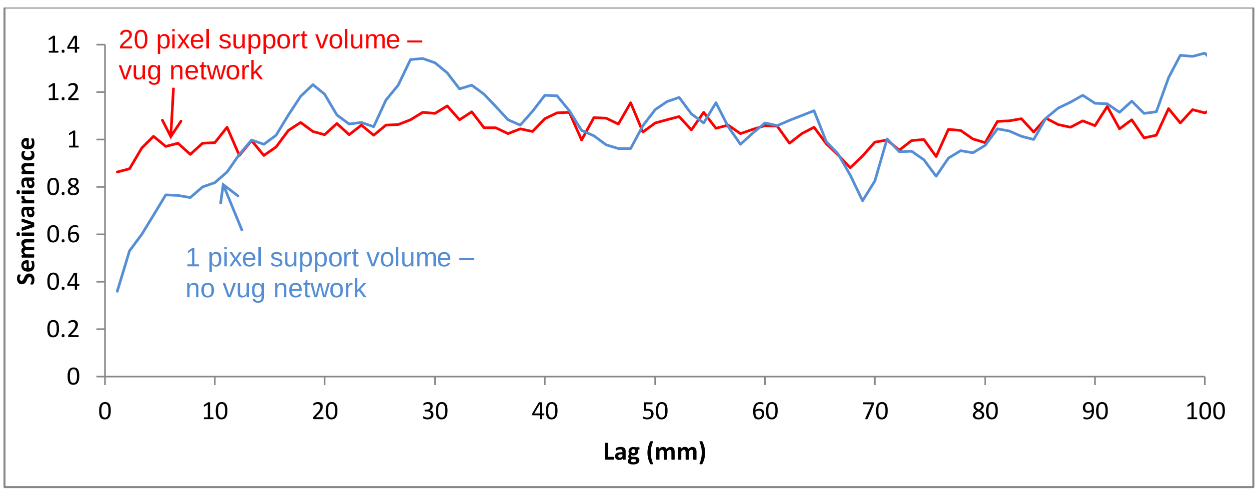

Figure 63. Experimental semivariograms of thin-section porosity with an artificial vug network inserted at a 100 pixel spacing. The blue line represents semivariance with a 1 pixel area of investigation. The red line represents semivariance with a 20 pixel area of investigation, which captures the hypothetical vug network.

Hypothesis 3: Short transects are not stationary (a requirement for variography), thus the power-law is illusory

To this point, it has been assumed that all the data sets contributing to Figure 59 exhibited stationarity, meaning variance did not vary significantly in space. Thus, it was also assumed that correlation ranges and hole effects for short transects (i.e., slabs and thin-sections) were real. In reality, this is not true because all of the slabs collected are too short to exhibit statistical stationarity. For example, the variance and mean log permeability of the Lysite slabs collected herein and Lysite outcrop data (Figure 5C,5D) are shown in Table 3. None of the slabs exhibit means or variances that are remotely similar to the outcrop. In analyzing the outcrop data, transects need to be ~90 meters long in order to exhibit stationarity (i.e., any 90 m transect exhibits the same mean and variance as the entire 150 m transect). Thus, the outcrop slabs analyzed herein were far too short to provide any useful results. While the majority of the slabs produced variograms that were interpreted as having sills, these variograms are just the result of random chance due to undersampling with insufficiently long transect lengths. This can be shown graphically by considering semivariograms of all Lysite slab and outcrop permeability data (Figure 64). When the slabs are considered individually (Figure 64A), some of their semivariograms may be interpreted as reaching a correlation range. However, when the slab data are combined into a single semivariogram and their semivariance is normalized to outcrop data (Figure 64B), it is apparent that the short slab transects are just part of the increasing semivariance before the range is reached. Figure 64B also exhibits the outcrop semivariance at a lag of 2.5 cm, which was calculated using the two ends of each core plug. This value matches the normalized slab permeability semivariance. Likewise, three scales of Lysite porosity data (thin-section, slab, and outcrop) are combined in Figure 64C. When all of the thin-sections are combined and all of the slab porosities are combined, apparent correlation ranges at microscales (as presented in the results section) are no longer present. In this case, the combined slab porosity data had a similar variance to the outcrop data and therefore it did not require correction, but the thin-section porosity semivariance values had to be corrected upward (Figure 64C). In both the permeability (Figure 64B) and porosity (Figure 64C) examples, variability is present at all scales, thus demonstrating that the slab data do not exhibit statistical stationarity.

Sample	Mean ln(k)	Population Variance - ln(k)	Mean Porosity	Population Variance - porosity
Lysite Outcrop	3.9	0.8	16.0	15.6
BCDE	2.3	0.2	12.8	7.5
KL	3.6	1.1	18.9	6.6
WXYZ	3.1	2.5	18.1	11.6
Combined slabs	3.2	1.6	17.6	13.4

Table 3. Average log permeability and population variance of Lysite outcrop data, three separate Lysite slabs, and the combined slabs. Since the slab means and variances are not consistent with the outcrop data, the data are not stationary at the slab scale.

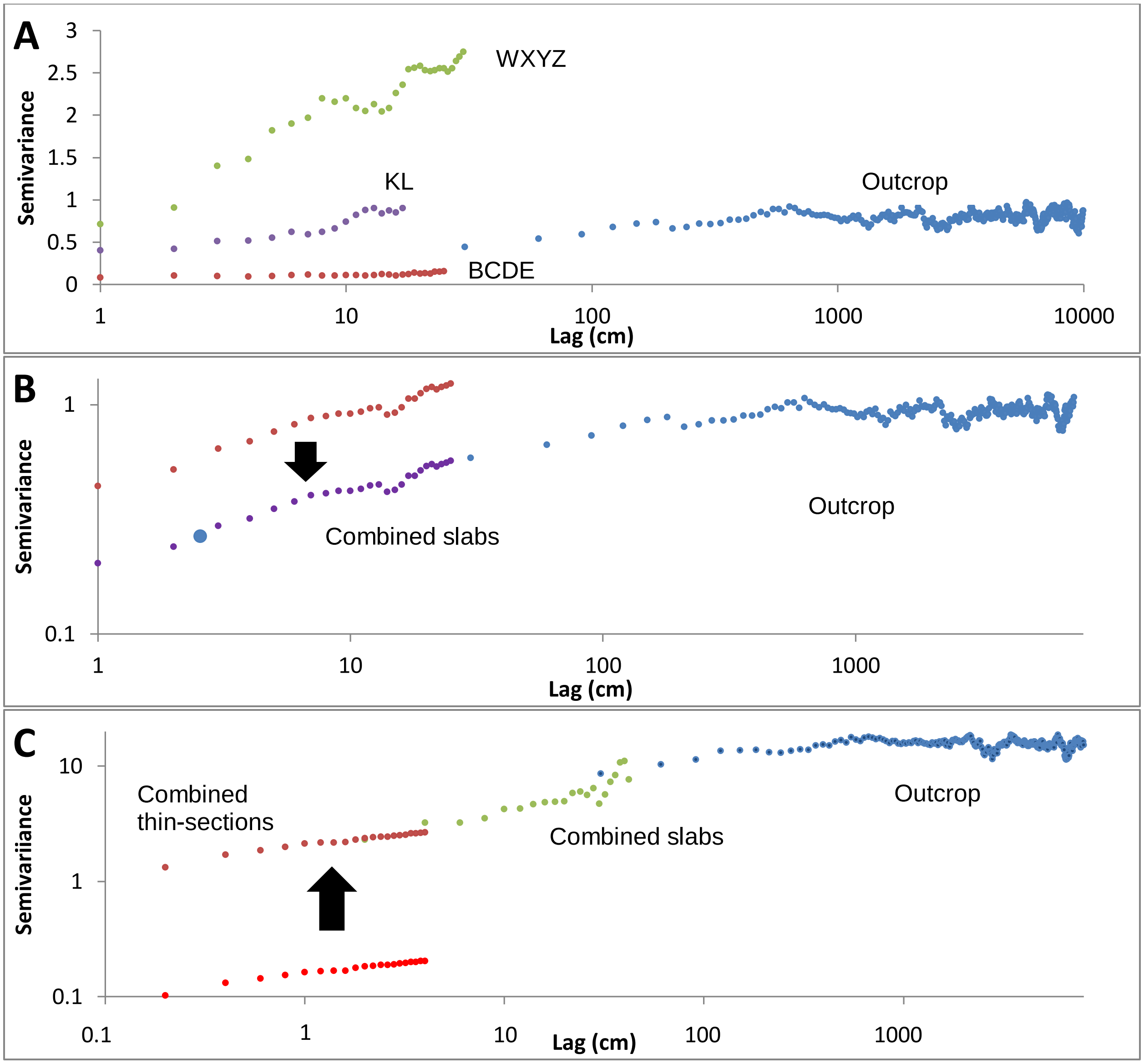

Figure 64. Experimental semivariograms showing data collected at multiple scales for the (A) Lysite outcrop permeability across individual slabs, (B) Lysite outcrop permeability from all combined slabs, and (C) Lysite outcrop, combined slabs, and combined thin-section porosity. When the slab and thin-section semivariance are combined and normalized to outcrop variance (black arrows), it is apparent that data collected at fine scales exhibit smoothly increasing semivariance below the sill. Normalization was done by dividing the semivariance at fine scales by the difference in population variance (Table 3) between fine and outcrop scale. Since none of the combined data at small scales have reached a sill, all interpreted correlation ranges and hole effects in the results (Table 2) are not valid.

As an analogy, the 18,000 pixel dataset used for hypotheses 1 and 2 can be analyzed at different transect lengths and different sample spacings in much the same way as the Lysite slab and outcrop transects. The entire 18,000 pixel transect was analyzed with a 30 pixel sample spacing and is compared to three randomly selected 1,800 pixel long transects with 1 pixel sample spacings (Figure 65A). Much like Figure 64A, each of the three short transects may be interpreted as having short correlation ranges around a lag of 0.3 mm. However, when all 1,800 pixel transects are combined, they exhibit no such correlation range (Figure 65B). This is exactly analogous to the way in which slabs were analyzed for this thesis and then compared to outcrop variograms, albeit without the luxury of being able to fill in all the areas where data were missing (i.e., going from Figure 65A to 65B).

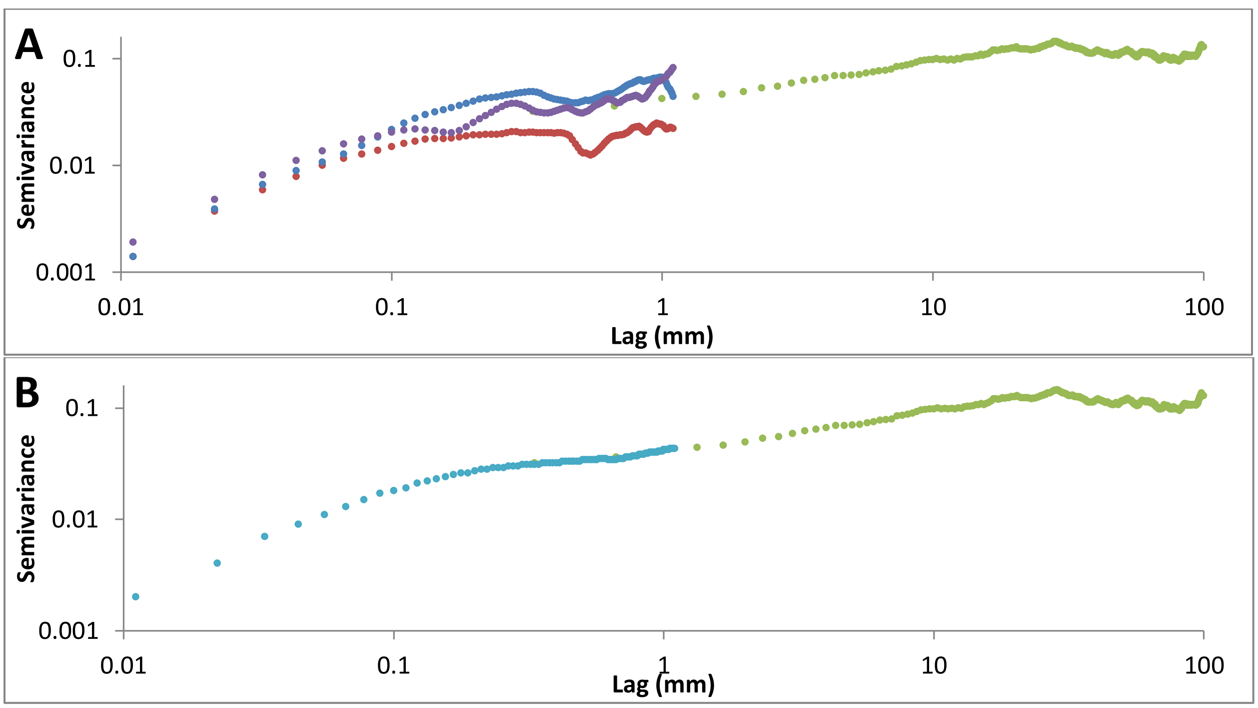

Figure 65. Experimental semivariograms for the BCDE thin section porosity transect. Green line is the result when the entire 18,000 pixel transect is analyzed with a 30 pixel spacing. (A) Three randomly selected 180 pixel transects with 1 pixel spacing and (B) all possible 180 pixel transects with 1 pixel spacing combined into a composite semivariogram (blue). The semivariograms for individual short transects (A) are not the same, thus the short transects do not exhibit stationarity. The semivariogram for all possible combined short transects (B) does not reach a correlation range and exhibits variability at all scales (thus it is not stationary).

Having shown that correlation ranges and hole-effects interpreted on the slab and thin-section data collected herein are not real, this calls into question the integrity of other data that were collected for this thesis. In particular, the short outcrop photomosaic transects (i.e., Cairn D, Cairn H, Tansill midstream, Tansill upstream, and San Andres A) are also likely too short to exhibit stationarity. The three longest outcrop photomosaics (i.e., Cairn E, Tansill downstream, and San Andres B) are all over 10 meters long and covered the entirety of their respective outcrop faces. The Cairn E outcrop variogram (Figure 52C) exhibits a long-range trend of increasing variance, which indicates non-stationarity for that outcrop. The Tansill downstream and San Andres B are more likely reliable data because they encompass the entire dolomite reaction front, whereas the shorter transects only cover only a small part of the reaction front (e.g., between two fractures as in Figure 34). In addition, the short transects were chosen specifically because they showed interesting spatial patterns between dolomite and limestone (e.g., Figures 55A and 56A), which was likely not representative of the reaction front as a whole. Thus, short outcrop photomosaics do not yield statistical stationarity and the data derived from them are not suitable for geostatistical analysis.

While the long outcrop photomosaics provide variogram data that reliably capture the spatial heterogeneity of the outcrops, these data probably cannot be used to help define the power-law (Figure 59) because they are based on different areas of investigation at each sampling point, different variables (lithology versus petrophysical properties), and are different types of variograms (indicator versus continuous). As such, any comparison of the outcrop photomosaics to outcrop and subsurface petrophysical data for the sake of defining a power law relationship across multiple scales is likely meaningless.

Summary

The analysis of the three hypotheses suggests that the power-law relationship seen in Figures 8 and 59 is not a real phenomenon due to multiple factors. First, the data sets collected from the slabs and thin-sections do not fit the requirement of stationarity. Those data sets sampled too short a length, and the ranges and hole-effects derived from their analysis are not real because the data sets are too small to capture the true variance present in the respective attributes. Second, analyzing different dolomite attributes at different volumes of investigation is the likely explanation for the very long correlation ranges of the data collected using wellbore tools. Subsurface data are generally derived from cubic meters worth of rock, which captures a much larger scale of heterogeneity than outcrop studies. Therefore, the power law defined in Figures 8 and 59 is just an artifact of misinterpretation of small-scale variograms and overinterpretation of the relationship between variograms derived for vastly different volumes of investigation. What this basically demonstrates is that there is variability at all scales and each scale has its own volume of support. Thus, a correlation range derived from outcrop measurements taken with a hand-held tool would be true for data at that scale, but would not be the correct value to use when modeling fluid flow in a large reservoir. That is because reservoir data are generally collected by methods with large support volumes (e.g., wellbore tools and seismic). Therefore, when a model is created based on those data, a correlation range that is consistent with those data is necessary. Thus, while the slab data collected herein did not exhibit actual variogram attributes (i.e., correlation range and hole effects), both the outcrop data and subsurface data exhibit variogram attributes that are true at their respective sampling scale.

In theory, a power law relationship across many scales could exist because there are many scales of heterogeneity that could potentially be captured by a variogram. As an alternative to the arguments above, a hypothetical argument could be made that the power law relationship is real and it is representative of different scales of heterogeneity. Geological heterogeneity exists at four general scales: microscale, mesoscale, macroscale, and megascale (Weber, 1986; Krause et al., 1987; Slatt, 2006). Analysis of the microscale might produce a variogram that defines the spatial distribution of pores where the correlation range (~10^{-1} cm) would be associated with the size of an average pore and hole effects would be associated with pore spacing. Analysis of mesoscale data (i.e., core, slab) data might produce a variogram that defines the spatial distribution of pore networks where the correlation range (~10^{1} cm) might be associated with overdolomitized and underdolomitized areas. It is even likely that the diagenetic processes that control the distribution of matrix pores in dolomite would also play an important role in the distribution of pore networks at an even larger scale. For example, Figure 65B exhibits two power-laws, one from lags of 0.01-0.1 mm and the other from lags of 0.1-10 mm. These power laws are defined by straight lines in the semivariance values. The smaller scale power-law (0.01-0.1 mm) likely corresponds with variability in pore size and the larger scale power-law (0.1-10 mm) likely corresponds with variability in pore density (i.e., porous and tight areas). Thus, a hypothetical power-law relationship that correlated pore distribution with the distribution of pore networks would be meaningful. Analysis of macroscale and megascale data would produce variograms that reflect the distribution of much larger scales of heterogeneity such as facies and entire flow units and would have correspondingly long correlation ranges because the scale of these types of heterogeneity are so much larger (i.e., tens to thousands of meters). A power-law relationship between mesoscale and macroscale would be less meaningful because the processes that control these features are not strongly related.

CHAPTER 6: CONCLUSION

The research question posed in this thesis was, does a power law relationship exist between correlation range and hole-effect wavelength across many magnitudes of sampling scale. This question was addressed by analyzing the spatial variability of various properties of dolomites at sub-meter sampling scales. Porosity and permeability were analyzed on five outcrop slabs from the Madison Formation and Cairn Formation. The slabs produced variograms that either exhibited long-range trends or apparent correlation ranges of 4-20 cm and hole effects with wavelengths of 20-30 cm. Thin-sections were collected from each of these slabs and analyzed for porosity, which was shown to exhibit either long-range trends or apparent correlation ranges of 0.2-0.5 cm and hole effect wavelengths of 2.8-4.6 cm. Outcrop photomosaics of macroscale vugs and dolomite-limestone reaction fronts were created at the Cairn Formation, Tansill Formation, and San Andres Formation. These attributes were shown to have apparent correlation ranges of 5-230 cm and hole effects with wavelengths of 70-560 cm.

When the data collected herein was considered in conjunction with previously collected literature data, a power-law relationship did appear to exist for both correlation range and hole effect wavelength over several magnitudes of sampling scale. Three possible hypotheses were considered to explain this apparent trend: (1) variogram attributes are related to the sample spacing, (2) variogram attributes are related to the support volume at each sampling scale, and (3) variograms generated over short sample spacing covered transect lengths that are too short to exhibit statistical stationarity and therefore the power-law relationship is illusory. When testing hypothesis 1, it was shown that varying sample spacing did not have any effect on variogram attributes, even over several orders of magnitude. Hypothesis 2 was argued to be a possible explanation, in particular when considering the subsurface datasets where a single data point reflects the averaging of properites over many meters of stratigraphic section. Hypothesis 3 was shown to be valid because short transects did not exhibit stationarity relative to longer transects of the same attributes in the same rocks. Therefore, it is concluded that the power-law relationship presented herein is not real. At small sample spacings, it is defined by data sets that lack stationarity; at large sample spacings, it is defined by dramatically different volumes of rock being investigated in an analysis. While a power-law relationship may exist for spatial patterning across many scales of dolomite heterogeneity, the power-law presented in this thesis is falsified.

REFERENCES

Amthor, J.E., E.W. Mountjoy, and H.G. Machel, 1994, Regional-scale porosity and permeability variations in Upper Devonian Leduc Buildups: implications for reservoir development and prediction in carbonates: AAPG Bulletin, v. 78, p. 1541-1559

Atchley, S.C, L.W. West, and J.R. Slugget, 2006, Reserves growth in a mature oil field: The Devonian Leduc Formation at Innisfail field, south-central Alberta, Canada: AAPG Bulletin, v. 90, p. 1153-1169

Bribiesca, E.A., 2010, Lateral variations in petrophysical, geochemical and petrographic properties of an Avon Park (middle Eocene) dolograinstone, Gulf Hammock Quarry, Florida: Masters Thesis, University of Colorado at Boulder

Budai, J.M., K.C. Lohmann, and J.L. Wilson, 1987, Dolomitization of the Madison Group, Wyoming and Utah Overthrust Belt: AAPG Bulletin, v. 71, p. 909-924

Budd, D.A., 2001, Permeability loss with depth in the Cenozoic carbonate platform of west-central Florida: AAPG Bulletin, v. 85, p. 1253-1272

Budd, D.A., M.J. Pranter, and Z.A. Reza, 2006, Lateral periodic variations in the petrophysical and geochemical propterties of dolomite: Geology , v. 34, p. 373-376

Buschkuehle, B.E. and H.G. Machel, 2002, Diagenesis and paleofluid flow in the Devonian Southesk-Cairn carbonate complex in Alberta, Canada: Marine and Petroleum Geology, v. 19, p. 219-227

Eisenberg, R.A., P.M. Harris, C.W. Grant, D.J. Goggin, and F.J. Conner, 1994, Modeling reservoir heterogeneity within outer ramp carbonate facies using an outcrop analog, San Andres Formation of the Permian Basin: AAPG Bulletin, v. 78, p. 1337-1359

Garcia-Fresca, B., 2009, Outcrop-constrained flow and transport models of reflux dolomitization: Masters Thesis, University of Texas at Austin

Garcia-Fresca, B., F.J. Lucia, J.M. Sharp, and C. Kerans, 2012, Outcrop-constrained hydrogeological simulations of brine reflux and early dolomitization of the Permian San Andres Formation: AAPG Bulletin, v. 96, p. 1757-1781

Gelhar, L.W., 1992, Critical review of data on field-scale dispersion in aquifers: Water Resources Research, v. 28, p. 1955-1974

Grant, C.W., D.J. Goggin, and P.M. Harris, 1994, Outcrop analog for cyclic-shelf reservoirs, San Andres Formation of Permian Basin: stratigraphic framework permeability distribution, geostatistics and fluid-flow modeling: AAPG Bulletin, v. 78, p.23-54

Gringarten, E. and C.V. Deutsch, 2001, Teacher's aide variogram interpretation and modeling: Mathematical Geology, v. 33, No. 4

Heylighen, F., 2008, Complexity and self-organization: Encyclopedia of Library and Information Sciences

Hurst, H. and D.J. Goggin, 1995, Probe permeametry: an overview and bibliography: AAPG Bulletin, v. 79, p. 463-473

Jennings, J.W., S.C. Ruppel, and W.B. Ward, 2000, Geostatistical analysis of permeability data and modeling of fluid-flow effects in carbonate outcrops: SPE Reservoir Evaluation & Engineering, v. 4

Katz, D.A., 2008, Early and late diagenetic processes of Mississippian carbonates, northern U.S. Rockies: Doctoral Dissertation, University of Miami

Kerans, C., and W.M. Fitchen, 1995, Sequence hierarchy and facies architecture of a carbonate ramp system; San Andres Formation of Algerita Escarpment and western Guadalupe Mountains, West Texas and New Mexico. University of Texas at Austin, Bureau of Economic Geology: Austin, TX. Report of Investigations 235, p. 86.

Kerans, C., F.J. Lucia, and R.K. Senger, 2001, Integrated characterization of carbonate ramp reservoirs using permian San Andres Formation outcrop analogs: AAPG Bulletin, v. 78, p.181-216

Kittridge, M.G, L.W. Lake, F.J. Lucia, and G.E. Fogg, 1990, Outcrop/subsurface comparisons of heterogeneity in the San Andres Formation: SPE Formation Evaluation, v. 5, No. 3

Krause, F.F., H.N. Collins, D.A. Nelson, S.D. Machemer, and P.R. French, 1987, Multiscale anatomy of a reservoir: geological characterization of Pembina-Cardium Pool, West-Central Alberta, Canada: AAPG Bulletin, v. 71, p. 1233-1260

Machel, H.G., and B.E. Buschkuehle, 2008, Diagensis of the Devonian Southesk Southesk-Cairn Carbonate Complex, Alberta, Canada: marine cementation, burial dolomitization, thermochemical sulfate reduction, anhydritization, and squeegee fluid flow: Journal of Sedimentary Research, v. 78, p.366-389

Mathias, W.D., 2011, Characteristics and origin of lateral cyclic patterns in petrophysical, Geochemical, and Petrographic Properties of Dolomite: Miocene Seroe Domi Formation, Bonaire, Netherland Antilles: Masters Thesis, University of Colorado at Boulder

Moore, C.H., 1989, Carbonate Diagenesis and Porosity: Developments in Sedimentology, v. 46

McNamara, L.B., N.C. Wardlaw, and M. McKellar, 1991, Assessment of porosity from outcrops of vuggy carbonate and application to cores: Bulletin of Canadian Petroleum Geology, v. 39, p.260-269

Neuman, S.P., 1994, Generalized scaling of permeabilities: validation and effect of support scale, Geophysical Research Letters, v.21, p.349-352

Neuman, S.P., 1990, Universal scaling of hydraulic conductivities and dispersivities in geologic media: Water Resources Research, v. 26, p. 1749-1758

Ortoleva, P.J., E. Merino, C. Moore, and J. Chadam, 1987a, Geochemical self-organization, I: reaction-transport feedbacks and modeling approach: American Journal of Science, v. 287, p. 979–1007

Pranter, M.J, C.B. Hirstius, and D.A. Budd, 2005, Scales of lateral petrophysical heterogeneity in dolomite lithofacies as determined from outcrop analogs: implications for 3-D reservoir modeling, AAPG Bulletin, v. 89, p. 645-662

Pranter, M.J., Z.A. Reza, and D.A. Budd, 2006, Reservoir-scale characterization and multiphase fluid-flow modelling of lateral petrophysical heterogeneity within dolomite facies of the Madison Formation, Sheep Canyon and Lysite Mountain, Wyoming, USA, Petroleum Geoscience, v. 12, p.29-40

Rossini, C., F. Brega, L. Piro, M. Rovellini, and G. Spolti, 1994, Combined geostatistical and dynamic simulations for developing a reservoir management strategy: a case history, SPE Journal of Petroleum Technology, v.46, p. 979-985

Senger, R.K., F.J. Lucia, C. Kerans, G.E. Fogg, and M.A. Ferris, 1993, Dominant control on reservoir-flow behavior in carbonate reservoirs as determined from outcrop studies, *in* W. Linville, ed., Reservoir characterization III: Proceedings, Third International Reservoir Characterization Technical Conference, Tulsa, OK, p. 107–150

Slatt, R.M., 2006, Stratigraphic reservoir characterization for petroleum geologists, geophysicists and engineers: Handbook of Petroleum Exploration and Production, v. 6, p. 19-23

Smith, L.B., G.P. Eberli, and M. Sonnenfeld, 2004, Sequence-stratigraphic and paleogeographic distribution of reservoir-quality dolomite, Madison Formation, Wyoming and Montana: AAPG Memoir 80, p. 67-92

Sonnenfeld, M.D., 1996, Sequence evolution and hierarchy within the Lower Mississippian Madison Limestone of Wyoming, in M. W. Longman and M. D. Sonnenfeld, eds., Paleozoic systems of the Rocky Mountain region: Rocky Mountain Section SEPM, p. 165–192.

Vandeginste, V., R. Swennen, S.A. Gleeson, R.M. Ellam, K. Osadetz, and F. Roure, 2009a, Thermochemical sulphate reduction in the Upper Devonian Cairn Formation of the Fairholme carbonate complex (South-West Alberta, Canadian Rockies): evidence from fluid inclusions and isotopic data: Sedimentology, v. 56, p. 439-460

Vandeginste, V., R. Swennen, M.H. Reed, R.M. Ellam, K. Osadetz, and F. Roure, 2009b, Host rock dolomitization and secondary porosity development in the Upper Devonian Cairn Formation of the Fairholme carbonate complex (South-west Alberta, Canadian Rockies): diagenesis and geochemical modeling: Sedimentology, v. 56, p. 2044-2060

Wang, F.P, J. Dai, and C. Kerans, 1998, Modeling dolomitized carbonate-ramp reservoirs: A case study of the Seminole San Andres unit – Part II, Seismic modeling, reservoir geostatistics and reservoir simulation: Geophysics, v. 63, p.1876-1884

Weber, K.J., 1986, How heterogeneity affects oil recovery, in, Lake, L.W. and Carrol, Reservoir Characterization, p. 487-545.

Whitaker F.F. and P.L. Smart, 2000, Characterizing scale-dependence of hydraulic conductivity in carbonates: evidence from the Bahamas: Journal of Geochemical Exploration v. 69-70, p. 133-137